OFFICE OF NAVAL RESEARCH

Insulator-Metal Transition and Inhomogeneous Metallic State in
Conducting Polymers

by

R.S. Kohlman and A.J. Epstein

Prepared for Publication in

Handbook of Conducting Polymers, Second Edition (Chapter 3)

The Ohio State University
Department of Physics
Columbus, OH

DTIC QUALITY INSPECTED 2

19971015 130   September 20, 1997

REPORT DOCUMENTATION PAGE

Form Approved OMB No. 0704-0188

1. AGENCY USE ONLY (Leave blank)	2. REPORT DATE 9/20/97	3. REPORT TYPE AND DATES COVERED Technical

4. TITLE AND SUBTITLE
Insulator-Metal Transition and Inhomogeneous Metallic State in Conducting Polymers

5. FUNDING NUMBERS
N00014-95-1-0302

6. AUTHOR(S) R.S. Kohlman and A.J. Epstein

7. PERFORMING ORGANIZATION NAMES AND ADDRESS(ES)
Department of Physics
The Ohio State University
174 West 18th Avenue
Columbus, OH 43210-1106

8. PERFORMING ORGANIZATION REPORT NUMBER
P308

9. SPONSORING/MONITORING AGENCY NAME(S) AND ADDRESS(ES)
Office of Naval Research
800 N. Quincy Street
Arlington, VA 22217

10. SPONSORING/MONITORING AGENCY REPORT NUMBER

11. SUPPLEMENTARY NOTES Prepared for publication in Handbook of Conducting Polymers, Second Edition

12a. DISTRIBUTION/AVAILABILITY STATEMENT
Reproduction in whole or in part is permitted for any purpose of the US Government.
This document has been approved for public relearse and sale; its distribution is unlimited.

12b. DISTRIBUTION CODE

13. ABSTRACT (Maximum 200 words)

This review article summarizes the insulator to metal transition that occurs in polyaniline, polypyrrole, and polyacetylene with increasing order. Based on dc and microwave frequency conductivity and optical studies, an inhomogeneous disorder induced insulator-metal transition is proposed to occur.

14. SUBJECT TERMS
Conductivity, optical response, dielectric constant, conducting polymers, insulator-metal transition

15. NUMBER OF PAGES
120

16. PRICE CODE

17. SECURITY CLASS. OF RPT	18. SECURITY CLASS OF THIS PG.	19. SECURITY CLASS OF ABSTRCT.	20. LIMITATION OF ABSTRACT
Unclassified			

Insulator-Metal Transition and Inhomogeneous Metallic State in Conducting Polymers

R. S. Kohlman[a] and A. J. Epstein[a,b]

[a] Department of Physics and [b] Department of Chemistry, The Ohio State University, Columbus, Ohio 43210-1106

Contents

I. INTRODUCTION

For the past fifty years, conventional insulating polymer systems have been increasingly used as substitutes for structural materials such as wood, ceramics, and metals because of their high strength, light weight, ease of chemical modification and customization, and processibility at low temperatures [1]. In 1977, the high electrical conductivity of an organic polymer, doped polyacetylene, was reported [2], spurring interest in "conducting polymers [2-6]." The frequency dependent electrical transport in doped polyacetylene was investigated intensively to understand the transport mechanisms [6,7]. The common electronic feature of pristine (undoped) conducting polymers is the $\pi-$conjugated system which is formed by the overlap of carbon p_z orbitals and alternating carbon-carbon bond lengths [4,7-9]. (In some systems, notably polyaniline, nitrogen p_z orbitals and C_6 rings are also part of the conjugation path.) Figure 1 shows the chemical repeat units of pristine forms of several families of conducting polymers, i.e., trans- and cis-polyacetylene [(CH)$_x$], the leucoemeraldine base (LEB), emeraldine base (EB), and pernigraniline base (PNB) forms of polyaniline (PAN), and polypyrrole (PPy).

Due to the susceptibility of one-dimensional chains to Peierls distortions [10], charge doped into the polymer is stored in novel states such as solitons, polarons, and bipolarons, which include a charge and a lattice distortion which surrounds it [7]. Despite the strong electron-phonon coupling in conducting polymers, the conductivities of the pristine polymers can be transformed from insulating to metallic through the process of doping, with the conductivity increasing as the doping level increases. Both n-type (electron donating) and p-type (electron accepting) dopants have been utilized to induce an insulator-metal transition in electronic polymers [2-5,7-9].

An extraordinary large range of conductivity is obtained upon doping [11-28]. Figure 2 shows that the conductivity of each undoped polymer can be increased by 10 orders or more. For instance, the conductivity of polyacetylene processed by various routes [11-13,25,26,29-32] when doped with iodine can be increased from $\sim 10^{-10}$ [cis-(CH)$_x$]-10^{-5}

[<u>trans</u>-$(CH)_x$] $(\Omega \text{ cm})^{-1}$ [= S/cm] to greater than 4×10^4 S/cm [3,12,33], comparable to the conductivity of good metals (*e.g.*, $\sigma_{DC} \sim 4.8 \times 10^4$ S/cm for lead and 5.9×10^5 S/cm for copper at room temperature [34]). Recent advances in the processing of other conducting polymer systems has led to improvements in their σ_{DC}, to the range of $\sim 10^3$ S/cm [3,5,22,24,33,35]. With such high conductivity, conducting polymers become useful for applications as wires, in electromagnetic shielding, and for electrostatic dissipation [3], with the advantages that conducting polymers are light weight and facilitate recycling, as compared with metallized polymers [1].

Accompanied by the enhancement in σ_{DC}, many traditional signatures of an intrinsic metallic nature have become apparent, including negative dielectric constants [3,18,33,36], a Drude metallic response [18,23,33,37,38], temperature independent Pauli susceptibility [33,39–45], and a linear dependence of thermoelectric power on temperature [46–48]. However, the conductivities of even the new highly conducting polymers, though comparable to traditional metals at room temperature, generally decrease as the temperature is lowered [3,5,33,35]. Some of the most highly conducting samples remain highly conducting even in the millikelvin range [35,38,49] demonstrating that a truly metallic state at low temperature has been attained.

These metallic features have been reported in conducting versions of both polyaniline and polypyrrole. The ability to process PAN doped with camphorsulfonic acid (CSA) from solution [17,50] has resulted in free standing films with high conductivity ($\sigma_{DC} \sim$ 100-400 S/cm) [37,51] which span the insulator-metal transition (IMT) even at low temperature [38,49]. Some samples of electrochemically prepared polypyrrole doped with hexafluorophosphate (PF_6) are metallic to low temperature [22,35]. However, when PPy is synthesized using different dopants or at high temperatures, the materials are more disordered and show insulating behavior [22–24,52,53]. Similar results are reported in the literature for conducting polyacetylene [35].

The transport properties of conducting polymers are highly dependent upon the structural disorder arising from sample quality, doping procedure, and aging [3,33]. In doped

4

polyacetylene [35], polypyrrole [35], and polyaniline [38], studies of the millikelvin resistivity ($\rho = 1/\sigma$) showed the conductivity is thermally activated in strongly disordered films, the resistivity appears like that of a disordered metal ($\rho \propto \log T$) for samples of intermediate conductivity, and that ρ has a very weak temperature dependence for the weakly disordered state. Careful studies of the microwave dielectric contant in polyaniline as the crystallinity of the films improves demonstrate that the carriers become more delocalized as the structural order is improved [18]. Variation of the solvent from which PAN-CSA is cast yields a change in the local order in the polymer [54–56] and a concomitant change in the crystallinity of the films, with the transport properties showing stronger localization as the crystallinity decreases [55,56]. Even the most metallic samples are not single crystals. Doped polyacetylene has a complex fibrillar morphology with $\sim$ 80-90 % crystallinity, while doped PAN and doped PPy have 50 % crystallinity at best [54].

The effect of the disorder and the one-dimensionality of the polymer on the nature of the metallic state and the insulator-metal transition are still strongly debated. Disorder [57,58] and one-dimensionality [58] lead to localization of the electron wavefunctions. Even if the polymer chains are well ordered, macroscopic transport is impossible unless the carrier can hop or diffuse to another chain to avoid the chain breaks and defects [59]. Previous theoretical calculations [36,60,61] as well as experimental work [18,20,36] have stressed the importance of interchain interaction and three-dimensionality of the electron states in highly conducting polymers to avoid one-dimensional localization. There is evidence that the metallic states are three-dimensional, though the transport properties are highly anisotropic [59,62–64]. The nature of the disorder is still an important question. Disorder can result in different properties depending on whether it is homogeneous or inhomogeneous.

The wavefunctions of the charge carriers may become localized to a few atomic sites if the disorder is strong enough. The behavior of a uniformly disordered material near an insulator-metal transition has been discussed in the context of an Anderson transition [57,58,65]. For a three-dimensional system, when the disorder potential becomes comparable to the electronic bandwidth, a mobility edge exists which separates localized from extended

states [57,58]. If the Fermi level (E_F) lies in the region of extended states, σ_{DC} is finite [58] and the logarithmic derivative of the conductivity [$W \equiv d\ln\sigma_{DC}/d\ln T$] [66] has a positive slope at low temperature. When E_F lies in the range of localized states, the carriers have a hopping behavior (where $\sigma_{DC} \rightarrow 0$) [58] and the W function has a negative slope at low temperature [66]. Also, the dielectric function is positive due to the polarization of the localized state. The strong disorder necessary to cause localization of 3D electronic wavefunctions necessarily limits the mean free time (τ) to be small. As the IMT is crossed, the electronic localization length (L_{loc}) diverges and the system monotonically becomes more metallic, displaying higher σ_{DC} with weaker temperature dependences. However, τ varies slowly with energy in crossing the IMT [67]. Therefore, τ remains short close to the IMT. In fact, the Ioffe-Regel condition requires that $k_F\lambda \sim 1$ for a material near an IMT [68], where k_F is the fermi wavevector and λ is the mean free path. This implies that the scattering time $\tau \sim 10^{-15}$ s. For such short scattering times, the frequency dependent conductivity [$\sigma(\omega)$] is monotonically suppressed at low frequency. Also, localization corrections to the metallic Drude response result in a positive dielectric function [$\epsilon(\omega)$] for short τ at low frequency, rather than the negative low frequency $\epsilon(\omega)$ of normal metals [34,69].

In contrast, if the disorder is inhomogeneous with large variations on the length scale of or larger than the characteristic electron localization lengths, then the behavior expected for a composite system may be expected. The Inhomogeneous Disorder Model [23,33,36,37] treats the metallic state of conducting polymers as a composite system comprised of metallic ordered regions (with delocalized charge carriers) coupled by disordered quasi-one-dimensional regions through which hopping transport along and between chains occurs. Localization occurs in the disordered regions due to the one-dimensional electronic nature of the polymer chains in this region. When the polymer chains in the disordered region are tightly coiled, the in-chain localization length is short and coupling between metallic regions is poor, so that free electrons are confined within the metallic regions [3,18,33,37,55,56,70,71]. The temperature dependent transport is then dominated by hopping and phonon induced delocalization in the disordered regions [36] or even tunneling between metallic islands [72]

6

depending upon the morphology. When the polymer chains in the disordered regions are sufficiently straight (*i.e.*, larger radii of curvature or longer persistance lengths), the in-chain localization length is larger than the typical separation between metallic islands and carriers are able to diffuse macroscopically among the metallic regions [18,37,70,71]. In this case, a fraction of the carriers will percolate through the ordered paths. Just as in the Anderson transition, there is a crossover in slope for the W plot as percolation occurs, though the IMT is no longer necessarily a monotonic function of the room temperature σ_{DC} [37,70]. In this model, the magnitude of σ_{DC} depends on the number of well coupled metallic regions across the sample. On the metallic side of the IMT, a fraction of the carriers will demonstrate free carrier response even at low temperature. Due to phonon-induced delocalization in the disordered regions, a fraction of the carriers may appear percolated at room temperature even for samples on the insulating side of the IMT [37,70].

To determine the nature of the metallic state in conducting polymers, it is necessary to use a wide variety of probes. DC transport measurements provide insight into the insulating or metallic nature of electrons at the Fermi level. Measurement of high frequency transport provides an important probe away from the Fermi energy to help discriminate between the homogeneously and inhomogeneously disordered metallic state [6,37]. For instance, $\epsilon(\omega)$ and the microwave dielectric constant (ϵ_{MW}) can be used to determine the presence of Drude (free carrier) dispersion in the electrical response of the sample as well as the plasma frequency of the free carriers [3,18,23,33,37]. This free carrier behavior can be monitored as a function of processing and temperature. Also, $\epsilon(\omega)$ and the optical frequency conductivity [$\sigma(\omega)$] provide probes of the scattering times and mean free paths for the samples as the IMT is crossed.

In this chapter, coordinated studies of the temperature dependent DC, optical (2 meV - 6 eV), and microwave (6.5 GHz) transport on two different polymers systems, polyaniline (PAN) and polypyrrole (PPy), are emphasized. From a comparison of this set of experiments with the reports in the literature for polyacetylene, it is determined that there is a universal behavior of the metallic state in conducting PAN, PPy, and $(CH)_x$. The metallic

state is characterized by a small fraction of carriers which are delocalized down to low T with long mean free times ($\tau > \sim 10^{-13}$ s) and a large majority of carriers which are more strongly localized ($\tau_1 \sim 10^{-15}$s). These delocalized electrons result in a weak temperature dependence for σ_{DC} down to mK temperatures. This metallic state is strongly dependent on structural order. More disordered polymers show strong localization and hopping (insulating) transport. We conclude that, though the insulator-metal transition is due to structural disorder, it is not due to a conventional homogeneous Anderson transition. We propose that the insulator-metal transition is instead better described by the Inhomogeneous Disorder Model.

II. MODELS FOR LOCALIZATION AND METALLIC CONDUCTIVITY

It is established experimentally that a finite density of states at the Fermi level [$N(E_F)$] can be induced by doping [3,7,15,33,39–43]. Even though there is a high density of conduction electrons at the Fermi level for the highly doped state, the carriers may be spatially localized so they cannot participate in transport except through hopping. The prime source of localization is structural disorder in the polymers [3,33,54]. X-ray diffraction studies of these systems show that they are generally of modest crystallinity, with regions of the material which are more ordered while other regions are more disordered [52,54,73,74]. Also the fibrillar nature of many of the conducting polymers may lead to localization by reducing the effective dimensionality of the electrons delocalized in a bundle of polymer chains [61]. In the following sections, the effect of inhomogeneous and homogeneous structural disorder on the resulting transport properties of the disordered metallic state will be discussed.

A. Inhomogeneous Disorder Induced Insulator-Metal Transition

Conducting polymers generally display a rich variety in their morphology [54], being partially crystalline and partially disordered as shown schematically in Figure 3. If the localization length in the more disordered regions of the electrons (L_{loc}) is comparable or small

8

compared to the crystalline coherence lengths ($\sim 10^1$ Å) in the polymer, then the disorder present in the conducting polymer is viewed as inhomogeneous [3,23,33,37,70]. The localization effects in the inhomogeneously disordered (partially crystalline) conducting polymers is proposed to originate from quasi one dimensional localization in the disordered regions [18,23,33,36] which surround the ordered regions. It is well known for a one-dimensional metallic chain that the localization of charge carriers arises for even weak disorder because of quantum interference of static back-scattering [58], with the L_{loc} increasing as the disorder decreases. For quasi-one-dimensional conducting polymers, the transfer integral perpendicular to the chain axis is crucial. As the polymer chains are finite, if the carrier can not diffuse to another chain before being reflected back onto itself and thus experiencing quantum interference, then the polymer will not be a conductor. This leads to the condition $w_\perp > 1/2\tau$, where $w_\perp$ is the interchain transfer rate and τ is the mean free time, to avoid quasi-one-dimensional localization [59].

Prigodin and Efetov studied the insulator-metal transition of these quasi-one-dimensional conducting polymers using a random metallic network (RMN) model [61] to represent weakly connected, fibrous bundles of metallic chains. In this zero temperature model, the phase transition from insulating to metallic behavior is a function of the cross-section of electronic overlap between fibers (α), and the product ($\rho = pL_{loc}$) of the localization radius (L_{loc}) and the concentration of crosslinks between fibers (p). The metallic state can be induced by strengthening the interchain (or interfibril) interaction (increasing α), increasing the density of crosslinks between fibers (increasing p), or increasing the localization length (increasing L_{loc}). This model developed for contacts between fibers comprised of parallel polymer chains can be generalized to the three-dimensional delocalization transition that occurs in inhomogeneously disordered (partially crystalline) nonfibrillar polymers [3,33]: the metallic state is induced as the strength of connection between ordered or crystalline regions (α) is increased, as the density of interconnections between ordered or crystalline regions (p) increases, and as the localization length within the disordered regions (L_{loc}) increases. L_{loc} depends upon the

9

morphology of the disordered region. Figure 3 (b) schematically shows examples of rod-like and coil-like chain morpholgies [50]. L_{loc} will be larger (smaller) for the rod-like (coil-like) morphology. Within this model, conduction electrons are three-dimensionally delocalized in the "crystalline" ordered regions (though the effects of paracrystalline disorder may limit delocalization within these regions [75]). In order to transit between ordered regions, the conduction electrons must diffuse along electronically isolated quasi-one-dimensional chains through the disordered regions where the electrons readily become localized.

Because the IMT depends upon the coupling between metallic regions, the Inhomogeneous Disorder model resembles a percolation transition. The main difference between percolating conducting polymers and more traditional percolating system such as silver particles in potassium chloride is that the conducting polymer "crystals" do not have sharp boundaries. As a single polymer chain can be a part of both metallic "crystalline" regions and quasi-one-dimensional disordered regions, the percolating object is a fuzzy ellipsoid [3,37]. When L_{loc} is greater than the average distance between metallic regions, carriers may diffuse among the metallic regions and an IMT occurs. If L_{loc} is temperature dependent due to phonon assisted processes [36], it is possible to show the behavior of a percolated metallic system at high temperatures (L_{loc} greater than the average distance between metallic islands) and the behavior of an unpercolated insulating system at low temperature (L_{loc} less than the average distance between metallic islands).

The dependence of the conductivity on transport through quasi-one-dimensional chains leads to some profound effects. For an ordered quasi-one-dimensional metal with its highly anisotropic electronic fermi surface, σ is given in the chain direction by

$$\sigma_{\parallel} = (e^2 na/\pi\hbar)v_F\tau = (e^2 na/\pi\hbar)(\lambda/a).\tag{1}$$

where n is the conduction electron density per unit volume, a is the interatomic distance in the chain direction. $v_F = 2t_0 a/\hbar$, t_0 is the electron hopping element along the chain. and τ is the mean free time. Kivelson and Heeger [76] have shown that only $2k_F$ phonons can relax the momentum of the electrons for a quasi-one-dimensional chain from which the counter

10

ions are spatially removed and therefore effectively screened. Since the $2k_F$ phonons have a relatively small thermal population (due to their high energies ~ 0.1 eV), the conductivity is predicted [76] to be quite high at room temperature ($\sim 2 \times 10^6$ S/cm for polyacetylene) and increase exponentially upon cooling. A small interchain hopping integral $t_\perp \sim 0.1$ eV is all that is necessary to obtain three-dimensional delocalization of carriers and the resulting metallic state may take advantage of this large quasi-one-dimensional (1D) conductivity. The lack of effective scatterers in an ordered quasi-one-dimensional metal may lead to an anomalously long scattering time [18] compared with conventional 3D metals.

In a real system, disorder scattering must be taken into account as the DC conductivity is limited by the least conducting (most disordered) part of the conduction path. In disordered quasi-1D conducting polymers, static disorder scattering (with scattering time $\tau_{imp}(2k_F)$) as well as $2k_F$ phonons (with scattering time $\tau_{ph}(2k_F, T)$) can relax momentum. The effect of phonon-induced delocalization (scattering time $\tau_{ph}(0, T)$), which increases the conductivity with increasing temperature, must be taken into account. Within this model [36], the T dependent DC conductivity is given by

$$\sigma_{DC}(T) = \frac{\Omega_p^2}{4\pi}\tau_{tr}(T)\frac{[f(T) - 1]}{[f(T) + 1]}, \tag{2}$$

where $\Omega_P^2 (= 4\pi n e^2/m^*)$ is the carrier plasma frequency, τ_{tr} is the effective transport scattering time determined via Matthieson's rule

$$\frac{1}{\tau_{tr}(T)} = \frac{1}{\tau_{imp}(2k_F)} + \frac{1}{\tau_{ph}(2k_F, T)}, \tag{3}$$

and

$$f^2(T) = 1 + 4\frac{\tau_{imp}(2k_F)}{\tau_{ph}(0, T)}. \tag{4}$$

The behavior with temperature of the scattering times and the resultant $\sigma_{DC}(T)$ [77] are shown in Figure 4. In well ordered materials, it is possible for $\tau_{imp}(2k_F) > \tau_{ph}(2k_F, T)$ near room temperature. Therefore, τ_{tr} is dominated by inelastic phonon scattering near room temperature. Since $\tau_{ph}(2k_F, T)$ increases with decreasing temperature, σ_{DC} increases with

11

decreasing T, similar to the behavior of metallic systems. When $\tau_{imp}(2k_F) < \tau_{ph}(2k_F, T)$, localization effects begin to dominate (phonon induced delocalization is important), resulting in a suppression in σ_{DC} at lower temperatures and a consequent maximum in $\sigma_{DC}(T)$, Fig. 4. For weaker disorder [longer $\tau_{imp}(2k_F)$], this maximum in σ_{DC} is shifted to lower temperature. At even lower temperature, if $\tau_{imp}(2k_F) > \tau_{ph}(0, T)$, there is a crossover to a more strongly localized hopping conductivity. This model accounts for localized behavior at low temperature despite conductivities at room temperature in excess of the Mott minimum conductivity. Only the most delocalized electrons on the percolating network contribute to the high DC conductivity. (The more localized electrons lead to a conductivity less than $\sim$ 10 S/cm [70].) The fraction of delocalized carriers can be determined from high frequency measurements.

For a truly metallic system, the DC conductivity will remain finite as $T \to 0$ [58] and the logarithmic derivative of the conductivity ($W = d\ln\sigma_{DC}(T)/d\ln T$) will show a positive slope at low T [66]. In contrast, for an unpercolated system, the DC conductivity will decrease rapidly at low T and the W plot will have a negative slope, characteristic of hopping systems. In the Inhomogeneous Disorder Model, the W plot will show a crossover in the low T slope for the W plot from negative to positive, though the IMT is not necessarily a monotonic function of the room temperature σ_{DC} due to its dependence on the density and strength of connections between metallic regions and the localization length of electronic states in the disordered regions.

Effective medium theories characterize the frequency dependent transport in systems with large scale inhomogeneities such as metal particles dispersed in an insulating matrix [78,79]. An IMT in the effective medium model represents a percolation problem where a finite σ_{DC} as $T \to 0$ is not achieved until metallic grains in contact span the sample. To understand the frequency dependence of the macroscopic material, an effective medium is built up from a composite of volume fraction f of metallic grains and volume fraction $1 - f$ of insulator grains. The effective dielectric function [$\epsilon_{EMA}(\omega)$] and conductivity function [$\sigma_{EMA}(\omega)$] are solved self-consistently.

12

The characteristic composite behavior of $\sigma_{EMA}(\omega)$ for a medium consisting of spherical particles with volume fraction f of Drude conductor and $1 - f$ of insulator is shown in Figure 5. For a volume fraction f less than the percolation value ($f = 1/3$ for spheres), $\sigma_{EMA}(\omega)$ is dominated by an impurity band of localized plasmon-like excitations. As the system approaches the percolation threshold, the localized peak in $\sigma_{EMA}(\omega)$ shifts to lower frequency. Above the percolation threshold, a Drude peak corresponding to the carriers which have percolated through the composite structure occurs at low frequency. Only a fraction $[\sim (3f - 1)/2$ [79]] of the full conduction electron plasma frequency appears in the Drude peak, depending upon the proximity to the percolation threshold. The same percolating free electron behavior is observable in the dielectric response $\epsilon_{EMA}(\omega)$ for the system.

This characteristic behavior for traditional composites is expected to be modified for conducting polymer composites. As mentioned earlier, the geometry of the percolating objects resemble fuzzy ellipsoids with large aspect ratios rather than spheres. Also, phonon assisted transport in the disordered regions of the conducting polymer (which are the insulating regions) may give the appearance of percolation in $\sigma(\omega)$ and $\epsilon(\omega)$ at room temperature even though a particular system may not truly be metallic at low T [37,70]. For both $\sigma(\omega)$ and $\epsilon(\omega)$, the distinct behavior of localized and delocalized charge carriers will be evident above percolation. Specifically for percolated samples, $\sigma(\omega)$ will increase and $\epsilon(\omega)$ will become increasingly negative with decreasing frequency below the uncreened free carrier plasma frequency Ω_p ($= \sqrt{4\pi\delta n e^2/m^*}$, where n is the full charge carrier density, δ is the fraction of the charge carrier density which is delocalized, ϵ is the electronic charge, and m^* is the effective mass of the delocalized carriers). The response of localized carriers (the localized plasmon-like excitations) will occur for frequencies less than the "full" unscreened plasma frequency Ω_{p1} ($= \sqrt{4\pi n e^2/m_1^*}$, where m_1^* is the averaged effective mass of the carriers) [37,70]. The anomalously long scattering times possible for quasi-1D systems may lead to huge negative dielectric functions at low frequency.

13

B. Anderson Disorder Induced Insulator-Metal Transition

It is useful to decribe the form of localization which occurs in a homogeneously disordered material in contrast to the model described in the previous section. The three-dimensional models described below assume that the materials are isotropic; i.e., the materials should be electrically the same in all directions. In a perfect crystal with periodic potentials. the wavefunctions form Bloch waves which are delocalized over the whole solid [34]. In systems with disorder, impurites and defects introduce substantial scattering of the electron wave function which may lead to localization. Anderson demonstrated [57] that electronic wave functions can be localized if the random component of the disorder potential is large enough ccmpared with the electronic bandwidth, Figure 6. In this case, the localized wavefunctions have the form

$$\Psi(\mathbf{r}) \propto exp(-\mathbf{r}/L_{loc})Re(\Psi_0). \tag{5}$$

where L_{loc} is the localization length of the state. Later, Mott showed that band tail states are more easily localized than states in the center of the band [58]. Therefore, a critical energy called the mobility edge (E_c) exists which separates localized states in the band tails from extended states in the center of the band. Fig. 6. The resulting electronic behavior of a material depends on where the Fermi energy (E_F) lies relative to E_c. If E_F lies in the range of extended states. then $\sigma_{DC}(T)$ is finite as $T \to 0$ [58] and the W plot has a positive slope at low temperature [66]. If the disorder potential is strong enough to cause E_F to be in the range of localized states, then the material will be non-metallic, with $\sigma_{DC} \to 0$ as $T \to 0$ [58] and a negative slope for the low T W plot [66], even though there is a finite density of states at E_F.

When E_F approaches E_c on the insulating side of the IM transition, the localization length L_{loc} diverges as the electronic wavefunction becomes delocalized through the material. However, because of the strong disorder. the mean free path (λ) is still very short. In 1960. Ioffe and Regel [68] proposed that the lower limit for the metallic mean free path is the

interatomic spacing, which occurs at and on the insulating side of the IMT. This condition led Mott to propose a minimum metallic conductivity ($\sigma_{min} \sim 0.03e^2/3\hbar a \sim 10^2$ S/cm in three dimensions, where a is the interatomic spacing). The Ioffe-Regel condition implies that $k_F\lambda \sim 1$ (k_F is the Fermi wavevector), when $\sigma_{DC} \sim \sigma_{min}$. If applied to conducting polymers, this leads to a very short mean free path and scattering time. For typical repeat distances along the polymer chain in doped PAN [54] (other doped conducting polymers have similar values), the Ioffe-Regel condition requires that

$$\lambda \sim 1/k_F \sim 1/(\pi/2(10\text{Å})) \sim 10\text{Å}, \tag{6}$$

and

$$\tau = \lambda/v_F \sim (10\text{Å})/(10^6 m/s) \sim 10^{-15}s. \tag{7}$$

Far into the metallic regime where transport is due to diffusion of carriers in extended states, $k_F\lambda \gg 1$.

When the Fermi level lies in the localized region, the conductivity at zero temperature is zero even for a system with a finite density of states. The transport at higher temperature involves phonon activated hopping between localized levels. The Mott variable range hopping (VRH) model is applicable to systems with strong disorder such that ΔV (disorder energy) $\gg B$ (band width) [58]. The general form of the temperature dependent conductivity of Mott's model is described as

$$\sigma = \sigma_0 \exp[-(\frac{T_0}{T})^{1/d+1}] \tag{8}$$

where d is the dimensionality and, for three-dimensional systems, $T_0 = c/k_B N(E_F)L^3$ (c is the proportionality constant, k_B the Boltzman constant, and L the localization length). In Mott's model, electron correlations are neglected as for the classical Fermi liquid. Efros and Shklovskii pointed out that the interactions between localized electrons and holes play an important role in the hopping transport, especially at low temperature [80], changing the expected temperature dependence of the conductivity to

$$\sigma = \sigma_0 \exp[-(\frac{T_0'}{T})^{1/2}] \qquad (9)$$

where $T_0' = e^2/\epsilon L$ (e is the electron charge, and ϵ is the dielectric constant). For materials very close to the IM transition, instead of an exponential temperature dependence, a conductivity with a power law temperature dependence is predicted [81].

Typical behavior for the evolution of the temperature dependent resistivity (ρ) as E_F crosses E_c is shown in Figure 7 for p-doped germanium as a function of the compensation (carrier density) [58]. For the material with the largest compensation (smallest carrier density), ρ has the largest magnitude and strongest temperature dependence. As the compensation is decreased (carrier density is increased), ρ decreases monotonically in magnitude and the temperature dependence decreases monotonically. For the most metallic sample, ρ shows a very weak T dependence at low temperature. This monotonic evolution for the magnitude and T-dependence of σ ($= 1/\rho$) is characteristic of an Anderson IMT [58].

At high frequencies, $\sigma(\omega)$ for ordered materials is given by the Drude formula

$$\sigma_{Drude}(\omega) = \frac{\Omega_p^2 \tau}{4\pi(1 + \omega^2 \tau^2)}, \qquad (10)$$

where $\Omega_p (= \sqrt{4\pi n e^2/m^\star})$ is the plasma frequency of the free electrons, n is the full carrier density, and $m^\star$ is the effective mass. This behavior follows from the Kubo formula when the mean free time (τ) is such that $\omega\tau \gg 1$ and breaks down when $\omega\tau \sim 1$ [58,82]. For three-dimensional materials near an Anderson IMT, $\sigma(\omega)$ is suppressed at low frequencies relative to $\sigma_{Drude}(\omega)$ due to quantum interference of the electronic wavefunctions [83,84]. Localization corrections to σ_{Drude} calculated within scaling theories of the Anderson transition [58,65,84–87] yield the localization modified Drude model:

$$\sigma_{LMDM}(\omega) = \sigma_{Drude}(\omega)(1 - \frac{C}{(k_F\lambda)^2}[1 - \frac{\lambda}{L(\omega)}]), \qquad (11)$$

where C is an undetermined universal constant (~ 1), k_F is the Fermi wavevector, λ is the mean free path, and $L(\omega)$ is the distance a charge would diffuse during an oscillation of the electromagnetic wave. It is noted that in this model at zero frquency, the high DC

conductivity of a sample near the IMT is due to localized charge carriers. Since in three dimensions,

$$L(\omega) = \sqrt{\frac{D}{\omega}}, \tag{12}$$

where $D = \lambda^2/3\tau$ is the diffusion constant, the localization modified Drude model can be written as

$$\sigma_{LMDM}(\omega) = \sigma_{Drude}(\omega)[1 - \frac{C}{(k_F v_F \tau)^2} + \frac{C(3\omega)^{1/2}}{(k_F v_F)^2 \tau^{3/2}}]. \tag{13}$$

The real part of the dielectric function ($\epsilon_{LMDM}(\omega)$) corresponding to the localization modified Drude model can be calculated using the Kramers-Kronig relations, giving

$$\epsilon_{LMDM}(\omega) = \epsilon_\infty + \frac{\Omega_p^2 \tau^2}{1 + \omega^2 \tau^2}[\frac{C}{(k_F v_F)^2 \tau^2}(\sqrt{\frac{3}{\omega \tau}} - (\sqrt{6} - 1)) - 1], \tag{14}$$

where ϵ_∞ is the dielectric screening due to higher energy interband transitions. It is noted that these expressions are not complete since they ignore cutoffs at low frequency when $L(\omega) \sim L_T$, where L_T is the Thouless length [67].

The behavior of both $\sigma_{LMDM}(\omega)$ and $\epsilon_{LMDM}(\omega)$ for materials close to the IMT is determined in the Anderson model by the Ioffe-Regel condition which requires $\tau \sim 10^{-15}$ s. $\sigma_{LMDM}(\omega)$ and $\epsilon_{LMDM}(\omega)$ are shown as the mean free time τ ($\sim 10^{-15}$ s) is varied in Fig. 8. $\sigma_{LMDM}(\omega)$ has Drude dispersion at high frequency, a maximum, and then monotonic suppression at low frequencies. As τ increases (reflecting a more ordered material), the Drude dispersion occurs over a wider frequency range and the maximum shifts to lower frequency. An important consequence of the localization modified Drude model is that $\epsilon_{LMDM}(\omega)$ becomes positive at very low frequencies, reflecting the short τ due to strong disorder scattering. This behavior should be contrasted with the negative value of $\epsilon(\omega)$ for the Drude model at low frequency ($\omega \ll 1/\tau$)

$$\epsilon_{Drude} \simeq \epsilon_\infty - \Omega_p^2 \tau^2. \tag{15}$$

17

III. EXPERIMENTAL TECHNIQUES

A. Chemical Preparation

The final structural order and hence the electronic properties of conducting polymers is sensitive to preparation techniques. The high quality free standing films of polyaniline emeraldine base (EB) doped with d,1-camphorsulfonic acid (CSA), for which data is presented here, were prepared using EB synthesized to provide different molecular weights [88]. Low molecular weight polyaniline, $\bar{M}_W <\sim 100,000$ was prepared by a well known route [55,56,88]. Polyaniline of high molecular weight, $\bar{M}_W >\sim 300,000$ was synthesized [88] by adding lithium chloride (LiCl) to the reaction vessel and lowering the temperature of the reaction. All molecular weights were determined by gel permeation chromatography using a 0.5% weight per volume LiCl/N-methyl pyrrolidone (NMP) solvent and a polystyrene standard.

In order to obtain fully doped polyaniline salt, the molar ratio of EB to the dopant (CSA) should be 1:2, assuming that all of the dopant ions succesfully protonate an imine nitrogen. For example 1.0 gram (0.00276 mole) of EB would be mixed with 1.287 gram (0.00552 mole) of HCSA. The EB and HCSA was mixed in two different ways. For some films, the EB and HCSA were mixed as powders using a mortar and pestle. This doped EB-CSA powder could then be dissolved in appropriate solvent mixtures. For the data reviewed here, these powders were dissolved in *m*-cresol or chloroform or mixtures of these solvents. The resulting properties were shown to vary dramatically depending on which solvent was used through the effects of secondary doping [55,56,88]. The alternate way of obtaining solutions of doped PAN-CSA is to separately add the EB powder into a volume of solvent and the HCSA into a volume of solvent and then mix the two solutions.

Also the concentration of PAN-CSA in the solvent was varied from 1-3 weight percent (wt %) as the amount of solvent which must evaporate from the resulting film has an effect on the structural order of the film. When the solution of PAN-CSA was prepared, it was

stirred overnight with a magnetic stirrer and then sonicated for $\sim$ 2 hours to completely dissolve all visible particles. The solution was then filtered and cast on a microscope slide upon which it dried in a hood. The resulting films could be peeled from the microscope slide to obtain free standing films of approximate thickness $\sim$ 40-100 μm. All polyaniline samples for which data are reported here were prepared in the labs of Alan G. MacDiarmid at the University of Pennsylvania. The details of the effects of different processing conditions on the free standing films are given in reference [88]. For this study, a sampling of these films were chosen which illustrate the properties of PAN-CSA as the transport properties approach and cross the insulator-metal transition. The samples for this study are listed in Table I along with their specific processing conditions.

The polypyrrole films which were doped with hexafluorophosphate (PF_6) and p-toluenesulfonate were obtained by anodic oxidation of pyrrole at -30 degrees Celcius under potentiostatic conditions. The electrolytic cell contained 0.06 moles per liter (mol/L) of pyrrole and 0.06 mol/L of the appropriate salt in propylene carbonate containing 1 vol% of water. A glassy carbon plate was used as the anode and a platinum foil was used as the anode. The current was adjusted to $\sim$ 0.125 mA/cm^2. The reaction took place for $\sim$ 24 hours under a stream of nitrogen gas. For PPy(PF_6) and PPy(TsO), elemental analyses determined that there is approximately one dopant per three pyrrole rings [22,24,35].

The polypyrrole film doped with sulfonated polyhydroxyether (S-PHE) [89] was synthesized on rotating stainless steel electrodes in a solution of 0.05 mol/L S-PHE, 5 vol % pyrrole, and 1 vol % water in propylene carbonate (PC) under galvanostatic conditions using a current density of 2 mA/cm^2. The film was peeled, washed with PC and ethanol and then dried under vacuum at 50 degrees celcius for 12 hours. The molar ratio of sulfonation is defined as $MR = n/(n + m)$, where n is number of sulfonated polyhydroxyether segments and m is the number of unsufonated polyhydroxyether segments as shown in Figure 9. For samples with low molar ratios, a large fraction of the volume of the polymer is occupied by the PHE, a saturated polymer which does not transport electrical charge effectively. Thus, a large volume of insulator is added to the film, drastically reducing the conduction elec-

19

tron density and the interaction between chains. Data presented here is from a study of a PPy(S-PHE) film with $MR = 0.125$ [53,89].

In general, data presented here is for samples that are under vacuum or "pumped" conditions that substantially reduce or eliminate effects of weakly bound moisture or solvents.

B. Transport Measurements

The dc conductivity (σ_{DC}) measurements were performed using a four probe technique as described previously [59]. Four thin gold wires (0.05 mm thick with 99.9 % purity) were attached to the sample surface using a graphite paste (Acheson Electrodag 502) to improve the electrical contact. By placing the sample probe in a Janis DT dewar with He exchange gas, $\sigma_{DC}(T)$ could be measured from 4.2-300 K. Measurements at mK temperatures were carried out by placing the sample probe in thermal contact with the mixing chamber of a ^{3}He-^{4}He dilution refrigerator [49]. The mK conductivity measurements were carried out using a low frequency $\sim$ 19 Hz alternating current and a lockin amplifier. A magnetic field of 0-5 Tesla was applied perpendicular to the plane of the samples.

Reflectance spectra from 2 meV-6 eV were recorded as reported previously [23]. The high energy (0.5-6eV) reflectance was recorded using a Perkin Elmer λ-19 UV/Vis/NIR (ultraviolet/visible/near infrared) spectrometer equipped with a Perkin Elmer RSA-PE-90 reflectance accesory based on the Labsphere DRTA-9a integrating sphere. The low energy (2 meV-1.2 eV) reflectance measurements were made on a BOMEM DA-2 Fourier Transform Infrared (FTIR) spectrometer equipped with a homemade cryostat which could be lifted so that a reference mirror and sample could be placed alternately in the IR beam. A Michelsen interferometer (1-12 meV) was used to record temperature dependent far IR reflectance spectra [38]. The measured reflectance spectra from the different spectrometers typically agreed to within 1 % in the regions of overlap for samples with highly specular surfaces.

The samples were free standing films with thickness $\sim$ 40-100 μm. This thickness is greater than the electromagnetic penetration depth ($\delta = c/\sqrt{2\pi\mu\omega\sigma(\omega)}$, where c is the

speed of light and $\sigma(\omega)$ is the conductivity at frequency ω) when $\sigma_{DC} > \sim 10$ S/cm. Samples with $\sigma_{DC} < 10$ S/cm were first checked to determine whether they transmitted far infrared radiation. Therefore, the reflectance can be analyzed using the Fresnell reflection coefficients for semi-infinite media [69].

The optical conductivity $[\sigma(\omega)]$ and the real part of the dielectric function $[\epsilon(\omega)]$ were calculated from the reflectance spectra using the Kramers-Kronig analysis and the Fresnell relations for semi-infinite media [69]. To calculate the optical functions using the Kramers-Kronig technique, reasonable extrapolations of the experimental reflectance data at low and high frequencies is necessary. In this study, the reflectance data were extrapolated at low energy using the Hagens-Rubens relation [69]. At high energy (6-12 eV), the reflectance spectra were extrapolated with a reflectance $R \propto \omega^{-2}$ (interband) followed by an $R \propto \omega^{-4}$ (free electron) at higher energy (> 12 eV).

The microwave conductivity and dielectric constant were measured using the cavity perturbation technique [59,71]. The resonant cavity used was a cylindrical TM_{010} cavity with a resonant frequency at 6.5 GHz. The whole cavity is inserted into a dewar filled with He gas to provide a temperature range from 4.2 - 300 K.

To understand the nature of the spins in the polymers, electron paramagnetic resonance (EPR) experiments were carried out using a Bruker ESP 300 spectrometer equipped with a TE_{102} rectangular cavity which resonates at 9.5 GHz (X band). An ESR-900 continuous flow helium cryostat from Oxford Instruments provided temperature control from 4-300 K.

IV. POLYANILINE

Polyaniline doped with camphorsulfonic acid has been shown to cross the insulator-metal transition and show metallic behavior at low temperature [49,51,90]. The proximity of the samples to the IM transition can be controlled to some degree by the processing conditions [51,55,56,88]. By using the concept of secondary doping [55,56], the electrical behavior and structural order of PAN-CSA can be varied by varying the solvent from which the film is cast

[55,56]. Also, the weight percent of the polymer in the solvent can be varied to change the resulting electrical properties of PAN-CSA. In this section, the experimental results for the low and high frequency transport near the IM transition will be discussed. For simplicity, the real part of the optical conductivity and dielectric function will be referred to as $\sigma(\omega)$ and $\epsilon(\omega)$ respectively.

A. X-ray Diffraction

Polyaniline forms a rich set of structures dependent upon the processing sequence and dopant [40,54,71,73,74,91–94]. Generally, polyaniline obtained from solution in the doped (conducting salt) form exhibits a local crystalline order of type emeraldine salt-I, ES-I. contrast, polyaniline obtained by doping powder or films cast as the base form from solution are of the ES-II type [40,71,73,93,95]. Both preparation methods lead to between a few percent and about 50 % crystallinity dependent upon details of the processing route. In addition, there are significant differences in the type of local order that exists in the disordered regions between the crystalline ordered regions, varying from liquid benzene-like, to coil-like, to expanded coil-like, to more rod-like [55,56,95,96]. For many undoped and doped polyanilines, short range local order in the disordered regions resembles that in the ordered regions [54,95].

Comparing the x-ray patterns for PAN-CSA cast from m-cresol with that of PAN-CSA cast from chloroform, there is a drastic change in the structure. In PAN-CSA (m-cresol), the repeat distance along the chain direction is ~ 9.2 Å [54]. In the PAN-CSA (chloroform), the repeat distance along the chain increases to ~ 14.2 Å, possibly due to the periodicity of a snaking chain which has undergone a "rod-like to coil-like" transition [54]. There is evidence that the benzene rings of the polyaniline tend to align very well with the plane of the free standing film, though there is less order in the stacking of layers [94]. In the most highly ordered, highest conductivity samples of PAN-CSA, a diffraction peak occurs at low scattering angles, suggesting a d-spacing of ~ 21 A [54,97] which may correspond to the

distance between 2D stacks of PAN chains separated by CSA ions [54].

For each of these systems the coherence length within the doped crystallographic regions generally is no more than 50 - 75 Å along the chain direction with smaller values in the perpendicular direction. It has been proposed that these coherent crystalline regions form metallic islands and the disordered weak links between more ordered regions are areas where conduction electrons are subject to localization, as expected for charges moving through isolated one-dimensional chains. That is, for each very highly conducting polymer system studied there are regions of one-dimensional electronic character through which conduction electrons must pass [33].

It is pointed out that subtle disorder in the ordered "crystalline" regions can have drastic effects. For example, the HCl salt of poly(o-toluidi...)[i.e., poly(methylaniline)] has similar percent crystallinity and similar size crystalline regions as HCl doped polyaniline, with the important difference of "paracrystallinity" introduced by two possible positions for the CH_3 substituted C_6 rings. That is, a rotation of the ring $180°$ about its nitrogen-nitrogen axis changes the structure. The disorder introduced disrupts the interchain interaction, leading to relatively strong localization [20,75,93]. The disorder in HCl doped poly(o-toluidine) is reduced (and the delocalization increased) through processing induced increase in structural order using fiber formation [19].

B. Magnetic Susceptibility

Magnetic susceptibility studies identify the charge storage mechanism at low doping levels, as well as the density of states at the Fermi level and the density of localized "Curie" spi.. at higher dopant levels. The magnitude of χ_{Pauli} depends on the structural order and morphology of the polymers as this affects the uniformity of the doping.

For PAN. $N(E_F)$ is finite and has been shown to increase with the level of protonic acid doping and the volume fraction of crystalline material for both the ES-I, Fig. 6, and ES-II. Fig. 7, structure [39,40]. The $N(E_F)$ differ for ES-I HCl and ES-II HCl, being 0.26 states/eV-

(C+N), and 0.083 states/eV-(C+N), respectively [59]. For highly conducting PAN-CSA (m-cresol) [44], $N(E_F) \sim 0.07$ states/eV-(C+N). Recently, a differently prepared stretched PAN doped with HCl was reported to have a much higher $N(E_F)$, ~1.4 states/eV-(C+N) [16]. Some solutions of PAN-CSA have been reported to have a Pauli-like susceptibility [98]. It has been proposed that there is primarily spinless bipolaron formation in the disordered regions, especially for ES-II materials [40]. It is also noted that oxygen and moisture can have a significant effect on both the Pauli and Curie susceptibility observed [99,100].

C. DC Conductivity

To establish that a material has undergone an insulator-metal transition, it is necessary to show that σ_{DC} is finite as $T \rightarrow 0$ [58] and that the logarithmic derivative of the temperature dependent conductivity [$W = d\ln(\sigma(T))/d\ln T$, a generalized activation energy] has a positive temperature coefficient at low temperature [66]. For a conductor very close to the insulator-metal transition, called a critical sample, the resistivity follows a power law behavior with T [81]. The plot of $\log W$ vs $\log T$ for a critical sample approaches $T = 0 K$ at a constant value, providing a dividing line between the plot of $\log W$ vs $\log T$ for insulating hopping behavior which increases with decreasing T (i.e., the slope of $\log W$ vs $\log T$ is equal to $-\gamma$ if $\sigma \propto exp(T_0/T)^\gamma$) and the plot of $\log W$ vs $\log T$ for metallic samples which decreases with decreasing T.

The W plots for PAN-CSA samples A-G are shown in Figure 10. The lettering for each sample reflects the relative behavior of the W plot for the various samples. The W plot for sample A has a positive slope at low temperature, indicating that it is metallic at low temperature. Measurements of σ_{DC} for sample A at millikelvin temperatures also show a large finite conductivity ($\sigma_{DC} >\sim 70$ S/cm) down to ~ 20 mK (discussed in greater detail in Section IV D), confirming the presence of delocalized states at the Fermi level as $T \rightarrow 0$. Therefore, sample A has crossed the IMT and is metallic. However, the remaining samples show a negative slope at low temperature, varying from -0.2 to -0.7. Table II, which

24

is characteristic of the hopping transport shown by samples which are insulating at low temperature ($\sigma_{DC}(T) = \sigma_0 \exp[-(T_0/T)^\gamma]$). As W, the reduced activation energy, grows in magnitude, the samples become more insulating and the exponent γ grows. For samples B and C γ is ~ 0.25, indicating 3D variable range hopping at low temperature. For samples D-G, $\gamma \sim 0.5$-0.7, suggesting that the localization is now more quasi-1D. Therefore, as the materials become more insulating, the charge transport becomes more characteristic of hopping on isolated chains with reduced dimensionality (in the disordered regions).

$\sigma_{DC}(T)$ for each of the samples is shown in Figure 11. $\sigma_{DC}(300K)$ and the resistivity ratio $\sigma_{DC}(300K)/\sigma_{DC}(5K) \equiv \rho_R$ are given for each sample in Table II. A wide range in ρ_R is observed. For samples A-E, $\sigma_{DC}(T)$ has a positive temperature coefficient of resistivity near room temperature [18,33,51], a maximum, and then localization effects at lower temperatures. These experimental $\sigma_{DC}(T)$ are consistent with the predictions of the inhomogeneous disorder model. The temperature at which the maximum in σ_{DC} occurs (T_M) is given for each sample in Table II. The shift of the maximum in PAN-CSA to lower temperature as the materials become more metallic (as gauged by the W plot) is consistent with PAN-CSA sample A having the least disordered conduction paths. Assuming that the materials are homogeneous, sample A is the most ordered material

Though PAN-CSA sample A shows intrinsic metallic behavior, it does not have the highest $\sigma_{DC}(300K)$ compared to sample C. In fact, samples C and D each show stronger temperature dependences for σ_{DC} than materials with lower $\sigma_{DC}(300K)$, Fig. 10 (b). This non monotonic behavior of the temperature dependence with increasing $\sigma_{DC}(300K)$ contrasts with the monotonic behavior shown in Fig. 7 for p-doped Germanium which undergoes an Anderson IMT. This non monotonic evolution of $\sigma_{DC}(T)$ is a strong argument against a homogeneous 3D Anderson IMT. Since PAN-CSA sample A is metallic while sample C is insulating at low T, $\sigma_{DC}(RT) > \sigma_{min}$, the minimum metallic conductivity, for sample C. However, sample C becomes insulating at low T.

D. Millikelvin Conductivity

The millikelvin σ_{DC} with no applied magnetic field is shown in Figure 12 along with the high temperature conductivity for samples A, B, and D. Sample A has a large finite $\sigma_{DC} > \sim$ 70 S/cm down to 18 mK. This indicates that there are extended states at E_F as $T \rightarrow 0$ for PAN-CSA sample A, *i.e.*, PAN-CSA sample A is a metal at low temperature. The remaining samples show more complex behavior at low temperature, though they demonstrate hopping behavior at $\sim$ 10 K. Sample B shows a monotonic decrease in σ_{DC} down to 18 mK. Sample D *shows a turn over in σ_{DC}* below $\sim$ 200 mK. σ_{DC} for sample D then increases and saturates at lowest temperatures. A similar increase in conductivity at low temperature has been reported for samples of polypyrrole [22–24,101,102], though the turn over was seen at $T \sim$ 5-20 K. In those materials, the increase at low temperature was ascribed to a tunneling mechanism [22,24,101]. This complex behavior implies that σ_{DC} does not go to zero as $T \rightarrow 0$ for samples B and D, even though σ_{DC} for these samples shows variable range hopping behavior at higher temperatures. Therefore, σ_{DC} does not follow variable range hopping behavior as $T \rightarrow 0$ as predicted for materials with homogeneous disorder and Anderson localization. It is conjectured that the dip in the conductivity may be due to reduced tunneling due to long wavelength phonon scattering which affects the polyaniline rings, reducing the overlap integrals and decreasing the wavefunction overlap. This saturation of σ_{DC} is not expected at low temperature for strongly disordered materials such as PAN-CSA samples F or G and PPy(S-PHE) due to larger separation between metallic regions and shorter localization lengths for chains in the disordered regions.

The behavior of the mK σ_{DC} when a magnetic field of 5 Tesla is applied is shown in Figure 13. For sample A, there is a weak *positive* magnetoconductance ($\Delta\sigma/\sigma \sim 10^{-1}$). This same behavior was reported for doped polyacetylene [35,47] and polypyrrole [49] which were highly conducting at mK temperatures. For these samples, a positive magnetoconductance was attributed to magnetic field destruction of weak localization effects [35,47] (quantum interference of electronic wavefunctions leading to standing wave patterns or lo-

calization [65]). In such a model, the increase in σ_{DC} with increasing T may be seen as a result of activating parallel conduction paths through phonon scattering induced destruction of weak localization in those parallel pathways. Positive magnetoconductance is also predicted for enhanced delocalization on percolating structures due to increased magnetic energy in the metallic regions [103]. Sample B also shows a positive magnetoconductance $(\Delta\sigma(H)/\sigma \sim 10^1)$ which is larger than that of sample A at low temperatures (~ 30 mK) and reduced though positive $(\Delta\sigma(H)/\sigma \sim 10^{-1})$ at higher temperatures (~ 200 mK). The larger $\Delta\sigma(H)/\sigma$ for sample B compared with A may result from paths in series (bottlenecks) with the main conduction path in which weak localization is reduced, resulting in high σ_{DC}. The magnetic field shifts the minimum of the conductivity to higher temperature in sample D. which also shows positive magnetoconductance at the lowest temperatures.

E. Reflectance

For free electron metals such as copper [69], silver [69], and aluminum [104]. the reflectance approaches unity at low frequencies and remains high up to frequencies near the conduction electron plasma frequency (Ω_{p1}) for that system. Figure 14 shows the room temperature reflectance for the samples A-G. At low energy. the reflectance approaches unity for PAN-CSA samples A-D. The value of the reflectance in the far IR at 6 meV (50 cm^{-1}) scales with σ_{DC} for that sample. Table II. providing an independent verification of the $\sigma_{DC}(RT)$ for each sample. At higher energy. the reflectance for samples A-E decreases monotonically with increasing energy to a minimum near ~ 2 eV. the conduction electron plasma frequency. Two distinct peaks are observed at higher energy near 2.8 eV and 6 eV. attributed to interband transitions within a polaron lattice [105,106].

For samples F and G. there is a strong peak at 1.5 eV. more pronounced in the lowest σ_{DC} sample G. When the peak at 1.5 eV is strong, the reflectance in the far infrared is diminished. This indicates that there is a second "localization/delocalization" transition from isolated polarons localized to one or two C_6H_4N repeat units to partially delocalized

27

charges which are proposed [62] to extend over distances of ~ 10 to ~ 100 Å.

The temperature dependent reflectance data of PAN-CSA samples A and D in the far IR are shown in Fig. 15. With decreasing T, the reflectance at ~ 2 meV is decreased relative to the room temperature reflectance while the higher energy ($>\sim 4$ meV) reflectance initially grows above the room temperature value. At the lowest T, the far IR reflectance is suppressed over the whole energy range. The difference between the metallic (sample A) and insulating (sample D) materials is the magnitude by which the reflectance is suppressed. For sample A, the far IR reflectance is suppressed by ~ 3 % from its value at RT while the suppression is ~ 10 % for sample D. This suppression of the reflectance in the far IR is consistent with the decrease of σ_{DC} at low T for each of these materials and results from the localization (trapping) at low temperature of carriers which are delocalized at room temperature.

F. Optical Conductivity

Kramers-Kronig analysis of the reflectance data provides the optical conductivity function [$\sigma(\omega)$]. We can obtain information about the conduction electrons in PAN-CSA by comparing this function with the Drude expression for free electrons and the localization models. The room temperature $\sigma(\omega)$ is shown in Figure 16 for samples A-G. In sample G there is a strong peak at ~ 1.5 eV and a weaker peak at ~ 0.6 eV. For sample F, $\sigma(\omega)$ shows that the peak at 1.5 eV is reduced and the peak in the IR has grown and the maximum has shifted to lower energy. For the samples with higher σ_{DC}, the peak at 1.5 eV is absent, indicating that it is not an intrinsic transition in the highly conducting state. Comparison of $\sigma(\omega)$ for samples E-G shows that there is an isosbestic point at ~ 1.3 eV, characteristic of composite behavior [37]. This supports directly that composite behavior occurs in bulk polyaniline.

For samples A-E, $\sigma(\omega)$ shows Drude dispersion with decreasing energy beneath ~ 1.4 eV until reaching a maximum in the mid IR. The oscillations of $\sigma(\omega)$ in the mid infrared

28

correspond to the vibrational modes of doped polyaniline. $\sigma(\omega)$ is monotonically suppressed beneath the σ_{Drude} at lower energy except for sample C. For sample C, $\sigma(\omega)$ begins to increase again with decreasing energy beneath 0.02 eV. Though the increase of $\sigma(\omega)$ in the far IR is not as rapid, the behavior is qualitatively similar to what was reported for iodine [63,64,107] and perchlorate [108] doped $(CH)_x$ where free electrons are reported. This type of frequency behavior for $\sigma(\omega)$ is qualitatively similar to that of metallic particles in an insulating matrix after percolation of the metallic particles [78]. It is indicative of a small plasma frequency of conduction electrons which are delocalized through the material. Also, Figure 16 demonstrates that the far IR $\sigma(\omega)$ scales with σ_{DC}, confirming the measured σ_{DC}

As σ_{DC} of the samples increases, the frequency at which the maximum in $\sigma(\omega)$ occurs (ω_{max}) shifts monotonically to lower energy, Table III. This shift of the conductivity peak to low energies is the same behavior the localization modified Drude model displays as the mean free time (and therefore the mean free path) grows and the Inhomogeneous Disorder model predicts as the samples near the percolation threshold. Since ω_{max} is lowest for PAN-CSA sample C, this indicates that the scattering time (mean free path) for sample C is the longest and therefore the disorder is weakest. Assuming a homogeneous material, sample C is inferred to be the most ordered sample. Recalling that the maximum in $\sigma_{DC}(T)$ implied sample A to be the most ordered, a contradiction is obtained from assuming the materials are homogeneous. Within the Inhomogeneous Disorder model, there is no contradiction. This is because $\sigma_{DC}(T)$ reflects the behavior of percolated carriers in well ordered conduction paths while the high frequency $\sigma(\omega)$ is dominated by the contribution of localized carriers, which contribute less than 10 S/cm to σ_{DC}, in disordered regions of the sample.

Drude conductivity fits to the energy range ~ 0.4-1.4 eV provide further information about the carriers. The plasma frequency (Ω_{p1}) and localized carrier scattering time (τ_1) for each of the samples, Table III, fall into the range $\Omega_{p1} \sim 1.7$ eV and $\tau_1 \sim 10^{-15}$ s. The small scattering time ($\tau_1 \sim 10^{-15}$ s) is attributed to the disorder in the polymer. This scattering time is the magnitude predicted from the Ioffe-Regel condition for materials close to a 3D Anderson IMT. However, the Anderson IMT model is not appropriate for these

29

materials. Analysis of the dielectric function $\epsilon(\omega)$, Section IV G, demonstrates that $\sigma_{DC}(T)$ in conducting polymer systems is due to a small fraction of carriers with $\tau \, > \sim \, 10^{-13}$ s which percolate through the material. The increase in $\sigma(\omega)$ for sample C in the far infrared is evidence of the percolated free electrons.

The "average" effective mass ($m^\star$) of the conduction electrons can also be calculated from knowledge of Ω_{p1} $(= \sqrt{4\pi ne^2/m^\star})$. From x-ray measurements [54], the volume of a 2 PAN ring repeat with a CSA counterion is $V \sim 760$ Å^3 assuming a unit cell with dimensions 10.4 Å (the repeat length along the chain), 3.5 Å and 21 Å(which represents the repeat distance between alternating stacks of PAN and CSA). Since there is one doped charge added per two ring repeat of PAN-CSA, $n = 1/760$ Å$^3 \sim 1.3 \times 10^{21}$ cm^{-3}. Therefore, $m^\star \sim 0.6 m_e$ (m_e is the electron mass).

Temperature dependent far IR $\sigma(\omega)$ for samples A and D are shown in Figure 17. For both samples, the trend is clear. As the temperature is lowered. $\sigma(\omega)$ first increases and then at lower temperatures is suppressed. The resulting suppression for sample D is much stronger than for sample A, in agreement with the trend in σ_{DC}. The growth and then decrease of $\sigma(\omega)$ is consistent with the localization of charges at low temperature which are delocalized at room temperature. Part of the Drude plasma frequency of free electrons is being frozen out at DC. Therefore, due to sum rules on $\sigma(\omega)$ [69], the transitions of the "frozen out" electrons must occur at higher frequency. From this point of view, sample D becomes insulating (hopping) at low temperature because the density of free electrons goes to zero at low temperatures. Sample A remains metallic at low temperatures because the free electron density is not sufficiently reduced.

G. Optical Dielectric Function

The dielectric function determined by Kramers-Kronig analysis provides information about whether the carriers are free or localized. The importance of localization is clear from $\sigma(\omega)$. As σ_{DC} increased, the mean free path clearly increased. With increasing electron

delocalization, a larger polarization of the electron gas is possible. The far IR $\epsilon(\omega)$ for samples E-G, Fig. 18 (a), is positive in the far IR, characteristic of localized carriers. The growth of the far IR $\epsilon(\omega)$ directly demonstrates the growing polarization of localized states with increasing σ_{DC}. For sample G, $\epsilon(\omega)$ is small and positive in the far IR with strong dispersion near the "localized polaron" peak at 1.5 eV. The growth of the average scattering time and mean free path is also made evident by the development of a zero crossing at ~ 1 eV. This zero crossing is termed ω_{p1} (the screened plasma frequency Ω_{p1}). When the mean free path grows, $\epsilon(\omega)$ shows Drude dispersion to lower frequencies so that $\epsilon(\omega)$ crosses zero at the screened plasma frequency of all the conduction electrons, even though localization corrections force $\epsilon(\omega)$ positive at lower frequencies. This behavior is reminiscent of the $\epsilon(\omega)$ for the localization modified Drude model, section II B. The zero crossing of $\epsilon(\omega)$ at ω_{p1} is therefore due to localized electrons.

However, the low frequency electrical response is not dominated by localized carriers for samples A-D near the insulator-metal transition. Figure 18 (b) shows $\epsilon(\omega)$ for samples A-D. In addition to the dielectric reponse of localized electrons at ~ 1 eV, a third zero crossing of $\epsilon(\omega)$ termed ω_p is evident in the far IR. For energies lower than ω_p, $\epsilon(\omega)$ remains negative as expected for free carriers. If the carriers are free electrons, then their frequency response is described by the Drude model. At sufficiently high frequencies ($\tau \gg 1/\omega$), the Drude dieletric function is given by

$$\epsilon_{Drude}(\omega) = \epsilon_b - \Omega_p^2/\omega^2, \tag{16}$$

where ϵ_b is the background dielectric response due to localized electrons and interband transitions and Ω_p is the plasma frequency for free carriers. Figure 19 shows $\epsilon(\omega)$ plotted against $1/\omega^2$ for sample A, C and D. (The plot for sample B is not shown because, though $\epsilon(\omega)$ is clearly turning toward negative values, the zero crossing is not observed in the experimental frequency range. For this sample, we do not have low enough frequency data where $\epsilon(\omega)$ is dominated only by free electrons.) The plots provide straight lines where the slope is Ω_p^2. The value of Ω_p for each of the samples is given in Table IV. The frequency

31

response of $\epsilon(\omega)$ for PAN-CSA samples A-D (*i.e.* the response of both localized carriers and delocalized carriers with long τ) is typical of percolating systems [78,79].

From Table IV, it is clear that Ω_p (the plasma frequency of free electrons) scales with σ_{DC} for each sample. This supports that the high DC conductivity and low frequency transport is controlled by the delocalized "free" carriers. Also, the scaling of Ω_p with σ_{DC} argues against the Anderson transition model for conducting polymers. Because sample C is insulating at low T, within the Anderson model, the Fermi level for sample C lies in the region of localized (hopping) states. However, sample C has a larger free electron plasma frequency (Ω_p) at room temperature than sample A which is metallic at low T and therefore has its Fermi level in the region of delocalized (free electron) states. In addition, the scaling of Ω_p with σ_{DC} argues against the negative $\epsilon(\omega)$ being due to the formation of an intrinsic many body gap as proposed for polypyrrole materials [109], especially since the negative far IR $\epsilon(\omega)$ is observed at room temperature in PAN-CSA samples.

The values obtained for Ω_p are very small compared to the full conduction electron density ($\Omega_{p1} \sim 2$ eV), suggesting that only a small fraction (n_{free}/n_{cond}) of the conduction electrons are delocalized macroscopically. This small fraction of delocalized carriers is consistent with the small number of percolation paths which occur close to the percolation threshold in composite systems. The fraction of the carriers that are delocalized can be estimated by comparing the plasma frequency of free electrons (Ω_p) with the full conduction electron plasma frequency (Ω_{p1}).

$$n_{free}/n_{cond} = (m^\star_{free}/m^\star_{cond})(\Omega_p/\Omega_{p1})^2. \tag{17}$$

This ratio is estimated in Table IV for samples A, C, and D assuming that the effective masses ($m^\star_{free}$ and $m^\star_{cond}$) are approximately the same. In each case,

$$n_{free}/n_{cond} \sim 10^{-3}. \tag{18}$$

Even assuming a tenfold increase in $m^\star_{free}$ as the free carriers may reside in a very narrow band (due to passage through the disordered regions), the fraction of delocalized carriers is

32

only on the order of 1 percent. That the current is carried by a small number of percolated paths is not surprising since high conductivities (> 10 S/cm) have been reported for PAN-CSA diluted to only 10 % in insulating PMMA [110].

Because the plots of $\epsilon(\omega)$ against $1/\omega^2$ in Fig. 19 do not show a tendency to saturate down to 10 cm^{-1}, the mean free time for the free electrons (τ) can be estimated as

$$\tau \gg 1/10cm^{-1} \sim 5 \times 10^{-13}s. \tag{19}$$

Such a huge mean free time in a disordered polymer is surprising, especially when compared with the typical room temperature scattering times for copper, $\tau \sim 10^{-13}$-10^{-14} s [34]. This small fraction is delocalized sufficiently that $k_F\lambda \gg 1$. Similar values for τ have been reported previously in doped polyacetylene [34]. The large scattering time likely results from the ramifications of an open Fermi surface as expected for an anisotropic metal [18,23,33,76] and that the usual scattering centers, being off the polymer chains, are likely screened, reducing their effectiveness. If the whole density of conduction electrons was able to diffuse with $\tau \sim 10^{-13}$ s, the dc conductivity would be $\sim 10^5$ S/cm. Using this estimate, it is suggested that substantial improvements in the electrical conductivity can still be obtained.

τ can also be estimated within the Drude model where

$$\sigma_{DC} = \Omega_p^2\tau/4\pi. \tag{20}$$

Since the free electron plasma frequency Ω_p scales with σ_{DC} the scattering time is estimated as $\tau \sim 10^{-13}$ s for samples A,C, and D. Table IV, assuming only the free electrons participate in the low frequency transport. This estimate of the free electron scattering time is in good agreement with the previous estimate. This large scattering time ($\tau >\sim 10^{-13}$ s) compares with $\tau \sim 10^{-14}$s at room temperature in copper [111]. The presence of carriers with $\tau \gg 10^{-15}$ s indicates that the low frequency carriers are not subject to the Ioffe-Regel condition which requires $\tau \sim 10^{-15}$ s in conducting polymers. This constitutes further evidence against the applicability of the Anderson IMT model.

The temperature dependence of the far IR $\epsilon(\omega)$ explicitly demonstrates the essential difference between metallic and insulating samples. The temperature dependent $\epsilon(\omega)$ for

sample A, Figure 20 (a), shows the crossover to negative values and the Drude dispersion in the far IR. This free carrier dispersion is present in $\epsilon(\omega)$ from 300 K down to $\sim$ 20 K. The presence of free carriers down to low T is consistent with the presence of high σ_{DC} down to millikelvin T. In contrast, the temperature dependent $\epsilon(\omega)$ for sample D is shown in Figure 20 (b). As the temperature is lowered to $\sim$ 10 K and σ_{DC} drops, $\epsilon(\omega)$ crosses from negative to positive in the far infrared. Therefore, the free carriers become localized at low temperature in PAN-CSA sample D. It is proposed that the localization at low T is due to the ineffectiveness of phonon assisted delocalization in the disordered regions at low T [36]. The localization of the free carriers in PAN-CSA sample D at low T is consistent with the strong decrease of σ_{DC} at low T. Therefore, the difference between sample A which remains metallic and sample D which becomes insulating at low T is the presence of percolated free carriers down to low temperatures. The values for the low T Ω_p and τ [only shown for those temperatures where Drude dispersion is evident in $\epsilon(\omega)$] determined from Drude fits to σ and ϵ [38] are shown in Table IV. The presence of free electrons at room temperature in insulating sample D indicates that percolation behavior can occur at high T even though at low T, the composite is not percolated. This is proposed to reflect the importance of phonon-induced delocalization on the electronic localization length (L_{loc}) in the disordered regions which electronically couple "crystalline" metallic regions in inhomogeneous conducting polymers [23,33,37,70].

Fig. 21 (a) shows a plot of $\epsilon(\omega)$ versus $1/\omega^2$ at different temperatures for sample A. The slope varies with temperature, indicating that Ω_p is temperature dependent. This is further evidence that the insulator-metal transition is due to a loss of free carrier density [$n(T)$]. Fig. 21 (b) shows directly that the free carrier plasma frequency Ω_p approximately scales with σ_{DC} at each temperature for metallic sample A. This behavior contrasts the case in conventional metals where the temperature dependence of σ_{DC} is determined solely by the temperature dependence of the scattering time. Assuming that $\sigma_{DC}(T) = \Omega_p^2 \tau / 4\pi$, the scattering time actually increases at low T, Table IV, as in conventional metals. Therefore, the temperature dependence of σ_{DC} in inhomogeneous metallic conducting polymers must

primarily be determined by $n(T)$. Within the Anderson model, lowering the temperature would result in depopulation of more extended states above the mobility edge and therefore a decrease in the scattering time. The contradiction of the Anderson model prediction and the trend in the data argue further agains the Anderson IMT. The increase in τ at low T may instead reflect the more robust percolation paths which remain at low T as the less robust ones "freeze out".

Figure 22 shows the dielectric function parallel and perpendicular to the stretch direction for HCl doped, stretched PAN obtained from polarized reflectance measurements [62]. There is a strong anisotropy evident in the electrical response. Parallel to the stretch direction, the high energy (~ 1 eV) zero crossing of $\epsilon(\omega)$ is observed as well as strong dispersion in the IR. Perpendicular to the stretch direction, $\epsilon(\omega)$ is positive over the whole energy range, showing very weak dispersion. The anisotropy present along the chain direction must be accounted for within the model of the insulator-metal transition. The homogeneous Anderson model which has been employed in the literature [85,105,109] assumes the material is isotropic. The fact that the anisotropic nature of the polymer transport is not included in the framework of the homogeneous Anderson IMT model also rules out this model for the conducting polymer IMT.

In summary, $\epsilon(\omega)$ is characteristic of strongly localized electrons ($\tau \sim 10^{-15}$ s) for samples E-G far from the IM transition. For samples A-D near the IM transition, a small fraction of the carriers become macroscopically delocalized ($\tau \geq \sim 10^{-13}$ s) while the majority of carriers are still strongly localized ($\tau \sim 10^{-15}$ s). The difference between metallic sample A and insulating sample D is that the free carriers freeze out in sample D at low T. This behavior is characteristic of percolating systems. Unlike usual percolating systems, the percolation for doped polymers can be temperature dependent. The dielectric response of oriented materials clearly point out the importance of dimensionality in the electronic behavior.

H. Discussion of Conductivity and Dielectric Functions

The dielectric function and optical conductivity provide insight into the nature of the disorder in the metallic state. In this section, $\epsilon(\omega)$ and $\sigma(\omega)$ for the PAN-CSA samples are compared with the localization modified Drude model for homogeneously disordered systems and a model for inhomogeneous disorder.

For the homogeneously disordered system, the mean free time is limited to a very short time due to substantial disorder. For materials near the insulator-metal transition, $k_F\lambda \sim 1$ [65,84,85,105]. Due to the limitation of λ, $\sigma(\omega)$ is suppressed and $\epsilon(\omega)$ is driven positive at low energy. The frequency dependence of σ and ϵ in this model is described by the localization modified Drude model [58,84,85,105], Section II B, with a short scattering time.

A typical fit of the localization modified Drude model is shown in Figure 23 for sample E. To assure that causality is satisfied, the parameters were chosen, Table V, to describe both $\sigma(\omega)$ and $\epsilon(\omega)$. The experimental $\sigma(\omega)$ and $\epsilon(\omega)$ are well represented for PAN-CSA sample E. It is important, however, to determine whether the parameters obtained are reasonable. The values obtained for the localized carrier scattering time τ_1 are comparable to the values obtained from the Drude fits to $\sigma(\omega)$, Table III, confirming the short scattering time ($\tau_1 \sim 10^{-15}$ s). However, the "full" carrier plasma frequency Ω_{p1} is small compared to what was found for the Drude fits, Table III, suggesting a sizeable difference in oscillator strength between the two models. Integration of $\sigma(\omega)$ for the localization modified Drude model shows that

$$8 \int_0^\infty \sigma_{LMDM}(\omega)d\omega = \Omega_{p1}^2[1 + C/(k_F v_F \tau_1)^2] \tag{21}$$

so that the oscillator strength is larger in the localization modified Drude model than just Ω_{p1}^2 as in the unmodified Drude model [34,69]. For sample F, the full plasma frequency calculated using Equation 21 and the parameters from Table V is ~ 2.0 eV, reconciling the oscillator strength differences between the Drude model and localization modified Drude model estimates of the oscillator strength.

36

The parameter $C/(k_F v_F)^2$ can be used to estimate the Fermi velocity (v_F), the mean free path ($= v_F \tau$), and the one-dimensional density of states ($N(E_F) = 2/\pi \hbar v_F$) [85]. To make the estimates, C is assumed to be of order unity [65,84,85,105]. Assuming that the sample is fully doped, k_F has the value of $\tau/2c$ with c $\sim$ 10.2 Å [54]. Using $\tau \sim 1.2 \times 10^{-15}$ and $C/(k_F v_F)^2 \sim 1.4 \times 10^{-30}$ s^2, $v_F \sim 5 \times 10^7$ cm/s and $\lambda = v_F \tau \sim 7$ Å. Using these parameters, $k_F \lambda \sim 1$. This value of $k_F \lambda$ is in accord with the Ioffe-Regel condition for conductors close to an insulator-metal transition since the mean free path is on the same size as a nitrogen and benzene ring repeat in PAN ($\sim$ 5.2 Å). The prediction for the one-dimensional density of states at the Fermi level, $N(E_F) \sim 2$ state per eV per formula unit (two nitrogens and two rings) is also in reasonably good agreement with the measured value of $N(E_F) \sim 1$ state per eV per formula unit [44]. The consistency of these estimates obtained from the localization modified Drude model indicate that the high frequency behavior of samples similar to E (dominated by localized excitations) is reasonably represented within a homogeneous Anderson transition picture.

The fits for $\sigma(\omega)$ and $\epsilon(\omega)$ of PAN-CSA samples E-G using the parameters in Table V are shown in Figures 24 and 25. For samples F and G, $\sigma(\omega)$ and $\epsilon(\omega)$ are complicated by the presence of localized polarons as well. Since the localized polaron feature occurs in a narrow frequency window ($\sim$ 1.5 eV), it can be modeled by including a lorentzian function. For sample F the lorentzian parameters were $\Omega_p = 0.8$ eV, $\gamma = 4.4 \times 10^{14}$ Hz, and $\omega_0 = 1.5$ eV, while $\Omega_p = 1.3$ eV, $\gamma = 5.4 \times 10^{14}$ Hz, and $\omega_0 = 1.5$ eV were used for PAN-CSA sample G.

One set of experimental trends is well represented by the localization modified Drude model. τ_1 increases with increasing σ_{DC}, suggesting that the disorder decreases, consistent with the shift of ω_{max} in $\sigma(\omega)$. Samples A-D deviate in an important way from the predictions of the localization modified Drude model in the far IR, Figures 26 and 27. Figure 26 shows that $\sigma(\omega)$ for PAN-CSA samples A-D can be reasonably modeled except for the upturn in $\sigma(\omega)$ for sample C at $\sim$ 0.02 eV. On the other hand, Figure 27 demonstrates that the localization modified Drude model can not account for the free carrier behavior in $\epsilon(\omega)$ at

low frequency. This is a consequence of the assumption within a homogeneous material that all of the carriers have short mean free times ($k_F v_F \tau_1 \sim 1$) limited by strong disorder. It is proposed that this model explains well the behavior of only the relatively strongly localized electrons ($k_F \lambda \sim 1$) in conducting polymers with reasonable parameters.

The early studied PAN-CSA [85] and PPy doped with perchlorate [112] both had $\sigma_{DC} \sim$ 100 S/cm, indicating that the carriers were reasonably localized. Therefore, the agreement of the optical properties with the localization modified Drude model (with $\tau \sim 10^{-15}$ s) is expected. However, this model is unable to account for the free electron behavior observed in higher σ_{DC} samples because Drude dispersion requires that $k_F \lambda \gg 1$.

The necessity of treating the highly conducting polymers within a composite picture with inhomogeneous disorder is clear from an estimate of the mean free paths for the percolated electrons. Using the same Fermi velocity estimated from the localization modified Drude model ($v_F \sim 5 \times 10^7$ cm/s) the mean free path for free electrons in PAN-CSA is estimated as $\lambda_{free} \sim 10^3$ Å. with $k_F \lambda_{free} \sim 10^2$ using τ determined from the infrared measurements. (As noted earlier, band narrowing due to disorder will increase m^* and decrease estimates of λ_{free}.) This estimate of λ_{free} is consistent with previous estimates of the mean free time in doped polyacetylene [64,108] and the inelastic length obtained from magnetoresistance experiments [90,113]. Since $\lambda_{free} \gg \xi$, the crystalline coherence length (~ 50 Å). these free electrons are capable of diffusing large distances among ordered regions between scattering events.

In contrast to the macroscopically homogeneous Anderson transition, effective medium models allow for macroscopic inhomogeneity and composite behavior. Therefore, there can be percolated metallic regions of the sample where the mean free time is large. For composite systems, the disorder is macroscopic and there may be two very different phases. Most calculations within the effective medium theory are for composites of an insulator and a metal [78,79]. For the conducting PAN and PPy samples, the different parts of the composite are proposed to be the more ordered (metallic) regions and the disordered regions where localization becomes important. The percolating behavior of conducting polymers

is expected to be modified from traditional insulator/metal composites as the ordered and disordered regions do not have sharp boundaries; a single polymer chain may be a part of both ordered and disordered regions. Also, phonon assisted transport occurs in the disordered regions. Nevertheless, there are many qualitative similarities with the insulator/metal composite. Figure 5 shows the behavior of $\sigma(\omega)$ for a system of metal particles percolating in an insulating matrix. At low volume fractions before percolation, the Drude peak in $\sigma(\omega)$ is suppressed and shows up as a localized plasmon excitation at higher energy [78,79]. The maximum in this localized plasmon band in $\sigma(\omega)$ shifts to lower frequency as the materials near percolation. Above percolation, the Drude peak is observed at low frequency, though the conductivity is only a fraction of the conductivity of the bulk metal (alternatively, the Drude peak contains only a fraction of the density of carriers). The fraction depends on the proximity of the system to the percolation threshold. Though it was not calculated in Ref. [78], the appearance of a Drude peak in $\epsilon(\omega)$ is required by causality when there is a Drude peak in $\sigma(\omega)$.

For insulating PAN-CSA samples E-G, $\epsilon(\omega)$ shows only localized excitations. The peak in $\sigma(\omega)$ shifts to lower frequency with increasing σ_{DC}, consistent with the behavior of a localized plasmon band in a composite system [78,79]. For metallic PAN-CSA samples A-D, $\epsilon(\omega)$ has a large plasma frequency, ω_{p1}, for electrons with localized behavior and a small plasma frequency for free electrons. The fraction of the free carriers that percolate was estimated as $\sim 10^{-2}$-10^{-3}. This value may seem small for percolation but the volume fraction required for percolation depends upon the aspect ratio of the percolating item [78,79]. Conducting polymers have already been shown to percolate in insulating polymers at volume filling fractions beneath 1 % [110,114]. The experimental $\sigma(\omega)$ for PAN-CSA sample C demonstrates an upturn at low energy ($\sim$0.02 eV) similar to the percolating Drude peak in Figure 5. Therefore, both the insulating and metallic samples are consistent with the expectations for a composite system.

The presence of two electron gases, one of which is strongly localized ($\tau \sim 10^{-15}$ s) and the other which has percolated showing Drude dispersion and a long mean free time ($\tau \sim$

10^{-13} s), qualitatively can be taken into account by introducing a distribution function for scattering times into the localization modified Drude model. This distribution function is strongly peaked with $k_F \lambda \sim 1$ but with a small tail with larger $k_F \lambda$. Such a distribution of scattering times assumes that there are some paths in the material which are more ordered so that τ is longer, taking into account the inhomogeneous nature of a polymer solid as determined from x-ray experiments [54,73]. For such a case, we assume for convenience that $\sigma_{inhomo}(\omega)$ and $\epsilon_{inhomo}(\omega)$ are given by:

$$\sigma_{inhomo}(\omega) = \int_0^\infty P(\tau)\sigma_{LMDM}(\omega, \tau)d\tau \tag{22}$$

$$\epsilon_{inhomo}(\omega) = \int_0^\infty P(\tau)\epsilon_{LMDM}(\omega, \tau)d\tau, \tag{23}$$

where $P(\tau)$ is the distribution function for the scattering times.

For analytical simplicity, we consider the representative distribution function

$$P(\tau) = \frac{2\Delta}{\pi} \frac{\tau^2}{(\tau^2 - \tau_0^2) + \tau^2 \Delta^2}. \tag{24}$$

where Δ describes the width of the spread in scattering times and τ_0 is the average scattering time. The resulting functions were fit to $\epsilon(\omega)$ and $\sigma(\omega)$ for sample C. The plots, shown in Fig. 28, indicate that by including a distribution which allows for carriers with long scattering times, both the localized ($\tau \sim 10^{-15}$s) and the Drude carriers ($\tau \sim 10^{-13}$ s) can be roughly fit. The parameters used were $\Omega_p = 1.0$ eV, $\tau_0 = 2.7 \times 10^{-15}$s, $C/(k_F v_F)^2 = 11 \times 10^{-30}$ s^2, and $\Delta = 1.3 \times 10^{-15}$s. The behavior of these model functions as the width of the distribution function is varied is shown in Figure 29, which shows the crossover in behavior from insulating (with only localized carriers) to metallic (with some delocalized electrons). An increase in the width of spread of scattering times (Δ) is equivalent to having more carriers with long mean free times. In other words, an increase in Δ places the sample further above percolation so that there are more ordered paths where free electron diffusion is possible.

Qualitatively, $\sigma(\omega)$ and $\epsilon(\omega)$ for PAN samples E-G show the behavior expected for *both* the good conductor/poor conductor composites as well as for the 3-D localization modified

Drude model with only short scattering times (corresponding to the Ioffe-Regel criterion). $\sigma(\omega)$ and $\epsilon(\omega)$ of highly conducting PAN-CSA samples A-D show Drude behavior for a small fraction of the conduction electrons which essentially percolate through the film while the remaining conduction electrons are more localized, showing the behavior expected only within the composite picture. Therefore, $\sigma(\omega)$ and $\epsilon(\omega)$ indicate that the metallic state in conducting PAN-CSA and $PPy(PF_6)$ is inhomogeneous. This same experimental behavior has been reported for iodine [63,64,107] and perchlorate [108] doped polyacetylene and is shown for doped PPy in Section V.

I. Microwave Dielectric Constant

The microwave frequency dielectric constant (ϵ_{MW}) is a key probe of the delocalization of charge carriers. For delocalized Drude electrons at frequencies less than their plasma frequency, the real part of the dielectric function [$\epsilon(\omega)$] is negative due to the inertia of the free electron in an AC field [34,69,82,111]. For a localized carrier, the charges can stay in phase with the field and $\epsilon(\omega)$ is positive at low frequencies. Thus, the sign of the microwave dielectric constant serves as a sensitive probe of the presence of free electrons and provides independent verification of the infrared results.

Figure 30 shows ϵ_{MW} for selected samples. For PAN-CSA samples E and F, ϵ_{MW} is positive from 300K down to $\sim$ 4K, indicating the importance of localization in these materials at all temperatures. This also agrees well with the infrared $\epsilon(\omega)$ for samples E and F which were positive in the far infrared, characteristic of localized carriers. For samples A, C, and D, ϵ_{MW} is negative at room temperature, providing an independent confirmation of the free electron behavior observed in the infrared. For sample A, ϵ_{MW} remains negative down to $\sim$ 4K, demonstrating independently of the infrared data that the metallic state in conducting polymers is accompanied by free (Drude) carriers. Also, the trends observed in $\sigma_{DC}(T)$ for samples A and C are observed in $\epsilon_{MW}(T)$. Near room temperature, ϵ_{MW} for sample C is metallic (negative), with an absolute value larger than that for sample A; however, at low T,

41

sample A shows a weaker dependence on temperature. The strong temperature dependence of ϵ_{MW} at low T for sample C indicates that ϵ_{MW} will cross over to positive values at lower T, reflecting low T insulating behavior. For PAN-CSA sample D, the crossover of ϵ_{MW} from negative to positive values is directly observed at low T (~ 10 K). This provides a confirmation of the crossover observed for sample D from metallic (negative values) to insulating (positive values) in the T dependent far IR $\epsilon(\omega)$ at ~ 150 K, and reflects the progressively increasing localization of the charge carriers as the temperature is lowered. This changeover from delocalized (free) carriers to localized carriers at low temperature reflects the importance of phonon-induced delocalization in the disordered regions of the inhomogeneous metallic state [36,71]. For sample D, the crossover in ϵ_{MW} occurs at ~ 10 K. For other samples, this crossover has been observed at high temperatures (~ 20 K) [36], indicating the importance of the specific material processing conditions and the resulting composite network.

Using the Drude model at low frequency ($\omega\tau \ll 1$)

$$\sigma \sim \omega_p^2 \tau / 4\pi \tag{25}$$

$$\epsilon \sim -\omega_p^2 \tau^2. \tag{26}$$

the plasma frequency (Ω_p) and scattering time (τ) can be estimated from ϵ_{MW} and σ_{MW} (not shown), Table VI. The predicted Ω_p for free electrons in samples A, C, and D is in the far infrared, in good agreement with the observed zero crossings of $\epsilon(\omega)$ in the far infrared. though the values are smaller than obtained from the Drude fits in the far infrared. The relative size of the plasma frequencies for the different samples [ω_p(sample C) $> \omega_p$(sample A) $> \omega_p$(sample D)] is in good agreement with the infrared measurements. The scattering time predicted in each case is $\sim 10^{-11}$ s. The values are two orders of magnitude larger than the τ predicted in section IV G.

The quantitative difference between the the Ω_p and τ estimated from infrared and microwave transport measurements may be a reflection of the inhomogeneity of the percolating network [70]. From the discussion of the optical conductivity and dielectric functions, a dis-

tribution of scattering times for the conduction electrons is likely involved in the transport. Therefore, at the lowest frequencies, the carriers which are the most delocalized (with the longest scattering times, $\tau \sim 10^{-11}$ s) may dominate the transport. Ω_p appears smaller because a smaller fraction of the charge carriers have such a long mean free time ($\tau \sim 10^{-11}$ s).

The trends observed in the infrared are confirmed by the transport measurements at 6.5 GHz. The high σ_{DC} oberved as $T \rightarrow 0$ in metallic PAN-CSA is accompanied by the presence of free electrons down to low temperature. In the samples where the free electron density "freezes out" at low temperature, σ_{DC} has a much stronger, insulating temperature dependence.

V. POLYPYRROLE

The dc and high frequency transport in polypyrrole (PPy) prepared with different dopants has also been systematically investigated. Introducing different dopants varies the disorder in the PPy system. For instance, PPy doped with hexafluorophosphate (PF_6) can be highly conducting down to mK temperature [35,49]. When the slightly larger dopant p-toluenesulfonate (TsO) is used, the conductivity is reported to be more strongly temperature dependent [22,23], showing three dimensional variable range hopping behavior. When doped not with an anion but with a polyanion (sulfated polyhydroxyether) the conductivity decreases drastically from ~ 10 S/cm at room temperature down to $\sim 10^{-10}$ S/cm at ~ 1.5 K [89], showing a stronger temperature dependence [$\sigma_{DC} \propto \exp(-(T_0/T)^{1/2})$].

The key difference between PPy doped with PF_6 and TsO is the disorder introduced into the polymer during polymerization. When, for instance, PF_6 was chemically exchanged with TsO as the dopant for PPy in a film polymerized with PF_6, the magnitude and temperature dependence of the conductivity of the resulting film was nearly identical to that of the parent film [PPy(PF_6)] [102]. The following set of experiments used the structural order of the doped PPy sample as a background to understand the difference between the metallic

state in these systems.

A. X-ray Diffraction

The x-ray diffractometer tracings for each of the films of this study are shown in Figure 31. X-ray studies of PPy(PF$_6$) indicate that these films are ≈ 50 % crystalline, with a structural coherence length of ~ 20 Å [54,115]. The reduction in structural disorder induced during synthesis compared with earlier studied PPy materials has been suggested to account for the improved metallic behavior of these new films [24,52,102]. The structure assigned to the crystalline portion of PPy(PF$_6$) samples consists of 2D stacks of PPy chains in the (b,c) plane separated by an intervening layer of PF$_6$ counterions [54,115]. The PPy(TsO) for this study was ~ 25 % crystalline, approximately one half that of PPy(PF$_6$), with a crystalline domain size which is decreased to ~ 15 Å [23] compared to ~ 20 Å. The bulky TsO dopant not only increases the separation between (b,c) layers of PPy chains by 50%, but likely enhances the conformational disorder of the PPy chain since intrachain x-ray reflections are not recorded for PPy(TsO). In contrast, the PPy(S-PHE) films show only a single broad peak reflecting disordered chains [53]. The fact that the maximum average d-spacing for the disordered chains in PPy(S-PHE) is different than those of PPy(PF$_6$) and PPy(TsO) may reflect the average stacking of the S-PHE polyanion which assume the majority of the volume in this material. The differences in crystallinity allows us to probe the effects of structural disorder on the metallic state.

B. Magnetic Susceptibility

The spin susceptibility was measured from room temperature down to 4 K for PPy doped with PF$_6$, TsO, and S-PHE. The temperature dependence provides insight into the nature of the spin states. A simple model for the total susceptibility is

$$\chi = \chi^{Pauli} + \chi^{Curie}, \tag{27}$$

44

where $\chi^{Pauli}(= 2\mu_B^2 N(E_F))$ is temperature independent and χ^{Curie} is proportional to T^{-1} [34]. Figure 32 shows $\chi \cdot T$ versus T for each of the samples. The solid lines are fits to $\chi \cdot T = \chi_P \cdot T + C$ where χ_P is the temperature independent Pauli susceptibility and C is the Curie constant.

The positive slopes in Fig. 32 indicate a finite $N(E_F)$ for each of the materials. $N(E_F) \simeq$ 0.80 states/eV·ring for PPy(PF$_6$): $N(E_F) \simeq 0.20$ states/eV·ring for PPy(TsO); and $N(E_F) \simeq 0.17$ states/eV·ring for PPy(S-PHE). This value is comparable to the N(E$_F$) measure for other highly conducting polymers [3]. For doped polyacetylene [33], N(E$_F$) ~ 0.18 states/eV·C and in PAN-CSA, N(E$_F$) ~ 0.1 states/eV·(C + N) [44]. The positive intercept corresponds to a finite number of uncorrelated Curie spins. PPy(TsO) [$C = 1.7 \times 10^{-3}$ emu·K/mol·ring ~ 1 spin/200 polypyrrole rings] and PPy(S-PHE) [$C = 6.3 \times 10^{-4}$ emu·K/mol·ring ~ 1 spin/500 polypyrrole rings] show a larger Curie component than PPy(PF$_6$) [$C = 3.6 \times 10^{-4}$ emu·K/mol·ring ~ 1 spin/10^3 polypyrrole rings]. The fact that PPy(TsO) has a larger number of Curie spins than PPy(S-PHE) per chain may reflect that bipolarons are preferentially formed in the more disordered chains of PPy(S-PHE).

The larger $N(E_F)$ and smaller density of uncorrelated spins for PPy(PF$_6$) correlates with the larger fraction of the sample having three-dimensional order [115], *i.e.*, crystallinity stabilizes a metallic density of states. Similar to doped polyaniline, where the metallic Pauli susceptibility is associated with the three-dimensionally ordered regions [39,40], a large finite $N(E_F)$ is present in PPy when there are large three dimensionally ordered (crystalline) regions. In more disordered materials, localized polarons or bipolarons predominate.

C. DC Conductivity

The reduced activation energy [66] (W $\equiv d\ln\sigma/d\ln T$) vs. T is shown in Fig. 33 for PPy(PF$_6$), PPy(TsO), and PPy(S-PHE). For PPy(PF$_6$), the positive slope of W with increasing T implies that it is in the metallic regime. Millikelvin dc conductivity measurements on the same PPy(PF$_6$) materials show metallic behavior [35] and a negative magnetoresis-

tance [49], confirming that PPy(PF$_6$) has crossed the IMT and is metallic at low T. In contrast, PPy(TsO) has a negative slope for its W plot, placing it in the localized regime. The slope of the line is ~ 0.25, indicating three dimensional variable range hopping. For PPy(S-PHE), the W plot also has a negative slope (~ 0.5) at low temperature, characteristic of quasi-1d variable range hopping. Therefore, with increased disorder and chain isolation, doped PPy becomes more insulating, with charge transport that becomes more characteristic of reduced dimensionality hopping, just as for the PAN-CSA samples.

The same reliance on structural order is seen for σ_{DC} in Fig. 34. σ_{DC} for PPy(PF$_6$) very slowly decreases as temperature decreases from room temperature ($\sigma_{dc} \sim 300$ S/cm) to ~ 20 K, and $d\sigma/dT < 0$ for $T < 20$ K. The increase in σ_{DC} with decreasing T at low temperature has been reported previously [22,24,35,101,102] and attributed to a tunneling mechanism [101]. The ratio of $\sigma(RT)/\sigma(20K)$ is <1.8, relatively small in comparison to that of other highly conducting polymers.

$\sigma_{DC}(T)$ for more disordered PPy(TsO) shows a stronger temperature dependence than PPy(PF$_6$) consistent with a 3d variable-range-hopping (VRH) model; $\sigma_{dc}(T) = \sigma_0 \exp[-(T_0/T)^{1/4}]$ where $T_0 = 16/k_B N(E_F)L^3$ (k_B: Boltzmann constant). Using the slope of $\ln \sigma$ vs $T^{-1/4}$, $T_0 \simeq 4100$ K and $N(E_F) = 0.2$ states/eV·ring determined from the magnetic studies, the localization length is estimated as $L \sim 30$ Å. This estimate of localization length is comparable with the x-ray crystalline coherence length (ξ).

For PPy(S-PHE), which has the least structural order of the doped PPy samples studied here, $\sigma_{DC}(T)$ shows the highest degree of localization, with a large resistivity ratio $[\rho(4K)/\rho(300K) \sim 10^{10}]$. The temperature dependence is that of quasi-one dimensional variable range hopping.

D. Reflectance

Similar to the results for highly conducting polyaniline, the reflectance of PPy doped with PF$_6$ and TsO, shown in Fig. 35, shows Drude-like behavior [69], increasing monotonically

with decreasing energy from the conduction electron plasma edge at ≈ 2.1 eV for PPy(PF$_6$) and ≈ 1.9 eV for PPy(TsO) and approaching unity at low energy [23]. The oscillations in the mid IR (~ 0.1 eV) are due to the phonons of doped PPy. The reflectance of the S-PHE doped PPy samples shows a more modest reflectance in the far IR, only approaching 40 % near 0.006 eV [53]. Unlike polyaniline, there is not a separate peak at higher energy (~ 1.5 eV) that develops with decreasing conductivity.

The reflectance for PPy(PF$_6$) measured at 10 K (2 meV- 1.2 eV) is compared with its room temperature reflectance in Fig. 36. There is very little change at high frequencies ($>$ 0.1 eV). In the far IR, the 10 K reflectance is higher than the room temperature reflectance down to ~ 0.01 eV and then drops beneath the room temperature reflectance. The decrease of the reflectance measured in the far IR is consistent with the drop in σ_{DC} as T decreases. The region where the 10 K reflectance rises above the room temperature reflectance is due to free carriers which are localized at low temperature, similar to what has been reported in polyacetylene [107] and earlier in this chapter for polyaniline. This decrease of the reflectance in the far IR is inconsistent with the opening of an intrinsic gap in the electronic spectrum of PPy(PF$_6$) as reported earlier [109].

E. Absorption Coefficient

The absorption coefficients (α) for PPy doped with PF$_6$, TsO, and S-PHE obtained via Kramers-Kronig analysis of the refelectance data are shown in Figure 37. α for each of the samples is similar in character at low energy. There is a peak at $\sim$1.0 eV and 2.8 eV. The absorption at higher energy depends upon the counter-ion which was used. Aside of the presence of a peak at 1.5 eV (attributed to isolated polarons [50]), the absorption coefficients for PAN-CSA [55,56], and PPy doped with PF$_6$, TsO, and S-PHE are very similar, implying that highly conducting PPy forms a polaron lattice like doped PAN instead of a bipolaron lattice [116]. In contrast, a peak at ~ 1.5 eV was observed in lightly doped poorly conducting PPy [112].

The absorption coefficient for PPy(PF$_6$) at 10 K is compared with the room temperature α in Figure 38. There is very little change in the absorption coefficient at high energy as the temperature is lowered. In the far IR, a peak at $\sim$ 0.01 eV forms due to absorption by carriers which are delocalized at room temperature but localized at 10 K. This behavior is very similar to what has been reported for iodine doped polyacetylene with decreasing temperature [107]. The lack of change of the absorption at high energy indicates that the localized electrons do not contribute significantly to the high σ_{DC}; the temperature dependence of their conductivity contribution is different than the highly conducting carriers at DC.

F. Optical Conductivity

Similar to the results for polyaniline, $\sigma(\omega)$ for doped PPy, Fig. 39, does not show Drude-like conductivity at low energies. Instead, $\sigma(\omega)$ shows Drude dispersion at high energy ($\sim$ 0.4-2 eV), a maximum at ω_{max}, and then suppression at low energy. The lack of structural order in PPy(S-PHE) results in a much greater suppression in $\sigma(\omega)$. The ratio $\sigma(6meV)/\sigma(\omega_{max})$ gives an indication of the localization. For PPy(PF$_6$), this ratio is $\sim$ 0.9, for PPy(TsO), $\sim$ 0.3, and for the PPy doped with S-PHE, $\sim$ 0.05. The fact that $\omega_{max} \sim$ 0.3 eV for PPy(PF$_6$) is smaller than $\omega_{max} \sim$ 0.4 eV for PPy(TsO) is consistent with the increased disorder in PPy(TsO), resulting in a smaller mean free path. The values obtained from a Drude fit to the high energy region of each sample are given in Table VII.

The plasma frequency for conduction electrons is higher in PPy doped with PF$_6$, TsO, and S-PHE than in PAN-CSA. For PPy(PF$_6$), a three pyrrole ring repeat plus dopant has dimensions: a = 13.4 Å, b = 10.95 Å, and c = 3.4 Å [115]. For PPy(TsO), the unit cell dimensions are the same except that a = 18.0 Å [23] as the toluenesulfonate dopant is larger. In heavily doped PPy(PF$_6$) and PPy(TsO), there is one dopant added per three rings [22–24,35]; therefore the doping density for PPy(PF$_6$) is $n \sim 2 \times 10^{21}$ cm^{-3} and for PPy(TsO), $n \sim 1.5 \times 10^{21}$ cm^{-3}. For PPy(S-PHE), the carrier density can be approxi-

mated from the density (1.3 g/cm^3) [89] as $n \sim 2.9 \times 10^{20}$ cm^{-3}. From these conduction electron densities and the Ω_{p1} ($= \sqrt{4\pi n e^2/m^\star}$) determined from Drude fits, $m^\star \sim 0.5\ m_e$ for PPy(PF$_6$), $m^\star \sim 0.5\ m_e$ for PPy(TsO), and $m^\star \sim 0.2\ m_e$ for PPy(S-PHE). Therefore, the effective masses ($m^\star$) for doped PPy are lower than for PAN-CSA, implying that the overlap integrals are larger.

The scattering times determined from Drude fits (from 1.4-$\sim$2.4 eV) for the conduction electrons are small, $\tau_1 \sim 10^{-15}$ s. This small value is comparable though smaller than what was found for τ_1 in PAN-CSA. The smaller values of τ for PPy compared with PAN may reflect greater disorder present in the disordered regions of PPy compared with PAN [54]. With increasing structural order within the PPy samples, τ increases, implying a larger mean free path for carriers in PPy(PF$_6$) in agreement with the behavior of ω_{max}.

G. Optical Dielectric Function

The same percolation behavior seen in $\epsilon(\omega)$ for doped polyaniline also is observed for doped polypyrrole. For metallic PPy(PF$_6$), $\epsilon(\omega)$ shows three zero crossings, Figure 40 (a). The dispersion of the localized electrons at high energy (> 0.06 eV) and the Drude dispersion in the far infrared are both evident. For PPy(TsO), the scattering time is reduced sufficiently by disorder that ϵ does not cross zero in the entire experimental frequency range. For PPy(S-PHE), the dispersion is very weak throughout the optical frequency range. The plot of $\epsilon(\omega)$ versus $1/\omega^2$ for PPy(PF$_6$) is shown in Fig. 40 (b). The slope of the curve gives $\Omega_p \sim 0.17$ eV. Compared to the plasma frequency of the full conduction electron gas (~ 2.5 eV), only a small fraction of the conduction electrons are "free". Estimating in the same manner as for PAN-CSA (Equation 17),

$$n_{free} \sim (0.17/2.5)^2 \sim 5 \times 10^{-3}. \qquad (28)$$

As discussed for PAN-CSA, the estimate of the fraction of delocalized electrons is dependent upon the ratio of m* in the disordered regions to m* in the ordered regions. Due to the

49

linearity of $\epsilon(\omega)$ versus $1/\omega^2$ down to 20 cm^{-1}, $\tau >\sim 1/20$ cm$^{-1} \sim 3 \times 10^{-13}$ s. Similar to the metallic state in PAN-CSA, there is a large majority of conduction electrons which are localized ($\tau_1 \sim 10^{-15}$ s) and a small fraction of the conduction electrons which are delocalized ($\tau >\sim 10^{-13}$ s) in metallic PPy(PF$_6$). With this long τ, a mean free path comparable to that of delocalized carriers in PAN-CSA is estimated. For more disordered PPy(TsO) and PPy(S-PHE), the electrical response is determined by only localized electrons. Similar to the behavior of $\epsilon(\omega)$ in PAN-CSA, $\epsilon(\omega)$ is larger in the far IR for more ordered, higher conductivity PPy(TsO) than PPy(S-PHE).

For PPy(PF$_6$), $\epsilon(\omega)$ at room temperature is compared with $\epsilon(\omega)$ at ~ 10 K in Fig. 41. Two important points are observed. At high energy, there is very little change in the dispersion of the localized carriers. $\epsilon(\omega)$ remains negative to slightly lower frequency, indicating that the scattering time changes only slightly as the temperature is lowered. This lack of a strong dependence of the scattering time on thermal processes indicates that the (static) disorder is the predominant scattering mechanism for the charge carriers. Similar results were reported for PAN doped with CSA [85]. The slight increase of the scattering time for localized electrons while σ_{DC} decreases implies that there is not a direct correlation of the localized carriers and the DC transport.

The temperature dependence of $\epsilon(\omega)$ in the far IR is shown in Fig. 41 (b). In contrast to the weak temperature dependence at high energy, the Drude dispersion is more strongly affected. Down to 10 K, the dielectric function remains negative in the far IR, indicating that free carriers are present down to low T in PPy(PF$_6$), consistent with the high millikelvin σ_{DC} measured for this material [35] and also with the behavior of metallic PAN-CSA. At 10 K, the plasma frequency for free electrons Ω_p is 0.1 eV, decreased from 0.17 eV at room temperature. In comparison to σ_{DC}, which decreases by ~ 1.8. ω_p decreases by ~ 1.7. The scaling of Ω_p with σ_{DC} indicates that free carriers dominate the high DC conductivity for doped PPy as well as for doped PAN. The free carriers which are frozen out at low temperature give rise to the additional absorption at ~ 10 meV seen in the absorption coefficient, Figure 37. As for PAN-CSA, the presence of a negative far IR $\epsilon(\omega)$ at room

temperature excludes the possibility of an intrinsic many body gap [109].

H. Microwave Transport

Microwave measurements for PPy samples provide independent confirmation of the results reported at infrared frequencies. Figure 42 compares $\sigma_{DC}(T)$ with $\sigma_{MW}(T)$ for PPy(PF$_6$) [23], PPy(TsO) [23], and PPy(S-PHE) [53]. The absolute values and the temperature dependence of σ in the DC and microwave frequency ranges for PPy(PF$_6$) are nearly identical, in agreement with the Drude theory. The stronger temperature dependence of σ_{DC} for PPy(TsO) and PPy(S-PHE) in comparison with $\sigma_{MW}(T)$ is expected since the sample is in the localized regime [117].

Figure 43 shows $\epsilon_{MW}(T)$ for PPy(PF$_6$) [23]. ϵ_{MW} at 265 K is huge and negative, $\sim -10^5$, corresponding to the Drude dielectric response at microwave frequencies. ϵ_{MW} remains huge and negative down to 4.2 K ($\sim -4 \times 10^4$). The absolute value of ϵ_{MW} has a very weak T-dependence and a maximum at ~ 20 K. This behavior qualitatively agrees with $\sigma_{DC}(T)$ and $\sigma_{MW}(T)$. Using the Drude model in the low frequency limit ($\omega\tau \ll 1$), $\sigma_{MW} \simeq (\omega_p^2/4\pi)\tau$ and $\epsilon_{MW} \simeq -\omega_p^2\tau^2$. Hence, ω_p and $\tau(\simeq 4\pi\epsilon_{MW}/\sigma_{MW})$ are ~ 0.007 eV and $\sim 3 \times 10^{-11}$ sec, respectively. The prediction of a small plasma frequency of free electrons with a zero crossing in the far infrared agrees well with the infrared measurements, providing an independent confirmation of the Drude carriers. Again, as for PAN-CSA, the plasma frequency (scattering time) for free carriers is small (large) compared with the infrared estimates. Therefore, a distribution of scattering times is important for highly conducting PPy samples as well.

Though its room temperature σ_{MW} is one-third that of PPy(PF$_6$), ϵ_{MW} for more disordered PPy(TsO) is positive in the entire temperature range [23]. The $T \to 0$ localization length can be estimated as ~ 25 Å using the metallic box model [59] and the ESR $N(E_F)$ in agreement with the crystalline coherence length ($\xi \sim 15$ Å). ϵ_{mw} linearly increases as temperature increases even though the localization length is small, which implies that the charge can easily delocalize through the disordered regions, and the phase segregation between the

metallic and disordered regions is weak in the PPy(TsO) sample.

ϵ_{MW} for PPy(S-PHE) is also positive over the entire temperature range and smaller in absolute value than ϵ_{MW} for PPy(TsO), consistent with stronger localization of charges in the PPy(S-PHE) sample [53]. For PPy(S-PHE), ϵ_{MW} does not change much from its low temperature saturation value until the temperature increases above $\sim$ 150 K, at which point it grows rapidly at higher temperatures. This indicates that there may be an energy barrier to hopping below 150 K. Using the metallic box model for this sample and the ESR $N(E_F)$, the $T \rightarrow 0$ localization length is estimated as $\sim$ 7 Å comparable to two pyrrole rings and smaller than that of PPy(TsO), consistent again with greater localization.

VI. POLYACETYLENE

It is noted that similar behavior for highly conducting doped polyacetylene samples have been reported, including a finite $N(E_F)$ [3,12,33,41,43], σ_{DC} finite as $T \rightarrow 0$ [35], large and negative ϵ_{MW} [3,33,118], and a rapid increase in the negative value of ϵ in the far infrared [63,64,108]. Further, samples for which $\sigma_{DC} \rightarrow 0$ as $T \rightarrow 0$ generally have ϵ_{MW} positive with the magnitude related to sample conductivity [119], and a positive $\epsilon(\omega)$ in the infrared [64,108]. Transport in the poorly conducting regime for doped polyacetylene has been thoroughly reviewed [6]. Models very similar to those applied to doped polyaniline and polypyrrole can be applied to doped polyacetylene [3,33]

VII. DISCUSSIONS AND CONCLUSIONS

The experimental data for doped polyaniline, polypyrrole, and polyacetylene show a wide range of electrical behavior, varying from localized charge carrier hopping behavior for all charge carriers to Drude free carrier diffusion for a small fraction of the carriers while the remaining carriers are localized. Regardless of the family of conducting polymer, the metallic state possesses certain universal properties, including a finite density of states at the Fermi level, a high σ_{DC} as $T \rightarrow 0$, and a dielectric function that becomes negative in

the infrared and remains negative to the microwave frequency range, as expected for Drude carriers. Conducting polymers exist which range from insulating to metallic and span the insulator-metal transition at low temperature.

Through analyses of the high frequency dielectric and conductivity functions, new insights have been obtained concerning the metallic state in conducting polymers. For highly conducting doped PAN and doped PPy, with decreasing energy, there are two negative going zero crossings for the optical frequency dielectric function for metallic conducting polymers. The dielectric frequency response for highly conducting doped polyacetylene is very similar, with a high energy zero crossing at $\sim$ 3 eV, and a very rapid increase in the absolute value of the dielectric function in the far IR. These two electrical responses correspond to the plasma response of delocalized (Drude) carriers at low frequencies (far IR $\sim$ 0.05 eV) and localized carriers at high frequencies ($\sim$ 1-3 eV). The delocalized carriers have an unusally long scattering time $\tau \sim 10^{-13}$ s, which is attributed to the intrinsic anisotropy of the Fermi surface for quasi-one-dimensional conducting polymers and that most off-chain impurities are effectively screened. However, the fraction of the charge carrier density which is delocalized is estimated to be less than 1 %. Analysis of the temperature dependence of the DC conductivity and dielectric function indicate that σ_{DC} is high at low T when $\epsilon(\omega)$ has free carrier behavior at low T. For materials for which the free carrier behavior in $\epsilon(\omega)$ "freezes out" at low T, σ_{DC} decreases rapidly at low T. This suggests that the high σ_{DC} in metallic conducting polymers is controlled by only the small fraction of delocalized carriers. This indicates that large potential increases in σ_{DC} (up to $\sim 10^5$ S/cm) can be obtained if the whole charge carrier density had $\tau \sim 10^{-13}$ s.

The zero crossing (ω_{p1}) at higher energy (1-3 eV) is attributed to the majority of carriers which are localized with short mean free times ($\tau \sim 10^{-15}$ s). For conducting polymers whose dielectric response is dominated by only localized carriers, $\epsilon(\omega)$ is positive in the far IR and σ_{DC} has a strong temperature dependence, becoming insulating at low T.

The insulator-metal transition was shown explicitly to be controlled by disorder in PPy through structural studies and in PAN by varying the local chain conformation by casting

PAN-CSA from different solvents. Though the IMT is controlled by disorder, it is not a homogeneous 3D Anderson transition. This is asserted because (1) PAN-CSA samples with conductivity (σ_{DC}) higher than the minimum metallic conductivity (σ_{min}) become insulating at low temperature; (2) the evolution of $\sigma_{DC}(T)$ through the IMT is not monotonic; (3) millikelvin σ_{DC} for selected insulating samples is not consistent with hopping transport; (4) the density of free electrons present in a sample scales with $\sigma_{DC}(T)$ so that a sample which demonstrates metallic behavior at low temperature may have a smaller density of free electrons at room temperature than a sample which demonstrates insulating behavior at low temperature due to the non monotonic evolution of $\sigma_{DC}(T)$ through the IMT; (5) $\epsilon(\omega)$ and $\sigma(\omega)$ for metallic samples are consistent with macroscopically inhomogeneous models but not Anderson localization models; (6) a long scattering time ($\tau \geq \sim 10^{-13}$ s) inconsistent with the Ioffe-Regel condition for homogeneous 3D Anderson localization of carriers close to the IMT is determined; and (7) doped oriented films of polyaniline and polyacetylene demonstrate a known strong anisotropy along the chain direction, implying a strong influence of dimensionality on the entire class of polymers which is not accounted for in the Anderson IMT model. Therefore, it is suggested that the metallic state and IMT are not controlled by homogeneous disorder.

Instead, the metallic state and IMT are proposed to be controlled by inhomogeneous disorder, consistent with the percolation (composite) behavior evident in $\epsilon(\omega)$ and $\sigma(\omega)$ at high frequencies, x-ray diffraction results, and the growth of a Pauli component of the magnetic susceptibility with increasing crystallinity. The composite nature results from the distinct transport among ordered metallic regions and the surrounding disordered regions where localization is strong. The IMT occurs when L_{loc} in the disordered regions exceeds the distance between ordered metallic regions so that carriers effectively percolate among metalic islands through the ordered paths. A small number of percolated paths could account for the small fraction of delocalized carriers. For metallic samples, a long mean free path up to $\sim 10^3$ Å (or perhaps longer if the microwave τ is used to estimate λ) is estimated (assuming m^* in the ordered and disordered regions is the same), much larger than the crystalline

domain sizes ($\sim 10^1$ Å). Such a long mean free path is consistent with percolation among many ordered regions.

For systems where the carriers have not percolated among the ordered regions, the transport is controlled by hopping and phonon-induced delocalization in the intermittant disordered regions. It is suggested that for materials with more rod-like chain conformation in the disordered regions, free carriers are present at room temperature which may "freeze out" at low T, causing a temperature dependent IMT. For systems with more coil-like local order in the disordered regions, free carriers are not observed and transport is due to hopping among localized states, which contributes less than ~ 10 S/cm to σ_{DC}.

REFERENCES

[1] see e.g. *Handbook of the Physical Properties of Polymers*, edited by J. E. Mark, (AIP Press, Woodbury, 1996).

[2] C. K. Chiang, C. R. Fincher, Jr., Y. W. Park, A. J. Heeger, H. Shirakawa, E. J. Louis, S. C. Gau, and A. G. MacDiarmid, Phys. Rev. Lett. **39**, 1098 (1977).

[3] R. S. Kohlman, J. Joo, and A. J. Epstein,*Conducting Polymers: Electrical Conductivity*, Chapter 34 in Handbook of the Physical Properties of Polymers, edited by J. E. Mark, (AIP Press, Woodbury, 1996).

[4] see e.g. *Handbook of Conducting Polymers*, edited by T. A. Skotheim (Marcel Dekker, New York, 1986).

[5] For recent research activity see for example, Proc. Int. Conf. on Science and Technology of Synthetic Metals, ICSM '96, Snowbird, Utah, July 28- Aug. 2, 1996, in Synth, Met., in press, ICSM '94, Seoul, Korea, July 21-29, 1994, in Synth. Met. **69-71** (1995); ICSM '92, Goteborg, Sweden, Aug. 12-18, 1992, in Synth. Met. **55-57** (1993); ICSM '90, Tubingen, FRG, Sept. 2-9, 1990, in Synth. Met. **41-43** (1991); and ICSM '88, Santa Fe, NM, June 26- July 2, 1988, in Synth. Met. **27-29** (1988).

[6] A. J. Epstein, *AC Conductivity of Polyacetylene: Distinguishing Mechanisms of Charge Transport*, Handbook of Conducting Polymers, edited by T. A. Skotheim (Marcel Dekker, New York, 1986), p.1041.

[7] A. J. Heeger, S. A. Kivelson, J. R. Schrieffer, and W. P. Su, Rev. Mod. Phys. **60**, 781 (1988).

[8] D. Baeriswyl, D. K. Campbell, and S. Mazumdar, in **Conjugated Conducting Polymers**, edited by H. G. Keiss (Berlin. Springer-Verlag, 1992), p. 7.

[9] E. M. Conwell, IEEE Transactions on Electrical Insulation, **EI-22**, 591 (1987).

[10] R. E. Peierls, *Quantum Theory of Solid* (Clarendon, Oxford, 1955), p. 108.

[11] J. Tsukamoto, Adv. in Phys. **41**, 509 (1992); J. Tsukamoto, A. Takahashi, and K. Kawasaki, Japan, J. Appl. Phys. **29**, 125 (1990).

[12] H. Naarmann and N. Theophilou, Synth. Met. **22**, 1 (1987).

[13] H. Shirakawa, Y. -X. Zhang, T. Okuda, K. Sakamaki, and K. Akagi, Synth. Met. **65**, 93 (1994).

[14] J. -C. Chiang and A. G. MacDiarmid, Synth. Met. **13**, 193 (1986).

[15] A. J. Epstein, H. Rommelmann, R. Bigelow, H. W. Gibson, D. M. Hoffman, and D. B. Tanner, Phys. Rev. Lett. **50**, 1866 (1983).

[16] P. N. Adams, P. Laughlin, A. P. Monkman, and N. Bernhoeft, Solid State Commun. **91**, 895 (1994); the value of conductivity reported in Fig. 4 is for samples kindly provided by Monkman and coworkers, and measured at The Ohio State University.

[17] Y. Cao, P. Smith, and A. J. Heeger, Synth. Met. **48**, 91 (1992).

[18] J. Joo, Z. Oblakowski, G. Du, J. P. Pouget, E. J. Oh, J. M. Weisinger, Y. Min, A. G. MacDiarmid, and A. J. Epstein, Phys. Rev. B **69**, 2977 (1994).

[19] Y. Z. Wang, J. Joo, C. -H. Hsu, J. P. Pouget, and A. J. Epstein, Phys. Rev. B **50**, 16,811 (1994).

[20] Z. H. Wang, H. H. S. Javadi, A. Ray, A. G. MacDiarmid, A. J. Epstein, Phys. Rev. B **42**, 5411 (1990).

[21] J. Yue, Z. H. Wang, K. R. Cromack, A. J. Epstein, and A. G. MacDiarmid, J. Am. Chem. Soc. **113**, 2655 (1991).

[22] M. Yamaura, T. Hagiwara, and K. Iwata, Synth. Met. **26**, 209 (1988).

[23] R. S. Kohlman, J. Joo, Y. Z. Wang, J. P. Pouget, H. Kaneko, T. Ishiguro, and A. J.

Epstein, Phys. Rev. Lett. **74**, 773 (1995).

[24] K. Sato, M. Yamaura, T. Hagiwara, K. Murata, and M. Tokumoto, Synth. Met. **40**, 35 (1991).

[25] A. J. Epstein, H. Rommelmann, M. Abkowitz, and H. W. Gibson, Phys. Rev. Lett. **47**, 1549 (1981).

[26] A. J. Epstein, H. Rommelmann, and H. W. Gibson, Phys. Rev. B **31**, 2502 (1985).

[27] F. Zuo, M. Angelopoulos, A. G. MacDiarmid, and A. J. Epstein, Phys. Rev. B **39**, 3570 (1989).

[28] J. C. Scott, P. Pfluger, M. T. Krounbi, and G. B. Street, Phys. Rev. B **28**, 2140 (1983).

[29] T. Ito, H. Shirakawa, and S. Ikeda, J. Polm. Sci. Polym. Chem. Ed. **12**, 11 (1974).

[30] K. Ito, Y. Tanabe, K. Akagi, and H. Shirakawa, Phys. Rev. B **45**, 1246 (1992).

[31] J. H. Edwards and W. J. Feast, Polymer Commun. **21**, 595 (1980).

[32] J. C. W. Chien, *Polyacetylene: Chemistry, Physics, and Material Science* (Academic, New York 1984), p. 24.

[33] A. J. Epstein, J. Joo, R. S. Kohlman, G. Du, A. G. MacDiarmid, E. J. Oh, Y. Min, J. Tsukamoto, H. Kaneko, J. P. Pouget, Synth. Met. **65**, 149 (1994).

[34] C. Kittel, *Introduction to Solid State Physics* (John Wiley & Sons, Inc., New York, 1986), p. 157.

[35] T. Ishiguro, H. Kaneko, Y. Nogami, H. Nishiyama, J. Tsukamoto, A. Takahashi, M. Yamaura, amd J. Sato, Phys. Rev. Lett. **69**, 660 (1992), H. Kaneko, T. Ishiguro, J. Tsukamoto, and A. Takahashi, Solid State Commun. **90**, 83 (1994).

[36] J. Joo, V. N. Prigodin, Y. G. Min, A. G. MacDiarmid, and A. J. Epstein, Phys. Rev. B **50**, 12,226 (1994).

[37] R. S. Kohlman, J. Joo, Y. G. Min, A. G. MacDiarmid, and A. J. Epstein, Phys. Rev. Lett. **77**, 2766 (1996).

[38] R. S. Kohlman, A. Zibold, D. B. Tanner, G. G. Ihas, Y. G. Min, A. G. MacDiarmid, and A. J. Epstein, submitted.

[39] J. M. Ginder, A. F. Richter, A. G. MacDiarmid, and A. J. Epstein, Solid State Commun. **63**, 97 (1987).

[40] M.E. Jozefowicz, R. Laversanne, H.H.S. Javadi, A.J. Epstein, J.P. Pouget, X. Tang, and A.G. MacDiarmid, Phys. Rev. B **39**, 12958 (1989).

[41] A. J. Epstein, H. Rommelmann, M. A. Druy, A. J. Heeger, and A. G. MacDiarmid, Solid State Commun. **38**, 683 (1981).

[42] P. K. Kahol, H. Guan, and B. J. McCormick, Phys. Rev. B **44**, 10393 (1991).

[43] S. Ikehata, J. Kaufer, T. Woerner, A. Pron, M. A. Druy, A. Sivak, A. J. Heeger, and A. G. MacDiarmid, Phys. Rev. Lett. **45**, 1123 (1980).

[44] N. S. Saricifti, A. J. Heeger, and Y. Cao, Phys. Rev. B **49**, 5988 (1994).

[45] K. Mizoguchi, M. Nechtschein, J. -P. Travers, and C. Menardo, Phys. Rev. Lett. **63**, 66 (1989); M. Nechtschein, F. Genoud, C. Menardo, K. Mizoguchi, J. -P. Travers, and B. Villeret, Synth. Met. **29**, E211 (1989).

[46] (a) Y. W. Park, Synth. Met. **45**, 173 (1991);(b) Y. W. Park, A. J. Heeger, M. A. Druy, and A. G. MacDiarmid, J. Chem. Phys. **73**, 946 (1980).

[47] H. H. S. Javadi, A. Chakraborty, C. Li, N. Theophilou, D. B. Swanson, A. G. MacDiarmid, and A. J. Epstein, Phys. Rev. B **43**, 2183 (1991).

[48] C. K. Subramaniam, A. B. Kaiser, P. W. Gilberd, C. J. Liu, and B. Wessling, Solid State Commun. **93**, 235 (1996).

[49] J. C. Clark, G. G. Ihas, A. J. Rafanello, M. W. Meisel, Reghu M., C. O. Yoon, Y. Cao, and A. J. Heeger, Synth. Met. **69**, 215 (1995).

[50] A. G. MacDiarmid and A. J. Epstein. Synth. Met. **65**, 103 (1994).

[51] M. Reghu, C. O. Yoon, D. Moses, A. J. Heeger, and Y. Cao, Phys. Rev. B **48**, 17685 (1993); M. Reghu, Y. Cao, D. Moses, and A. J. Heeger, *ibid.* **47**, 1758 (1993).

[52] J. H. Kim, J. H. Kim, H. K. Sung, H. J. Kim, C. O. Yoon, and H. Lee, Synth. Met., in press.

[53] R. S. Kohlman, S. M. Long, K. Bates, W. P. Lee, H. Kaneko, L. Zuppiroli, and A. J. Epstein. submitted.

[54] J. P. Pouget. Z. Oblakowski. Y. Nogami. P.A. Albouy, M. Laridjani, E.J. Oh. Y. Min. A.G. MacDiarmid. J. Tsukamuto, T. Ishiguro, and A.J. Epstein. Synth. Met. **65**, 131 (1994).

[55] A. G. MacDiarmid and A. J. Epstein. Synth. Met. **65**, 103 (1994).

[56] A.G. MacDiarmid, J.M. Weisinger, and A.J. Epstein. Bull. Am. Phys. Soc. **38**, 311 (1993); A.G. MacDiarmid and A.J. Epstein, Trans. 2nd Congresso Brazileiro de Polimeros, São Paulo, Brazil, Oct. 5-8, 1993. p. 544; Y. Min. A.G. MacDiarmid, and A.J. Epstein, Polymer Preprints **35**, 231 (1994).

[57] P. W. Anderson, Phys. Rev. **109**, 1492 (1958).

[58] N. ᴵ. Mott and E. Davis, *Electronic Processes in Non-Crystalline Materials* (Clarendon Press, Oxford. 1979), p. 6.

[59] Z. H. Wang, C. Li, E. M. Scherr, A. G. MacDiarmid. and A. J. Epstein, Phys. Rev. Lett. **66**, 1749 (1991): Z. H. Wang, E. M. Scherr, A. G. MacDiarmid, and A. J. Epstein, Phys. Rev. B **45**, 4190 (1992).

[60] M. I. Salkola and S. A. Kivelson. Phys. Rev. B **50**, 13,962 (1994); S. A. Kivelson and

M. I. Salkola, Synth. Met. **44**, 281 (1991).

[61] V. N. Prigodin and K. B. Efetov, Phys. Rev. Lett. **70**, 2932 (1993).

[62] R. P. McCall, E. M. Scherr, A. G. MacDiarmid, and A. J. Epstein, Phys. Rev. B **50**, 5094 (1994).

[63] G. Leising, Phys. Rev. B **38**, 10313 (1988).

[64] J. Tanaka, C. Tanaka, T. Miyamae, M. Shimizu, S. Hasegawa, K. Kamiya, and K. Seki, Synth. Met. **65**, 173 (1994).

[65] P. Lee and T. V. Ramakrishnan, Rev. Mod. Phys. **57**, 287 (1985); H. Fukuyama, in *Electron-Electron Interactions in Disordered Systems*, ed. by A. L. Efros and M. Pollak (Elsevier Science Publishers, 1985), p. 155.

[66] A. G. Zabrodskii and K. N. Zeninova, Zh. Eksp. Teor. Fiz. **86**, 727 (1984) [Sov. Phys. JETP **59**, 425 (1984)].

[67] V. N. Prigodin, private communication.

[68] A. F. Ioffe and A. R. Regel, Prog. Semicond. **4**, 237 (1960).

[69] F. Wooten, *Optical Properties of Solids* (Academic, New York, 1972), p. 173.

[70] R. S. Kohlman, D. B. Tanner, G. G. Ihas, Y. G. Min, A. G. MacDiarmid, and A. J. Epstein, Synth. Met., in press.

[71] J. Joo, Ph. D. Thesis: *Charge Localization and Delocalization Phenomena in Conducting Polymers*, The Ohio State University (1994); J. P. Pouget, to be published.

[72] F. Zuo, M. Angelopoulos, A. G. MacDiarmid, and A. J. Epstein, Phys. Rev. B **36**, 3475 (1987).

[73] J. P. Pouget, M.E. Jozefowicz, A.J. Epstein, X. Tang, and A.G. MacDiarmid, Macromolecules **24**, 779 (1991).

[74] J. P. Pouget, C.-H. Hsu, A. G. MacDiarmid, and A. J. Epstein, Synth. Met. **69**, 119 (1995).

[75] Z. H. Wang, A. Ray, A.G. MacDiarmid. and A.J. Epstein, Phys. Rev. B **43**, 4373 (1991).

[76] S. Kivelson and A. J. Heeger, Synth. Met. **22**, 371 (1988).

[77] V. N. Prigodin and K. B. Efetov, Synth. Met. **65**, 195 (1994).

[78] D. J. Bergman and D. Stroud, in *Solid State Physics*, edited by H. Ehrenreich and D. Turnbull (Academic, New York, 1992), vol. 46, p. 148.

[79] G. L. Carr, S. Perkowitz, and D. B. Tanner, *Far-Infrared Properties of Inhomogeneous Materials*, in Infrared and Millimeter Waves **13** (Academic, New York, 1985), p. 171.

[80] A. L. Efros and B. I. Shklovski, J. Phys. C **8**, L49 (1975); B. I. Shklovski and A. L. Efros, *Electronic Properties of Doped Semiconductors*,(Springer-Verlag, Heidelberg, 1984).

[81] A. I. Larkin and D. E. Khmelnitskii, Zh. Eskp. Teor. Fiz. **83**, 1140 (1982) [Sov. Phys. JETP **56**, 647 (1982)].

[82] P. Drüde, Ann. Phys. **1**, 566 (1900); **3**, 369 (1900).

[83] N. F. Mott, *Metal-Insulator Transitions*, (Taylor and Francis, New York, 1990).

[84] N. F. Mott and M. Kaveh, Adv. in Phys. **34**, 329 (1985).

[85] K. Lee, A. J. Heeger, and Y. Cao, Phys. Rev. B **48**, 14884 (1993).

[86] N. F. Mott, in *Localization and Interaction in Disordered Metals and Doped Semiconductors*, edited by D. M. Finlayson, Proceedings of the Thirty-First Scottish Universities Summer School in Physics of 1986 (Scottish Universities Summer School in Physics, 1986).

[87] N. F. Mott, in *Localization 1990*, edited by K. A. Benedict and J. T. Chalker, (Inst. of Phys. Conf. Ser. No. 108, Institute of Physics, Bristol, Philadelphia, New York, 1990). Paper presented at the Localization 1990 Conference held at the Imperial College, London.

[88] Y. G. Min, Ph.D. Thesis: *Determination of Factors Promoting Increased Conductivity in Polyaniline*, University of Pennsylvania (1995).

[89] O. Chauvet, S. Paschen, L. Forro, L. Zuppiroli, P. Bujard, K. Kai, and W. Wernet, Synth. Met. **63**, 115 (1994).

[90] Reghu Menon, C. O. Yoon, D. Moses, and A. J. Heeger, *Metal-Insulator Transition in Doped Conducting Polymers*, Handbook of Conducting Polymers, edited by R. Elsenbaumer.

[91] W. Fosong, T. Jinsong, W. Lixiang, Z. Hongfang, M. Zhishen, Mol. Cryst. Liq. Cryst. **160**, 175 (1988).

[92] Y. B. Moon, Y. Cao, P. Smith, and A. J. Heeger, Polym. Commun. **30**, 196 (1989).

[93] M.E. Jozefowicz. A.J. Epstein, J.P. Pouget, J.G. Masters. A. Ray and A.G. MacDiarmid, Macromolecules **25**, 5863 (1991).

[94] C. D. G. Minto and A. S. Vaughan, Polymer, in press.

[95] M. Laridjani, J.P. Pouget, E.M. Scherr, A.G. MacDiarmid, M.E. Jozefowicz, and A.J. Epstein, Macromolecules **25**, 4106 (1992).

[96] M. Laridjani, J. P. Pouget, A. G. MacDiarmid, and A. J. Epstein, to be published.

[97] L. Abell, S. J. Pomfret, E. R. Holland, P. N. Adams, and A. P. Monkman, Proc. Soc. of Plastic Engineers Ann. Technical Conf. (ANTEC 1996), 1417 (1996).

[98] Y. Cao and A. J. Heeger, Synth. Met. **52**, 193 (1992).

[99] H. H. S. Javadi, R. Laversanne, A. J. Epstein, R. K. Kohli, E. M. Scherr, and A. G. MacDiarmid, Synth. Met. **29**, E439, (1989).

[100] P. K. Kahol, A. J. Dyakonov, and B. J. McCormick, to be published.

[101] Reghu M. and S. V. Subramanyam, Sol. Stat. Commun. **72**, 325 (1989).

[102] M. Yamaura, K. Sato, T. Hagiwara, and K. Iwata, Synth. Met. **48**, 337 (1992).

[103] B. Movaghar and S. Roth, Synth. Met. **63**, 163 (1994).

[104] H. Ehrenreich and H.R. Phillip, Phys. Rev. **128**, 1622 (1962).

[105] K. Lee, A. J. Heeger, and Y. Cao, Synth. Met. **72**, 25 (1995).

[106] S. Stafstrom, J. L. Brédas, A. J. Epstein, H. S. Woo, D. B. Tanner, W. S. Huang, and A. G. MacDiarmid, Phys. Rev. Lett. **59**, 1464 (1987).

[107] H. S. Woo, D. B. Tanner, N. Theophilou, and A. G. MacDiarmid, Synth. Met. **41-43**, 159 (1991).

[108] T. Miyamae, M. Shimizu, and J. Tanaka, Bull. Chem. Soc. Jpn. **67**, 40253 (1994).

[109] K. Lee, Reghu M., E. L. Yuh, N. S. Saricifti, and A. J. Heeger, Synth. Met. **68**, 287 (1995).

[110] C. O. Yoon, M. Reghu, D. Moses, A. J. Heeger, and Y. Cao, Synth. Met. **63**, 47 (1994).

[111] G. Burns, *Solid State Physics* (Academic, New York, 1985), p. 187.

[112] K. Yakushi, L. J. Lauchlan, T. C. Clarke, and G. B. Street, J. Chem. Phys. **79**, 4774 (1983).

[113] M. Reghu, K. Vakiparta, C. O. Yoon, Y. Cao, D. Moses, and A. J. Heeger, Synth. Met. **65**, 167 (1994).

[114] G. Du, V. Prigodin, J. Avlyanov, A. G. MacDiarmid, and A. J. Epstein, to be pub-

lished.

[115] Y. Nagomi, J.P. Pouget, and T. Ishiguro, Synth. Met. **62**, 257 (1994).

[116] J. L. Brédas, J. C. Scott, K. Yakushi, and G. B. Street, Phys. Rev. B **30**, 1023 (1984).

[117] A. R. Long, Adv. Phys. **31**, 553 (1982); E. P. Nakhmedov, V. N. Prigodin, and A. V. Samukhin, Sov. Phys. Solid State **31**, 368 (1989).

[118] J. Joo, G. Du, V. N. Prigodin, J. Tsukamoto, and A. J. Epstein, Phys. Rev. B **52**, 8060 (1995).

[119] J. Joo, G. Du, J. Tsukamoto, and A. J. Epstein, Synth. Met., in press.

TABLES

TABLE I. The preparation conditions for the PAN samples of this study. Notice that in the column describing the solvent used, when the solvent listed is a percentage of m-cresol, the balance of the solvent is chloroform. Also, samples F and G appear to have been exposed to m-cresol

Sample	EB $\bar{M}_W$	Mixed as	Solvent	Wt %	σ_{DC}(300K) (S/cm)
A	400,000	powder	m-cresol	2	240
B	300,000	powder	m-cresol	2	110
C	50,000	solution	m-cresol	6.8	400
D	400,000	solution	m-cresol	1	120
E	50,000	powder	30% m-cresol	1	70
F	50,000	powder	chloroform	1	20
G	50,000	powder	chloroform	1	0.2

TABLE II. Comparison of the DC transport properties and the far IR reflectance at room temperature for PAN-CSA. The resistivity ratio $\rho_R = \rho(4.2K)/\rho(300K)$. The parameter γ is the hopping exponent determined from the low temperature W plot. T_M is the temperature at which the maximum occurs in σ_{DC}.

Sample	$\sigma_{DC}(300K)$ (S/cm)	ρ_R	γ	T_M (K)	Reflectance(6 meV)
A	230	1.7	0.08	188	0.8484
B	110	2.9	-0.2	218	0.7991
C	400	4.5	-0.3	224	0.9262
D	120	11	-0.6	240	0.8431
E	70	130	-0.5	288	0.7537
F	20	1.3×10^6	-0.7	>300	0.6915
G	0.7	-	-0.6	>300	0.3133

TABLE III. Comparison of the dc and high frequency conductivity parameters for selected PAN-CSA samples. The values for Ω_{p1} and τ_1 are obtained by fitting the Drude model to the optical conductivity near the plasma edge. ω_{max} represents the frequency where $\sigma(\omega)$ shows a maximum (ignoring phonon features).

Sample	$\sigma_{DC}(300K)$ (S/cm)	Ω_p (eV)	τ $(10^{-15}$ s)	ω_{max} (eV)
A	240	1.7	1.1	0.09
B	110	1.7	0.9	0.3
C	400	1.6	1.3	0.06
D	120	1.5	1.0	0.14
E	70	2.0	0.7	0.33
F	20	1.8	0.6	0.37
G	0.7	1.3	0.4	0.7

TABLE IV. Free electron plasma frequency Ω_p and scattering time τ versus temperature for selected PAN-CSA samples. The estimated fraction of the conduction electrons which are free and the estimated scattering time are also shown.

Sample	T (K)	$\sigma_{DC}(300K)$ (S/cm)	Ω_p (eV)	n_{free}/n_{cond} (10^{-3})	τ $(10^{-13}$ s)
A	300	230	0.07	1.2	2.3
	200	250	0.08	1.6	2.0
	100	240	0.06	0.9	2.9
	20	170	0.05	0.6	3.4
C	300	400	0.11	3.0	1.6
D	300	120	0.04	0.4	3.7
	200	120	0.03	0.2	6.6

TABLE V. Fit parameters for PAN-CSA using the localization modified Drude model. An additional lorentzian oscillator was included for samples F and G to model the 1.5 eV localized polaron peak.

Sample	Ω_{p1} (eV)	τ_1 (10^{-15} s)	$C/(k_F v_F)^2$ (10^{-30} s^2)	ϵ_{inf}
A	1.2	2.0	3.1	2.8
B	1.3	1.4	1.6	2.6
C	1.3	2.4	1.6	3.6
D	1.2	1.6	1.4	2.8
E	1.4	1.2	1.4	2.5
F	1.2	1.0	1.1	2.2
G	0.9	0.7	0.6	1.8

TABLE VI. Room temperature free electron plasma frequency ω_p and scattering time τ for selected PAN-CSA samples calculated from ϵ_{MW} and σ_{MW} using the Drude model.

Sample	ω_p (eV)	τ (10^{-11} s)
A (300K)	0.007	2.5
C (300K)	0.016	1.1
D (300K)	0.004	2.9

TABLE VII. Parameters from Drude fit to high energy (0.4-2 eV) $\sigma(\omega)$ for PPy samples.

Sample	Ω_{p1} (eV)	τ_1 (10^{-15} s)
PPy(PF$_6$)	2.5	0.53
PPy(TsO)	2.5	0.51
PPy(S-PHE)	1.5	0.43

FIGURES

FIG. 1. Chemical structures of conducting polyacetylene, polyaniline, and polypyrrole.

FIG. 2. Overview of conductivity of conducting polymers at room temperature. (a) stretched $[CH(I_3)]_x$ (from Ref. [11]), (b) stretched $[CH(I_3)]_x$ (from Ref. [12]), (c) $[CH(I_3)]_x$ (from Ref. [13]), (d) $[CH(I_3)]_x$ (from Ref. [14]), (d') $[CH(I_3)]_x$ (from ref. [15]), (e) stretched PAN-HCl (from Ref. [16]), (f) PAN-CSA from m-cresol (from Ref. [17]), (g) PAN-CSA from m-cresol (from Ref. [18]), (h) PAN derivative: poly(o-toluidine) POT-CSA fiber from m-cresol (from Ref. [19]), (i) POT-HCl (from Ref. [20]), (j) sulfonated PAN (from Ref. [21]), (k) stretched PPy(PF_6) (from Ref. [22]), (l) PPy(PF_6) and (l') PPy(TsO) (from Ref. [23,24]), (m) undoped trans-$(CH)_x$ (from Ref. [25]), (n) undoped cis-$(CH)_x$ (from Ref. [26]), (o) undoped PAN (EB) (from Ref. [27]), (p) undoped PPy (from Ref. [28]), The conductivity reported for the undoped polymers should be considered an upper limit due to the possibility of impurities.

FIG. 3. (a) Schematic picture of the inhomogeneously disordered state of metallic and insulating conducting polymers.(b) Schematic picture of rod-like and coil-like morphology of disordered regions.

FIG. 4. (a) Schematic picture of the temperature dependence of the various scattering times in the inhomogeneous disorder model and the respective localization domains, and (b) the corresponding diffusion constant ($\sigma_{DC}(T)$) expected for the inhomogeneous quasi-1D system (from [77].

FIG. 5. Schematic $\sigma(\omega)$ for an insulator/metal composite made up of a volume fraction f of a Drude metal and $1 - f$ of an insulator, as calculated in the effective medium theory. The heavy line at $\omega = 0$ represents the Drude peak. The integrated stength of the delta function is proportional to the height of the delta function. The scattering time is chosen to be very long so that the width of the Drude peak is too narrow to be resolved in the plot, emphasizing the behavior of the localized modes (from Ref. [78]).

FIG. 6. (a) The Anderson transition and (b) the form of the localized wavefunction in an Anderson metal-insulator transition. (c) The Fermi-glass state where the fermi level lies in the region of localized states (from Ref. [71]).

FIG. 7. Temperature dependent resitivity in an Anderson transition. Experimental temperature dependent resistivity for p-type germanium with different levels of compensation (K) leading to a variation in the electron density (from Ref. [58]). Notice that the magnitude and temperature dependence changes monotonically with increasing compensation (decreasing carrier density).

FIG. 8. Behavior of the localization modified Drude model with increasing mean free time (mean free path). (a) $\sigma(\omega)$. (b) $\epsilon(\omega)$. The parameters used were $\Omega_p^2 = 2$ eV^2 and $C/(k_F v_F)^2 = 1.9 \times 10^{-30}$ s^2.

FIG. 9. Chemical structure for sulfonated polyhydroxyethers (from Ref. [89]).

FIG. 10. (a) The reduced activation energy $W = d\ln(\sigma(T))/d\ln T$ for selected PAN-CSA samples.

FIG. 11. Temperature dependent dc conductivity for selected PAN-CSA samples.

FIG. 12. Millikelvin σ_{DC} for selected PAN-CSA samples. The high temperature (4-300 K) σ_{DC} data for each sample is included for comparison.

FIG. 13. Dependence of the millikelvin transport of selected PAN-CSA samples on applied 5 Tesla magnetic field.

FIG. 14. Room temperature reflectance for (a) PAN-CSA samples E-G and (b) PAN-CSA samples A-D.

FIG. 15. Temperature dependence of the far infrared (10-100 cm^{-1}) reflectance for (a) PAN-CSA sample A and (b) PAN-CSA sample D.

FIG. 16. Room temperature optical conductivity $\sigma(\omega)$ for (a) PAN-CSA samples E-G and (b) PAN-CSA samples A-D. The shift of the maximum in $\sigma(\omega)$ indicates the growth of the electron mean free path. The arrows indicate the peak (maximum) in the intraband $\sigma(\omega)$.

FIG. 17. Temperature dependence of the far IR optical conductivity in (a) PAN-CSA sample A and (b) PAN-CSA sample D.

FIG. 18. The real part of the dielectric response $\epsilon(\omega)$ at room temperature for (a) PAN-CSA samples E-G and (b) PAN-CSA samples A-D.

FIG. 19. $\epsilon(\omega)$ plotted versus $1/\omega^2$ for selected PAN-CSA samples at room temperature. The linearity confirms that the low energy carriers are free (Drude) carriers.

FIG. 20. Comparison of the temperature dependence of the dielectric response $\epsilon(\omega)$ for (a) metallic PAN-CSA sample A and (b) insulating PAN-CSA sample D.

FIG. 21. Temperature dependence of the free carrier dielectric response for metallic PAN-CSA sample A. (a) Far infrared $\epsilon(\omega)$ plotted against $1/\omega^2$ as a function of temperature. (b) Comparison of the temperature dependence of the free electron plasma frequency Ω_p and σ_{DC}.

FIG. 22. Real part of the dielectric constant vs. energy for light polarized (a) parallel and (b) perpendicular to the stretch direction for PAN doped with HCl (from Ref. [62]).

FIG. 23. Typical comparison of the localization modified Drude model fits to the experimental data. The data shown is (a) $\sigma(\omega)$ and (b) $\epsilon(\omega)$ for PAN-CSA sample E.

FIG. 24. (a) Experimental $\sigma(\omega)$ compared with (b) localization modified Drude model fits to $\sigma(\omega)$ for PAN-CSA samples E-G.

FIG. 25. (a) experimental $\epsilon(\omega)$ compared with (b) localization modified Drude model fits to $\epsilon(\omega)$ for PAN-CSA samples E-G.

FIG. 26. (a) experimental $\sigma(\omega)$ compared with (b) localization modified Drude model fits to $\sigma(\omega)$ for PAN-CSA samples A-D.

FIG. 27. (a) Experimental $\epsilon(\omega)$ compared with (b) localization modified Drude model fits to $\epsilon(\omega)$ for PAN-CSA samples A-D.

FIG. 28. Typical fit of the localization modified Drude model with a distribution of scattering times to the experimental data for PAN-CSA sample C. The plot shows (a) $\sigma(\omega)$ and (b) $\epsilon(\omega)$.

FIG. 29. Behavior of the localization modified Drude model with a spread in scattering times as the width of the distribution changes. Results for (a) $\sigma(\omega)$ and (b) $\epsilon(\omega)$ are shown. The parameters other than Δ are for PAN-CSA sample E, Table V.

FIG. 30. Temperature dependent microwave (6.5 GHz) dielectric constant for selected PAN-CSA samples. ϵ_{MW} for sample C was reported in Ref. [18].

FIG. 31. X-ray diffractometer tracings for PPy doped with PF_6 (from Ref. [115]) and S-PHE (from Ref. [53]), showing the change in crystallinity of the PPy as the dopant is varied.

FIG. 32. $\chi \cdot T$ vs. T for PPy(PF_6), PPy(TsO), and PPy(S-PHE).

FIG. 33. W plot for PPy doped with PF_6, TsO, and S-PHE.

FIG. 34. σ_{DC} for PPy doped with PF_6, TsO, and S-PHE.

FIG. 35. Room temperature reflection spectra for PPy doped with PF_6, TsO, and S-PHE.

FIG. 36. Comparison of the reflectance of PPy(PF_6) at room temperature an 10 K. Note the weak T dependence at high energy and the strong T dependence in the far IR.

FIG. 37. Room temperature absoption coefficient for PPy doped with PF_6, TsO, and S-PHE.

FIG. 38. Comparison of the absorption coefficient of $PPy(PF_6)$ at room temperature and 10 K (a) for the full optical range and (b) in the far IR.

FIG. 39. Room temperature optical conductivity for PPy doped with PF_6, TsO, and S-PHE. $\sigma(\omega)$ for disordered PPy(S-PHE) is suppressed strongly in the far IR.

FIG. 40. (a) Comparison of the real part of the dielectric function $\epsilon(\omega)$ for PPy doped with PF_6, TsO and S-PHE. (b) Far infrared $\epsilon(\omega)$ for $PPy(PF_6)$.

FIG. 41. Comparison of the dielectric response of $PPy(PF_6)$ at room temperature and 10 K. (a) $\epsilon(\omega)$ in the range of localized carriers. (b) $\epsilon(\omega)$ vs. $1/\omega^2$ in the far infrared.

FIG. 42. Comparison of the dc and microwave conductivity for (a) $PPy(PF_6)$, (b) PPy(TsO), and (c) PPy(S-PHE).

FIG. 43. (a) Microwave (6.5 GHz) dielectric constant for metallic $PPy(PF_6)$ and insulating PPy(TsO) and PPy(S-PHE).(b) Low T dielectric functions for PPy(TsO) and PPy(S-PHE) showing their saturation.

trans-polyacetylene   *cis*-polyacetylene
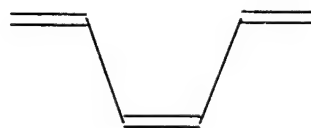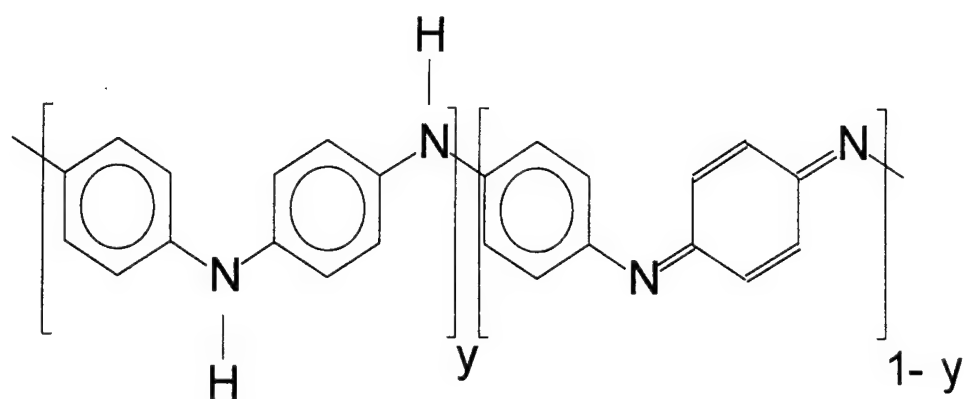
polyaniline: leucoemeraldine (y=1),
emeraldine(y=0.5) and pernigraniline (y=0)
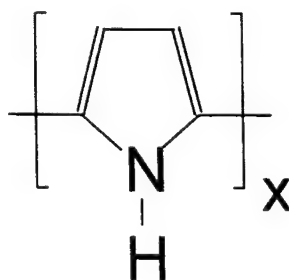
polypyrrole

Figure 1

Figure 2

(a)

$|\overset{s}{\leftrightarrow}|$

Ordered Regions

(b)

rod-like   coil-like

Figure 3

(a)

$\tau_{ph}(0,T)$

$\tau_{ph}(2k_F,T)$

$\tau_{imp}(2k_F)$

$\tau_{imp}(0)$

I-a | I-b

Localization

II-a | II-b

Coherent

0 | T_0' | T_S | T_c | T

(b)

$\dfrac{D_1(T)}{D_0}$

| Variable Range Hopping | Hopping Over Nearest States | Region of Localization Correlat ons | Band Transport |

1

ω_0 | T_c | T_b | T
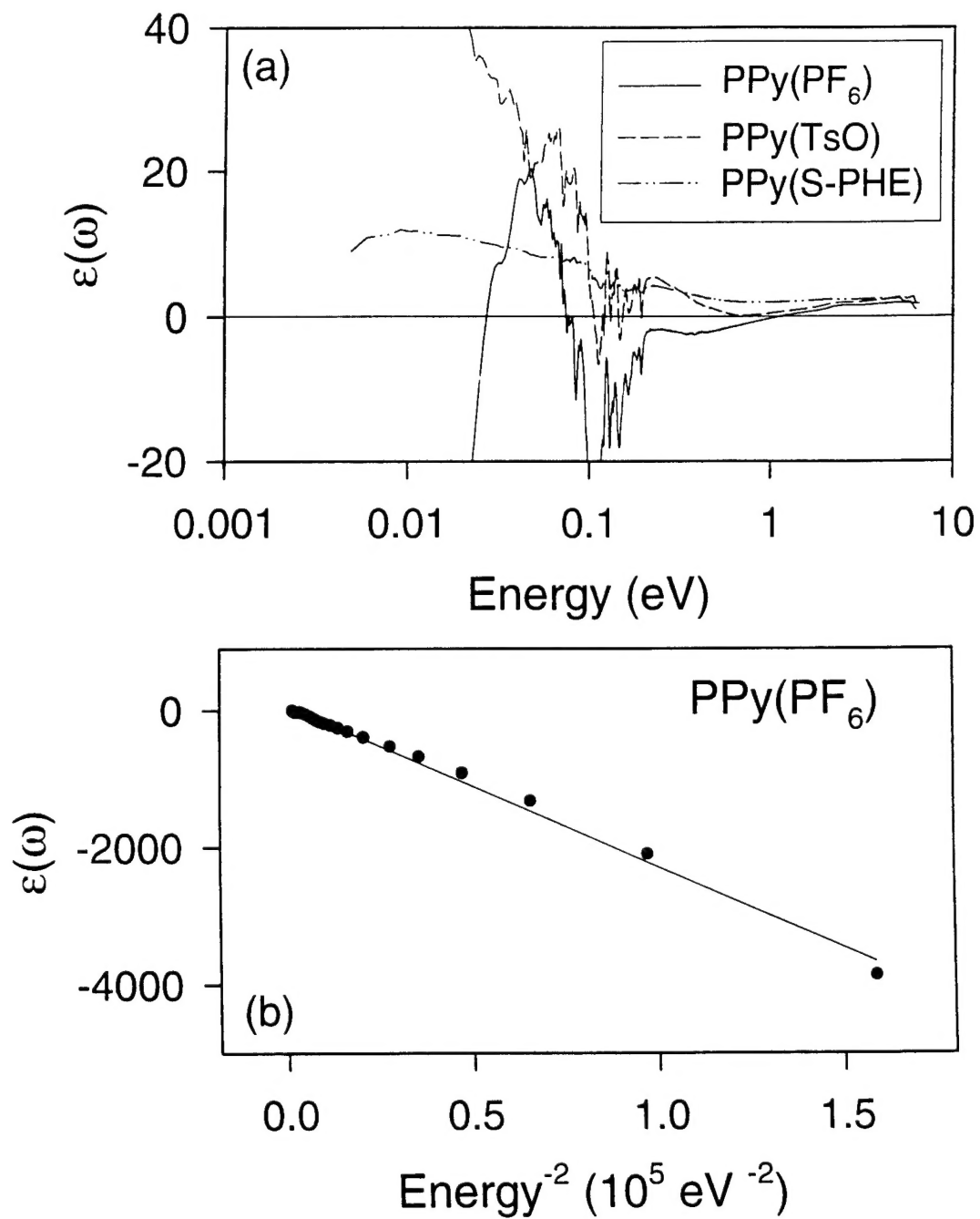
Figure 4

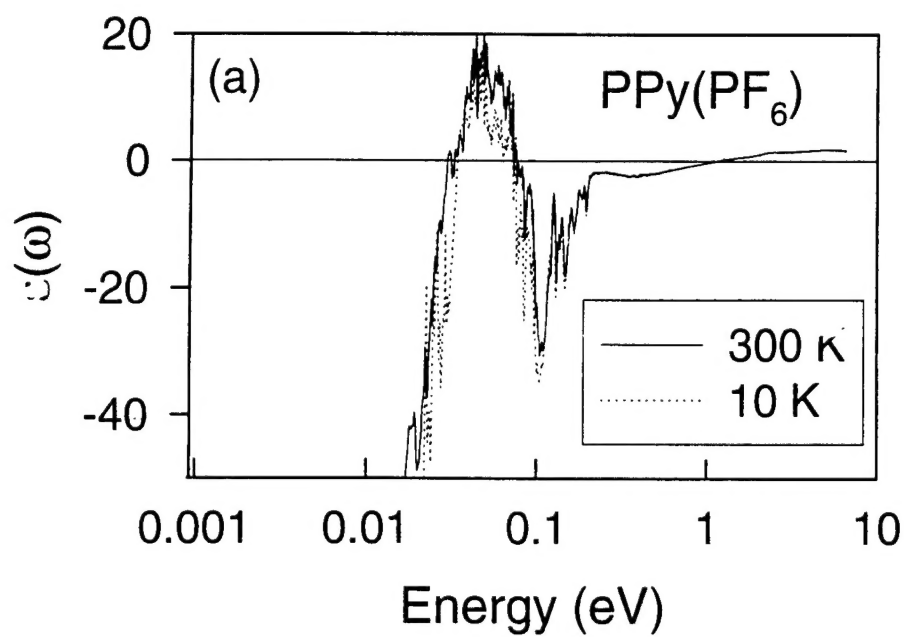Figure 5

(a)

(b)

$e^{-R/L}$

(c)
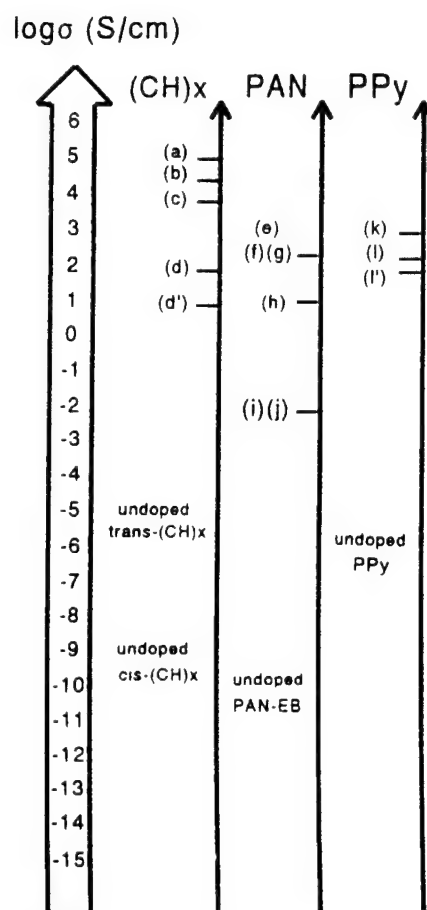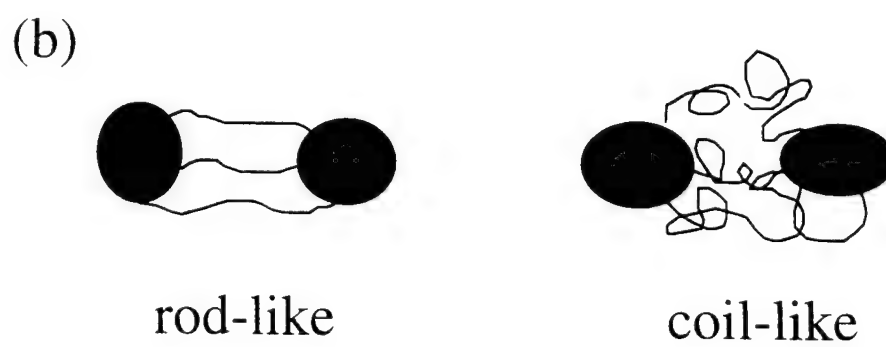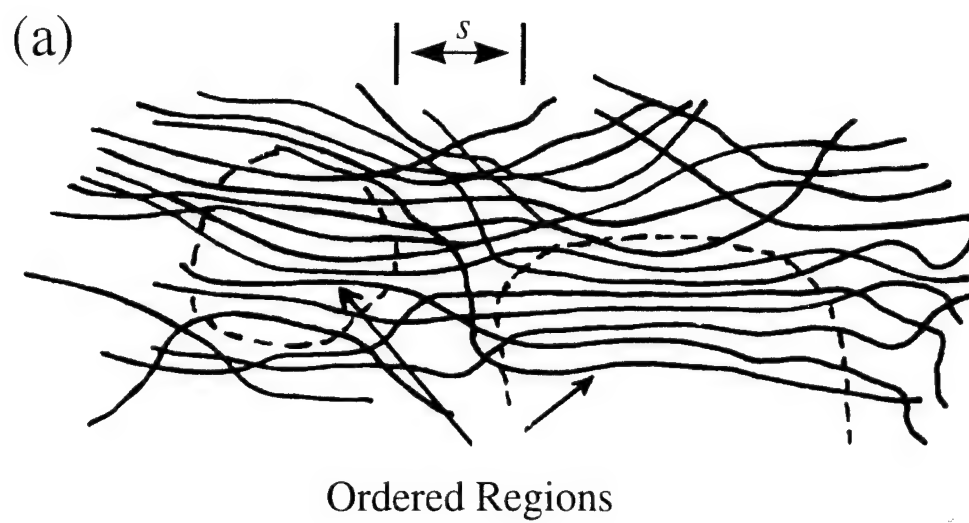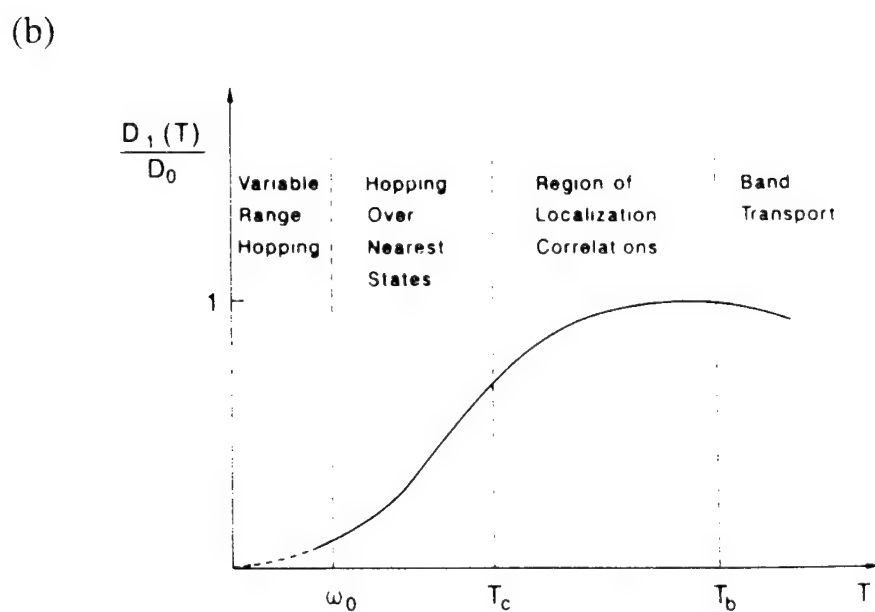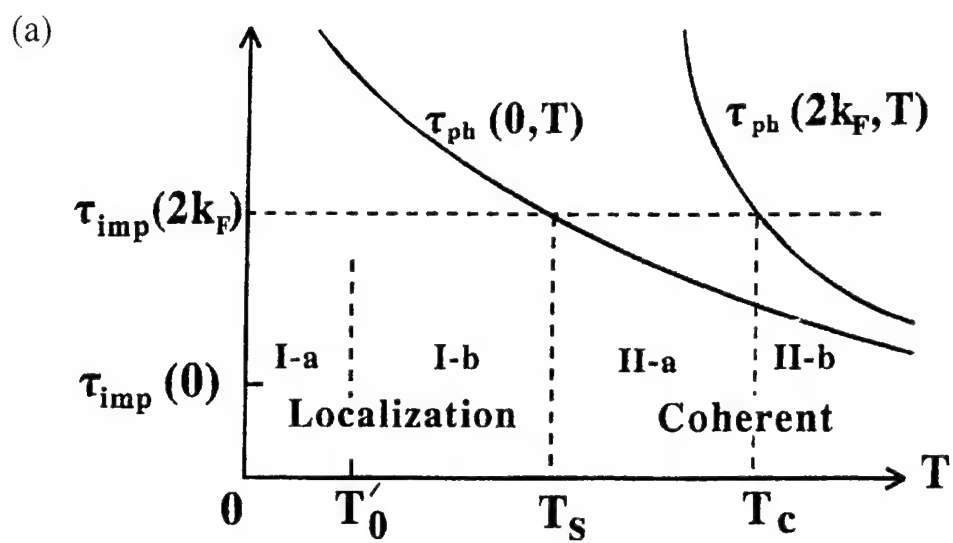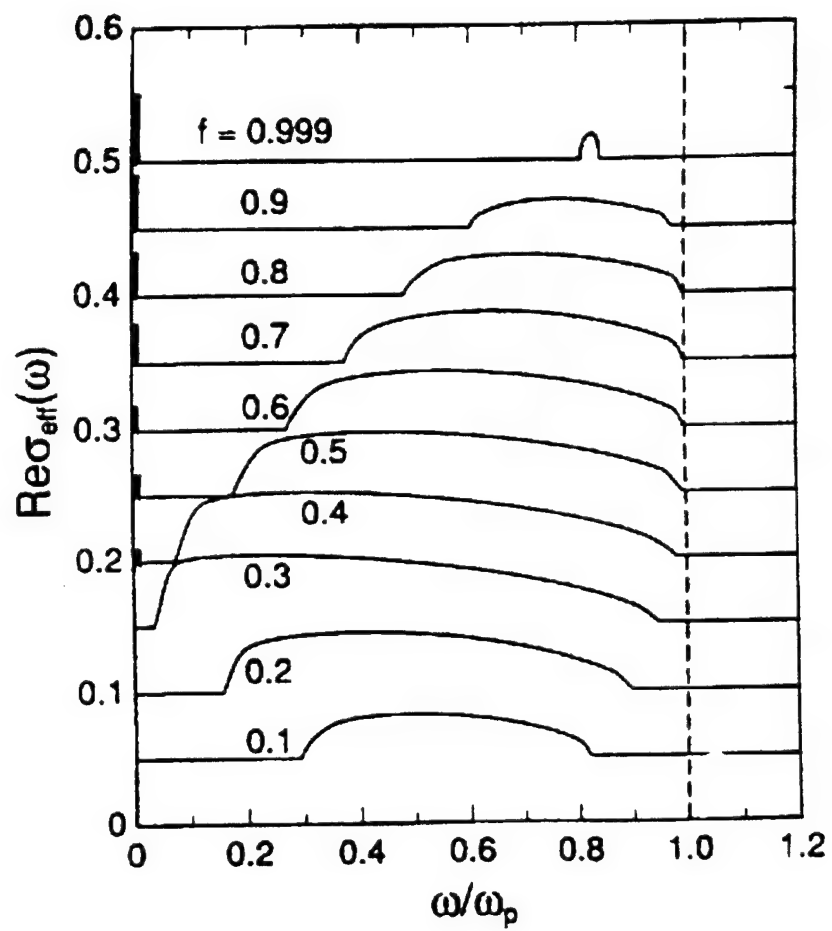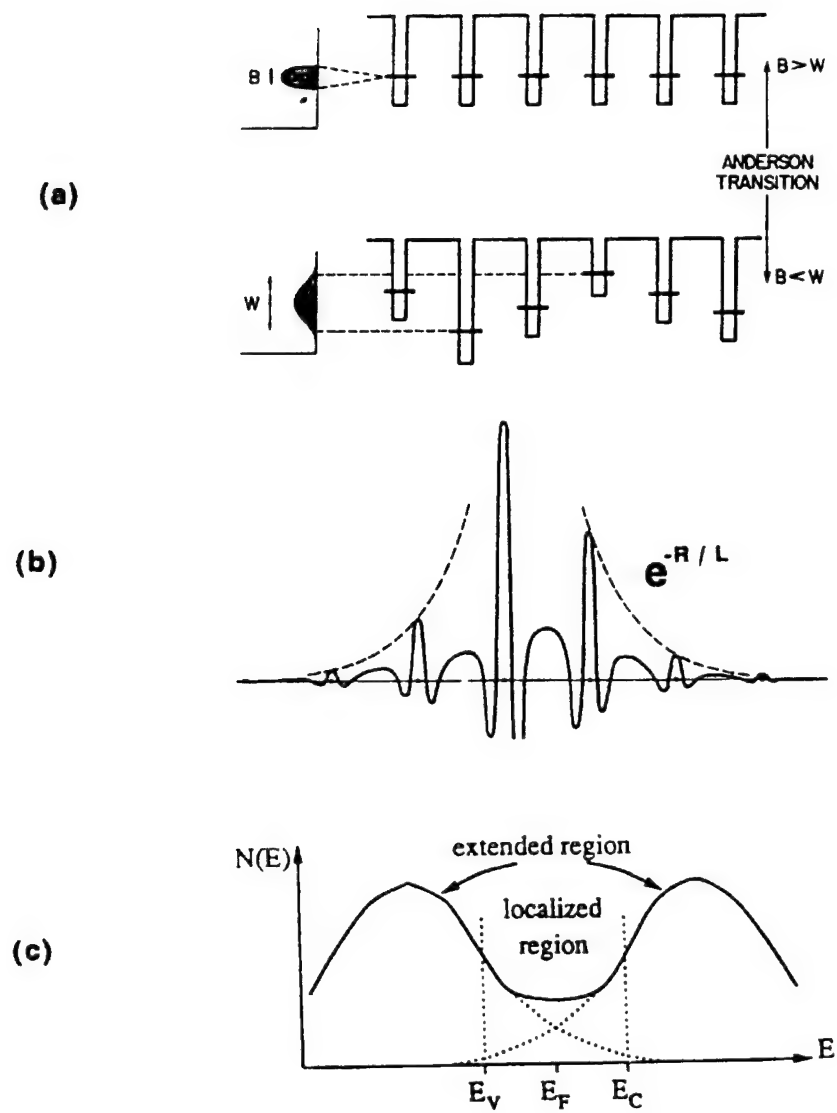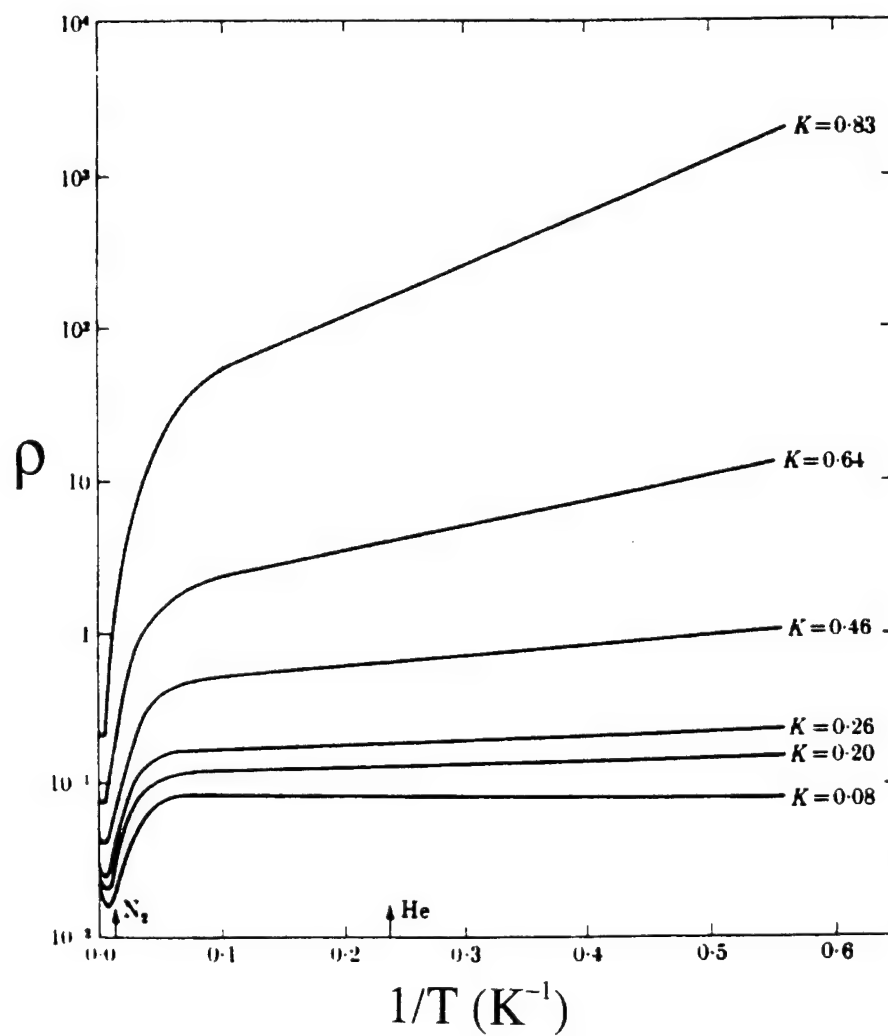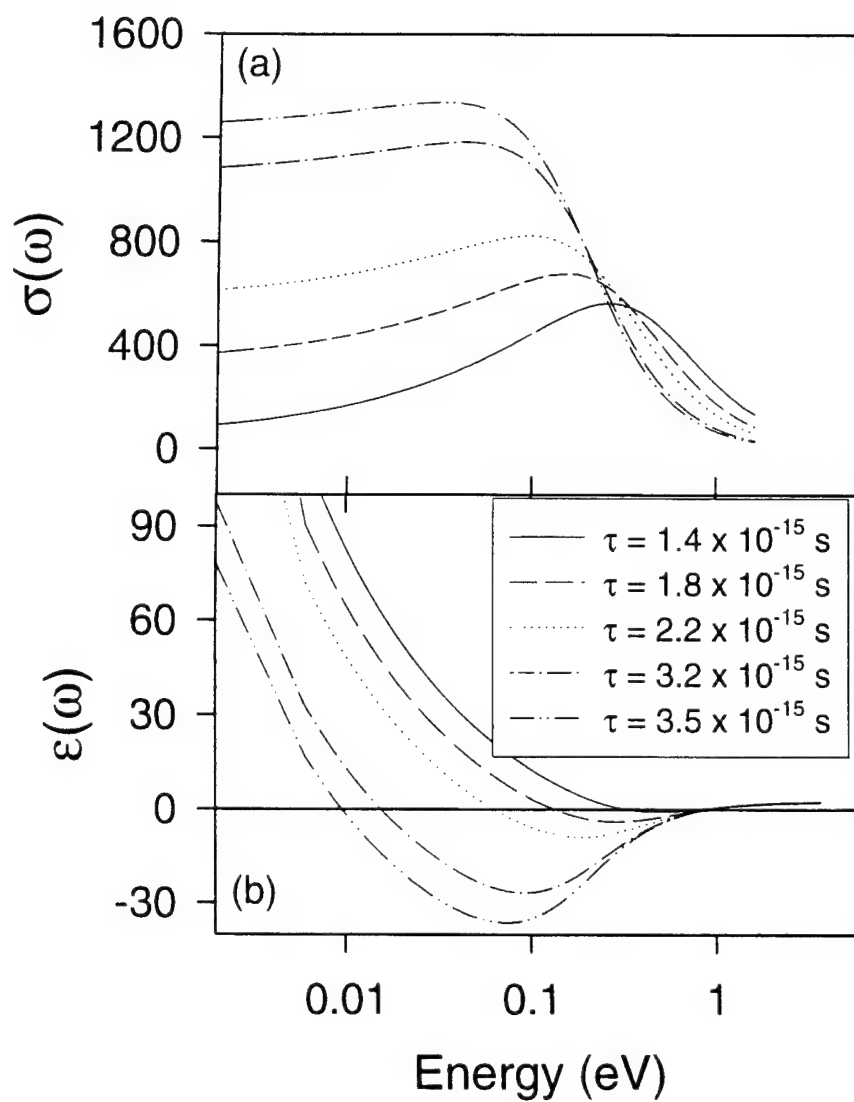
Figure 6

Figure 7

Figure 8
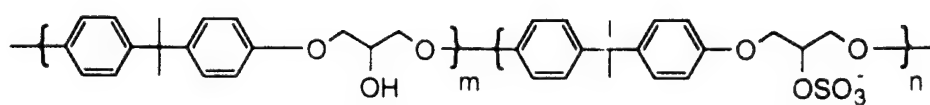
Figure 9
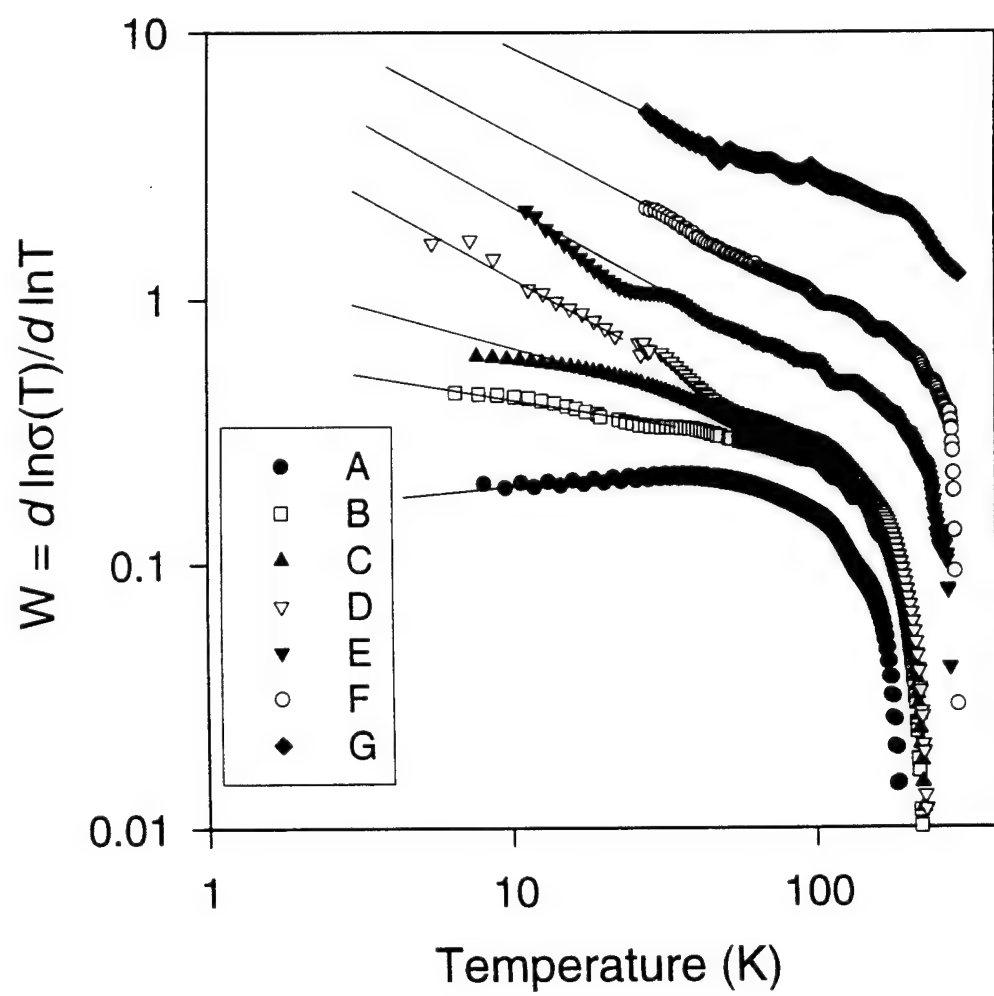
Figure 10
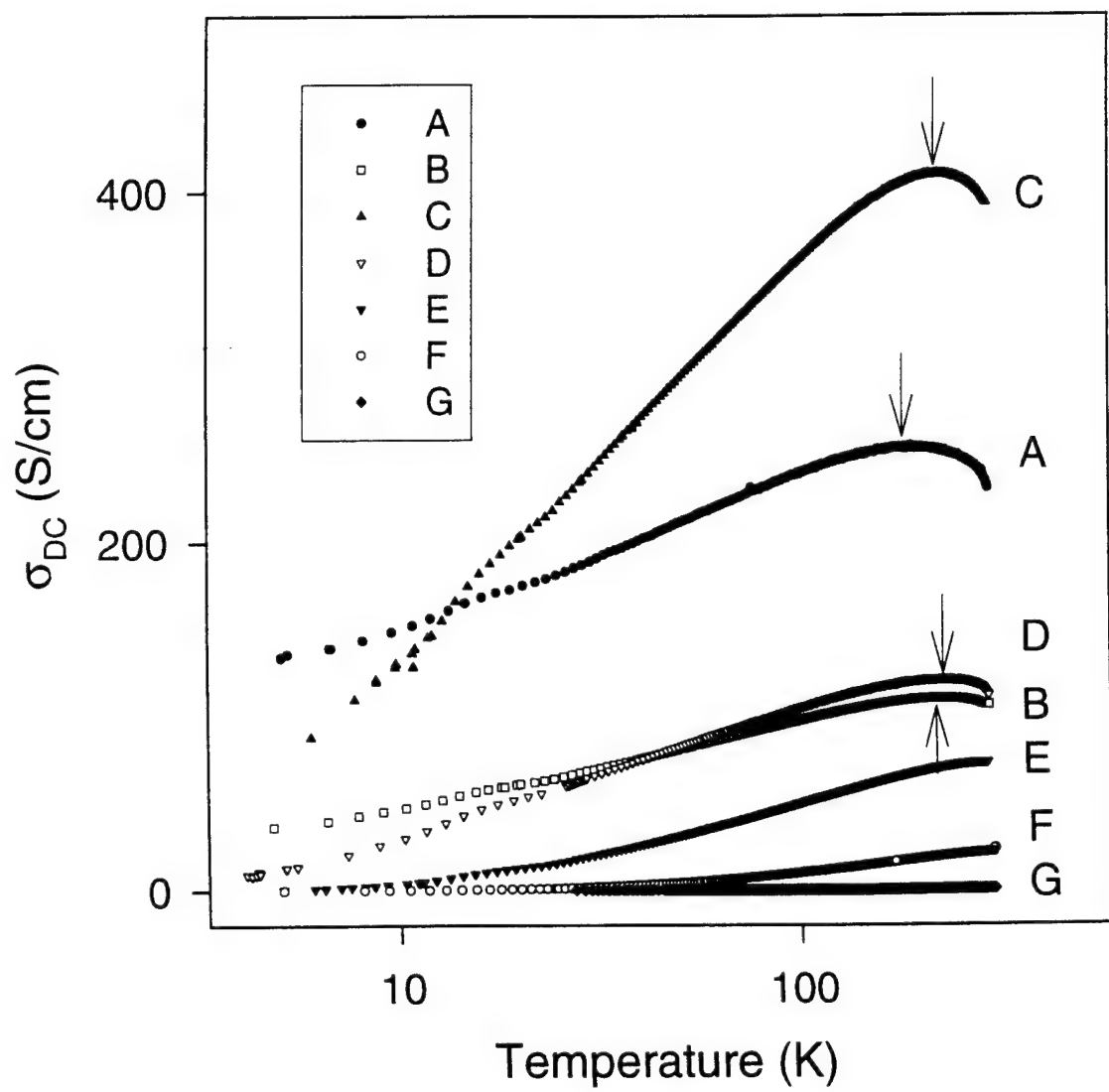
Figure 11
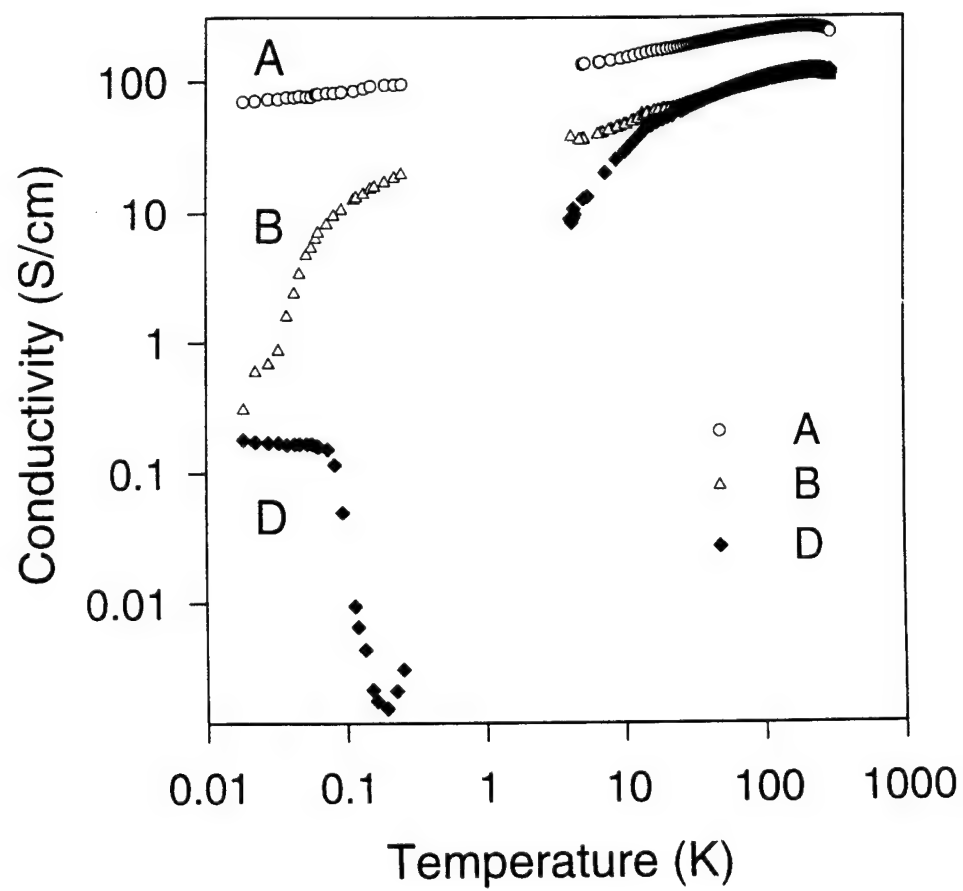
Figure 12
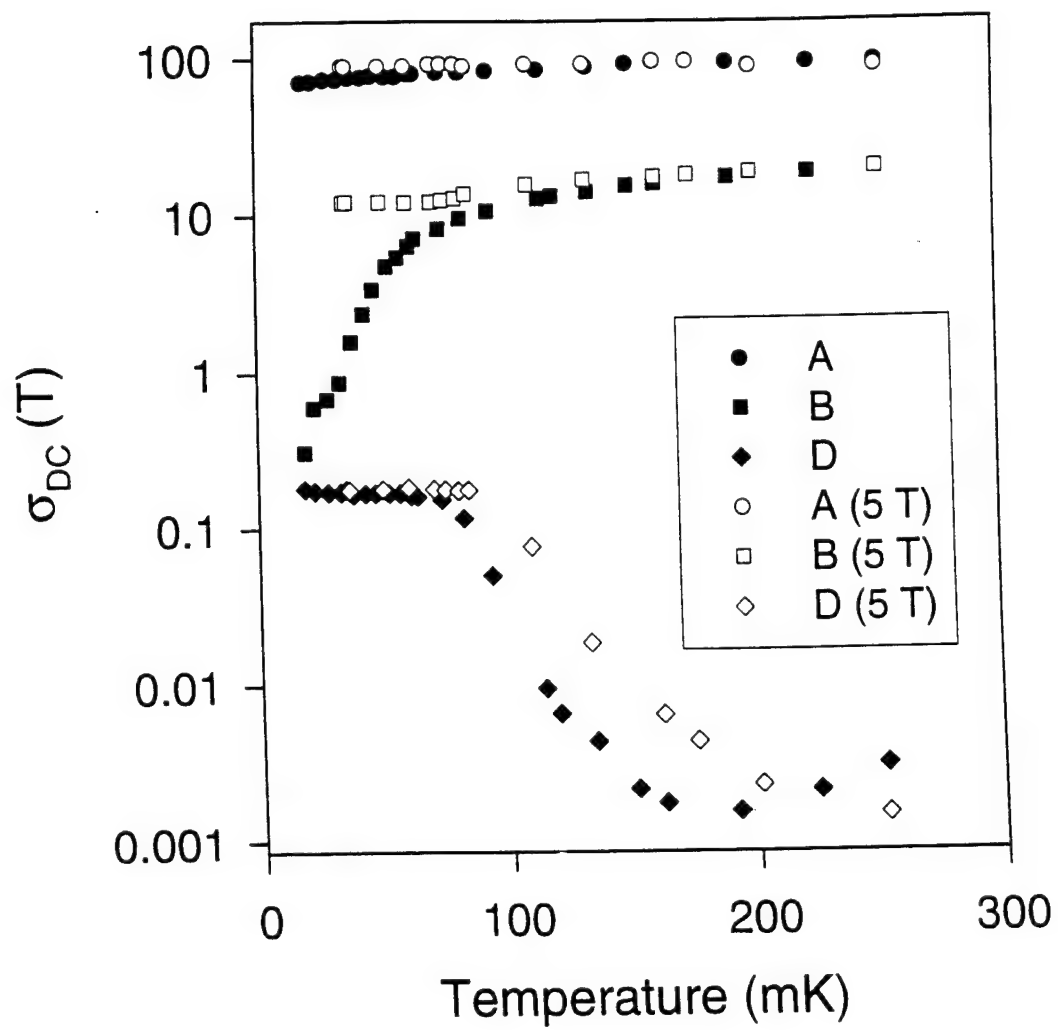
Figure 13
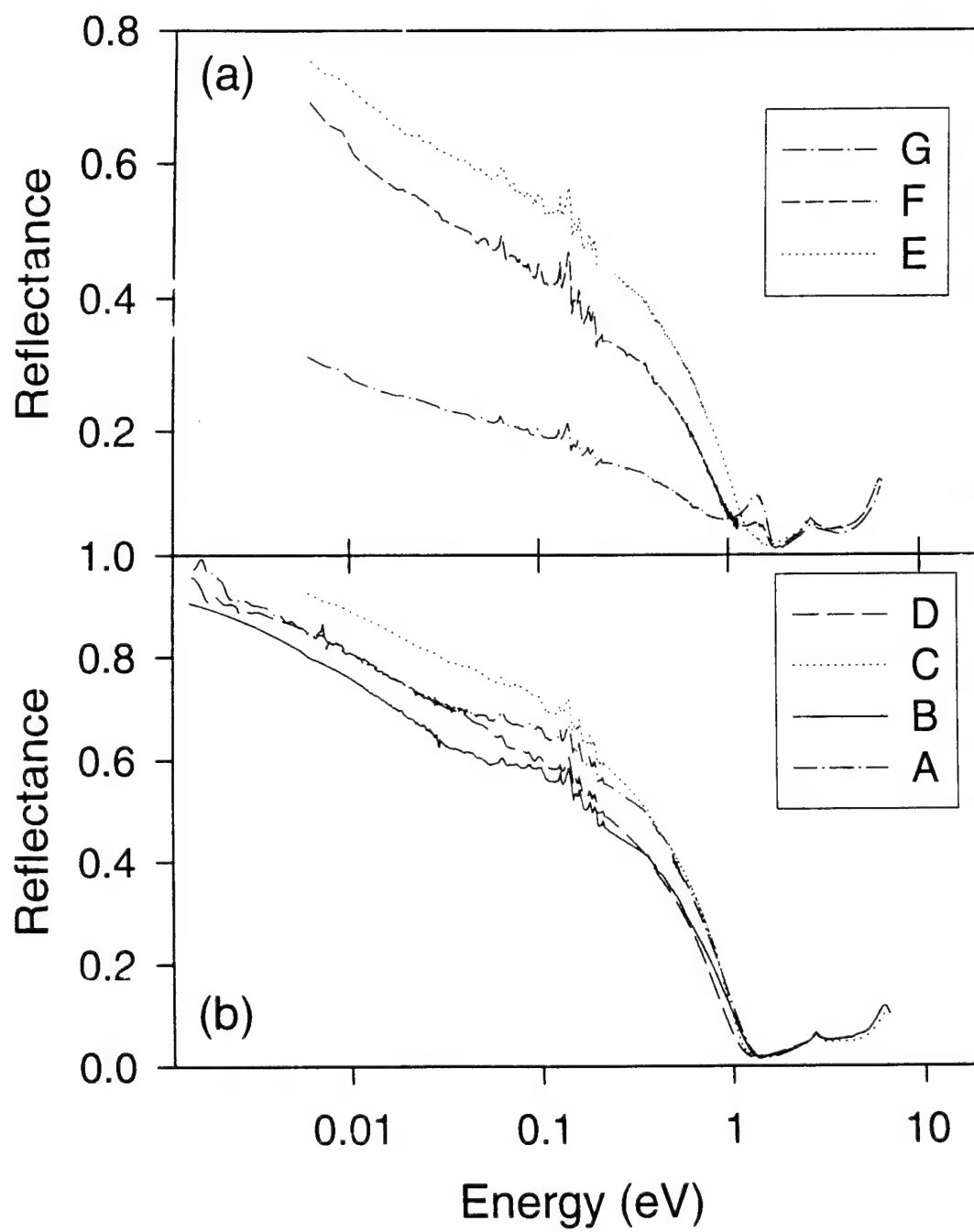
Figure 14
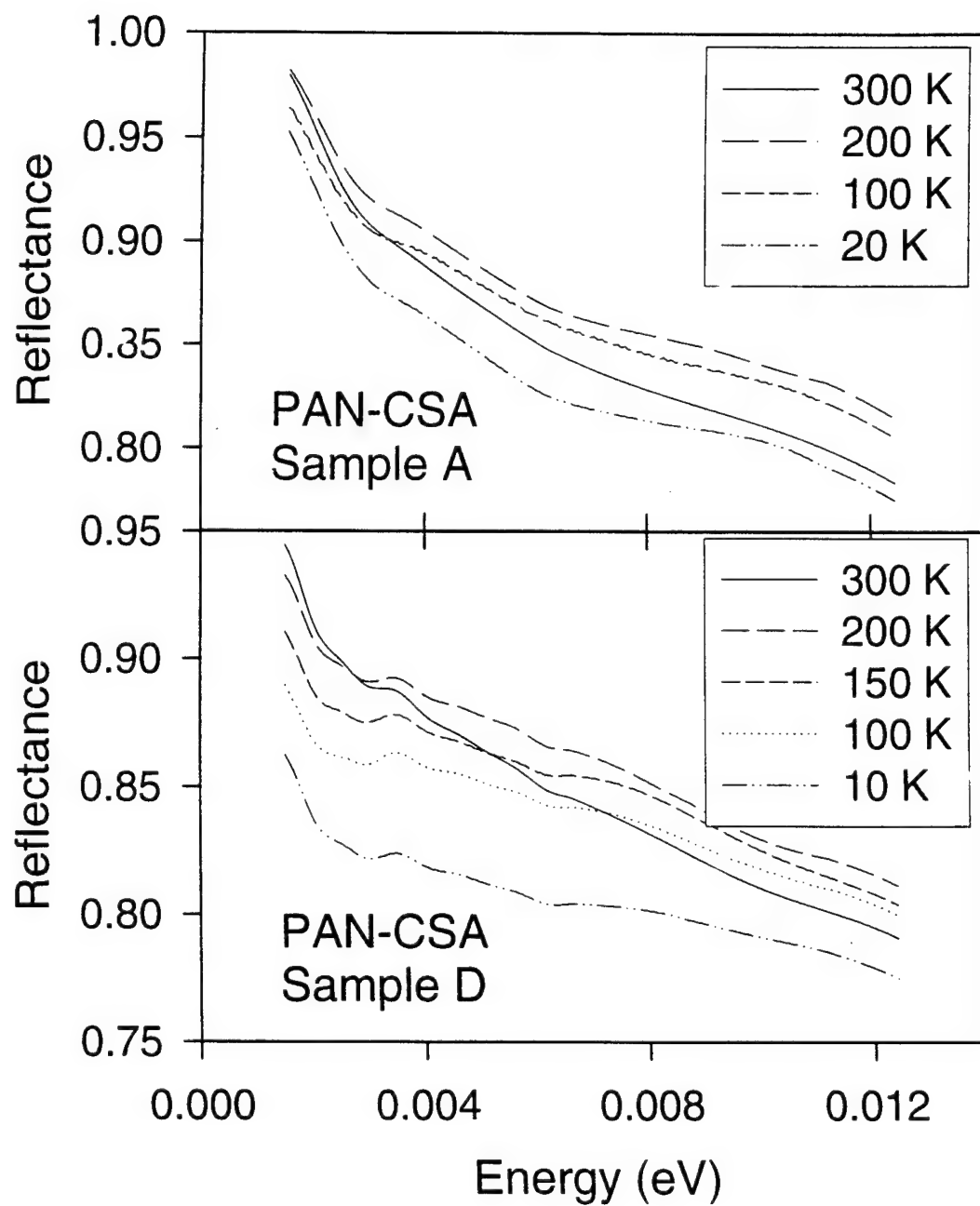
Figure 15
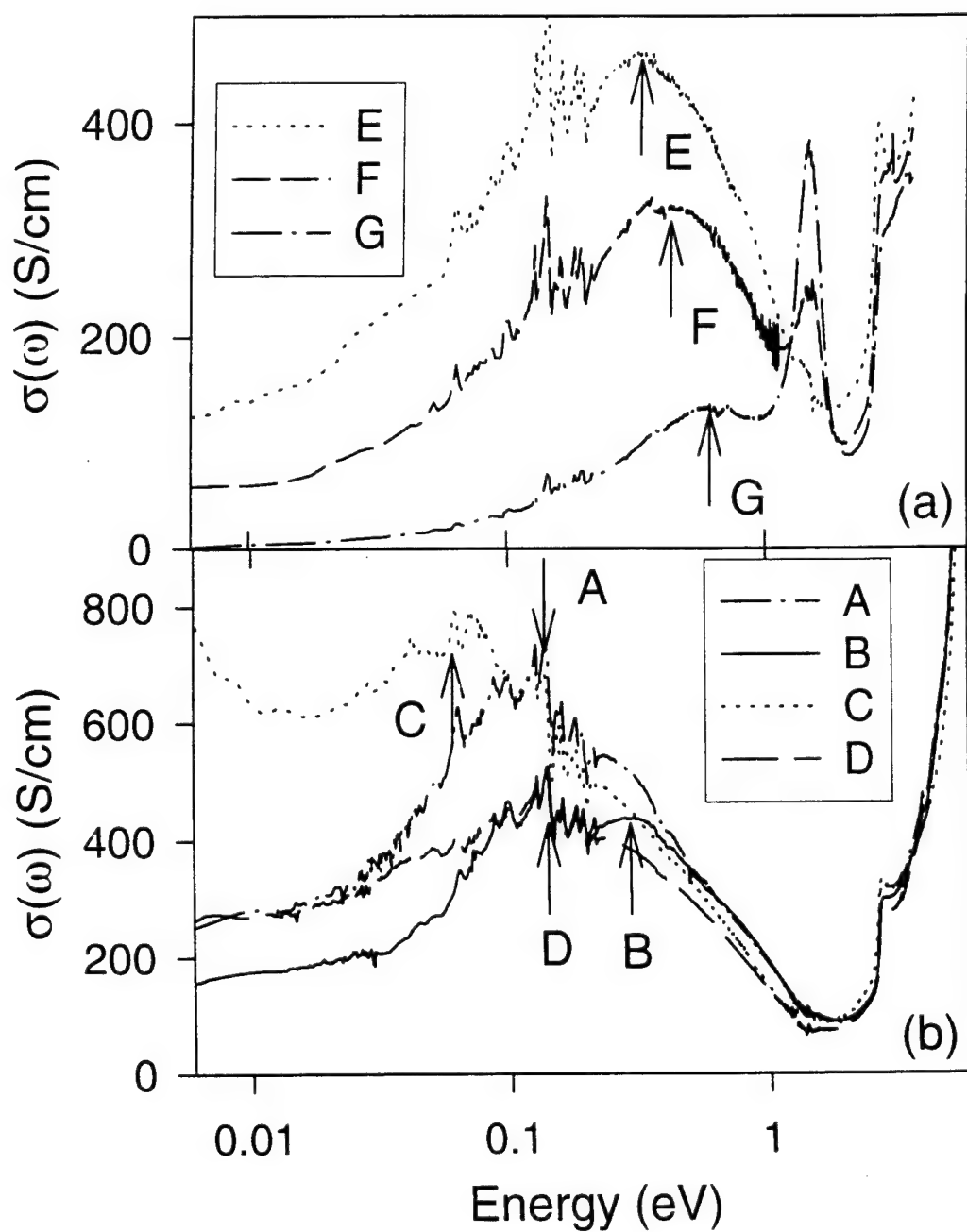
Figure 16
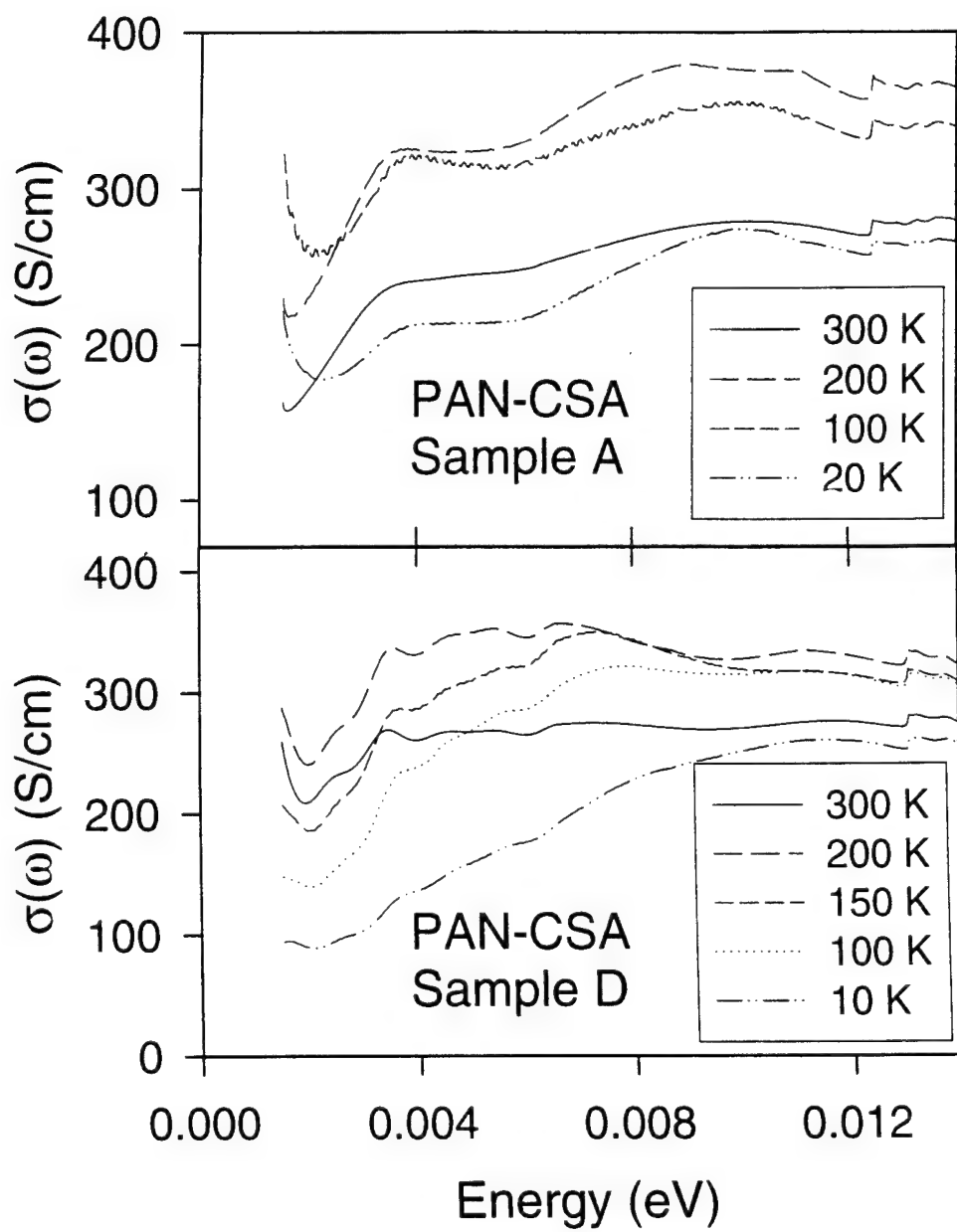
Figure 17
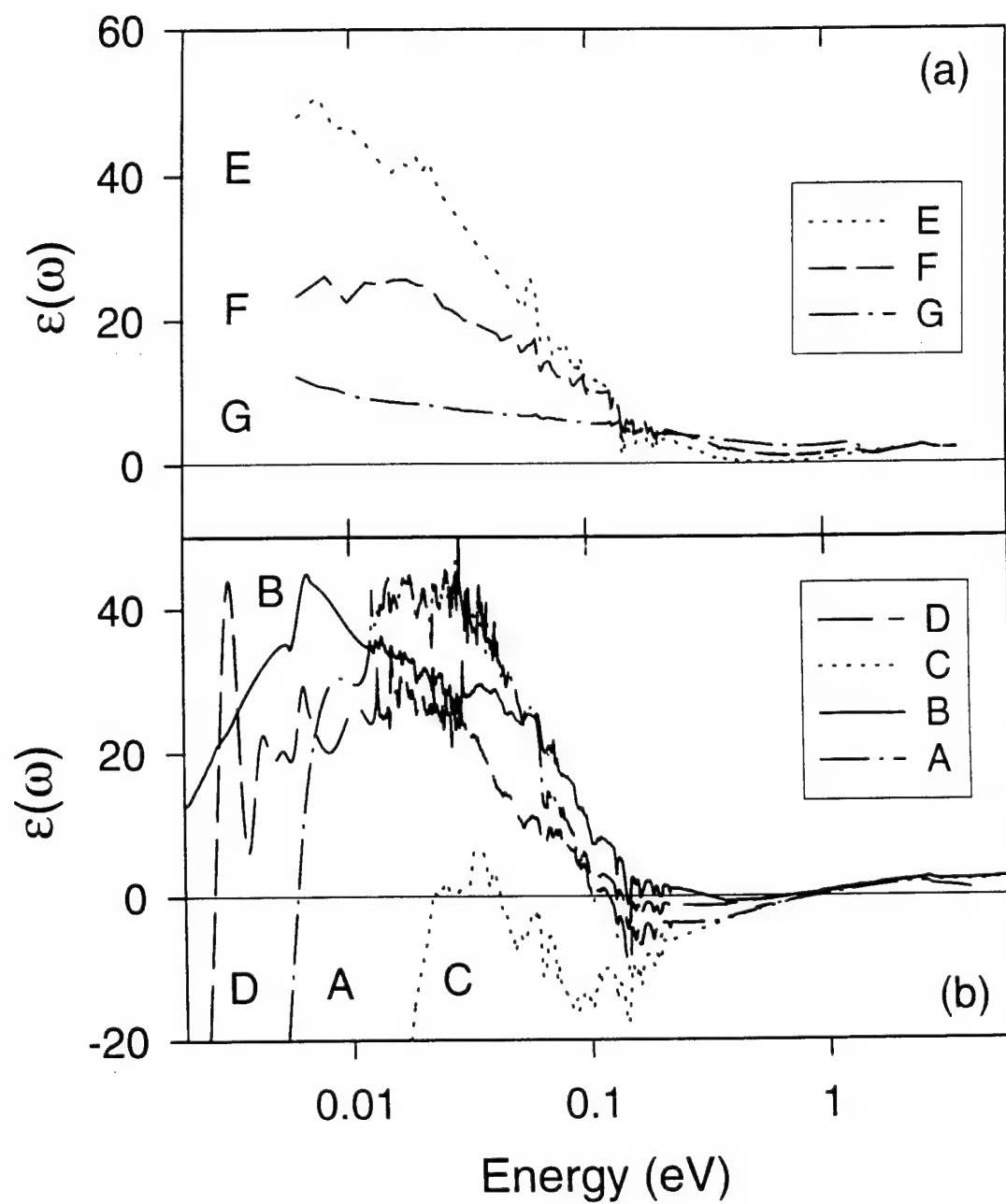
Figure 18
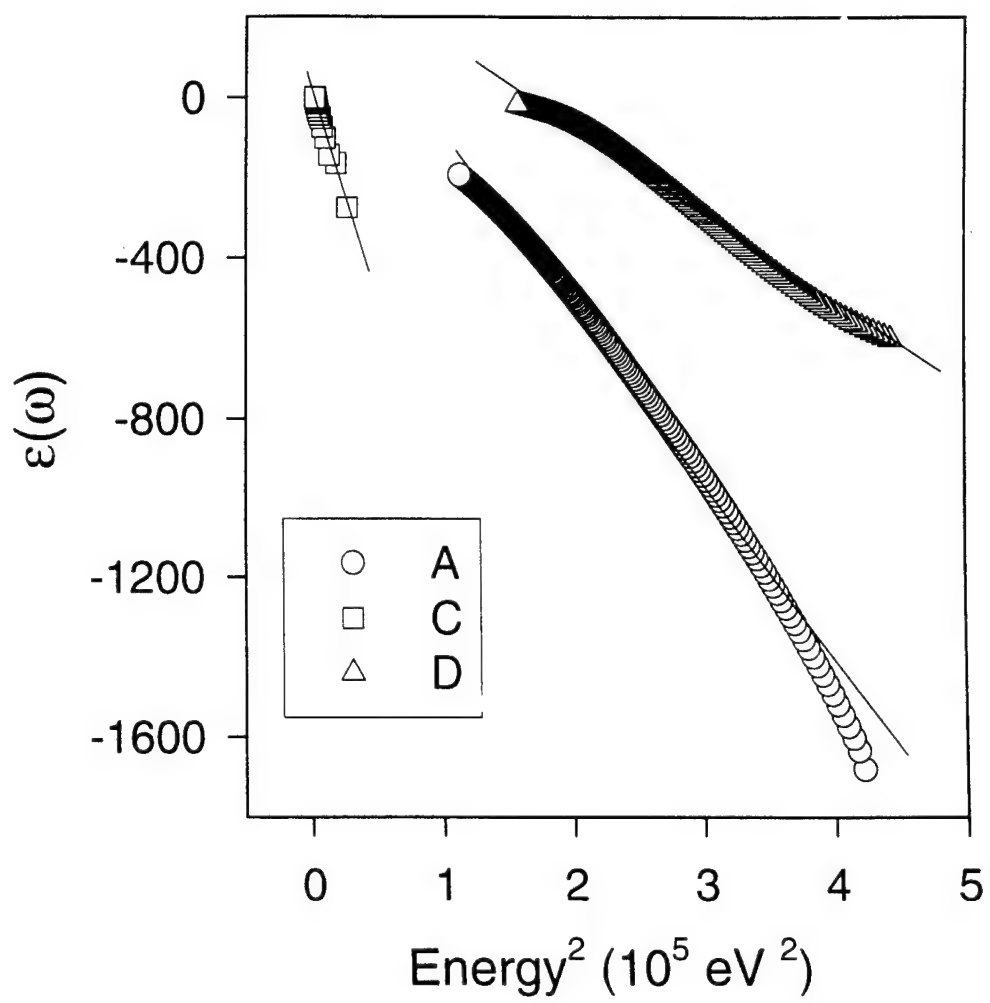
Figure 19

Figure 20

Figure 21.

Emeraldine Salt, $E_{\parallel}$ (a)

ε_1

Emeraldine Salt, $E_{\perp}$ (b)

ε_1
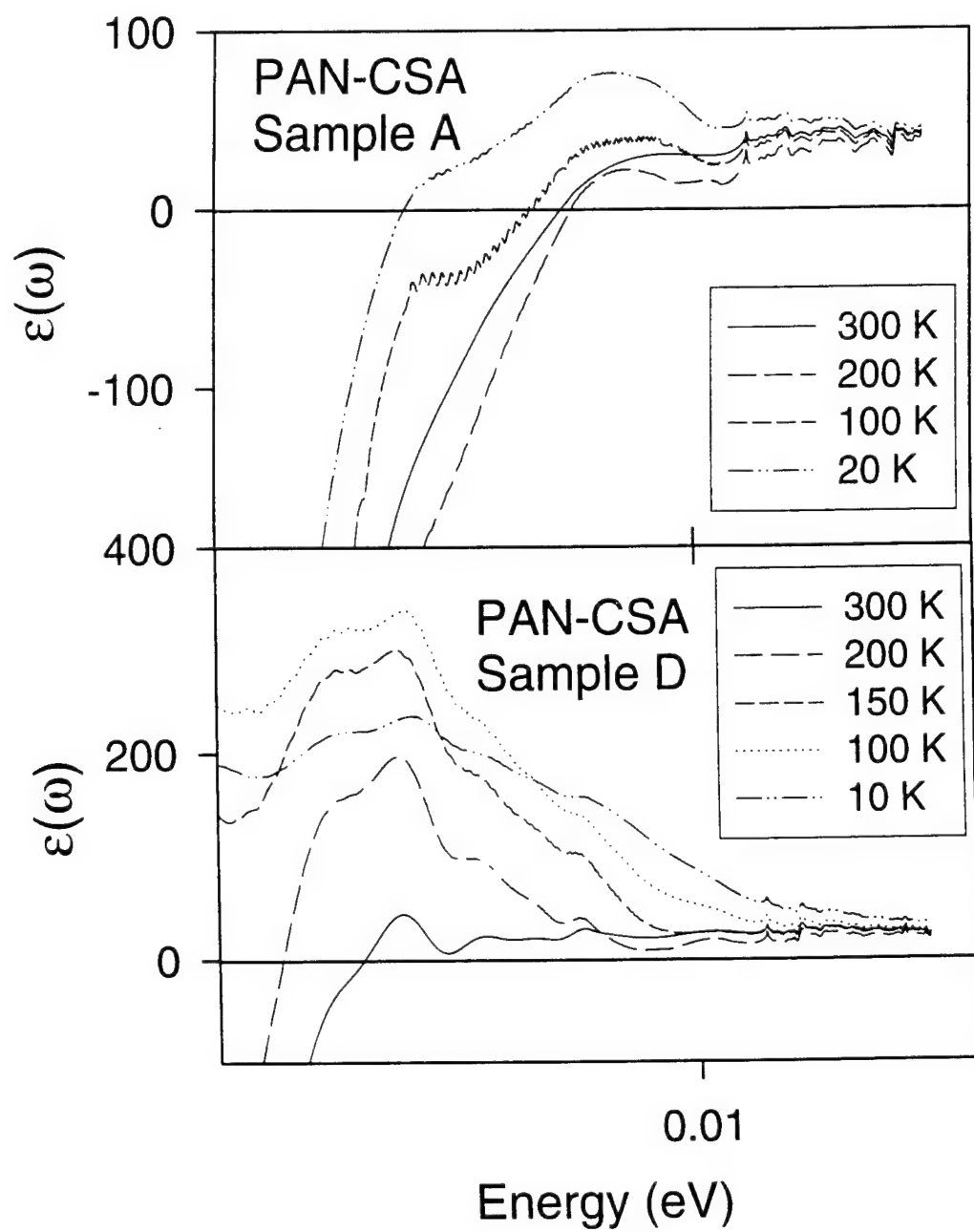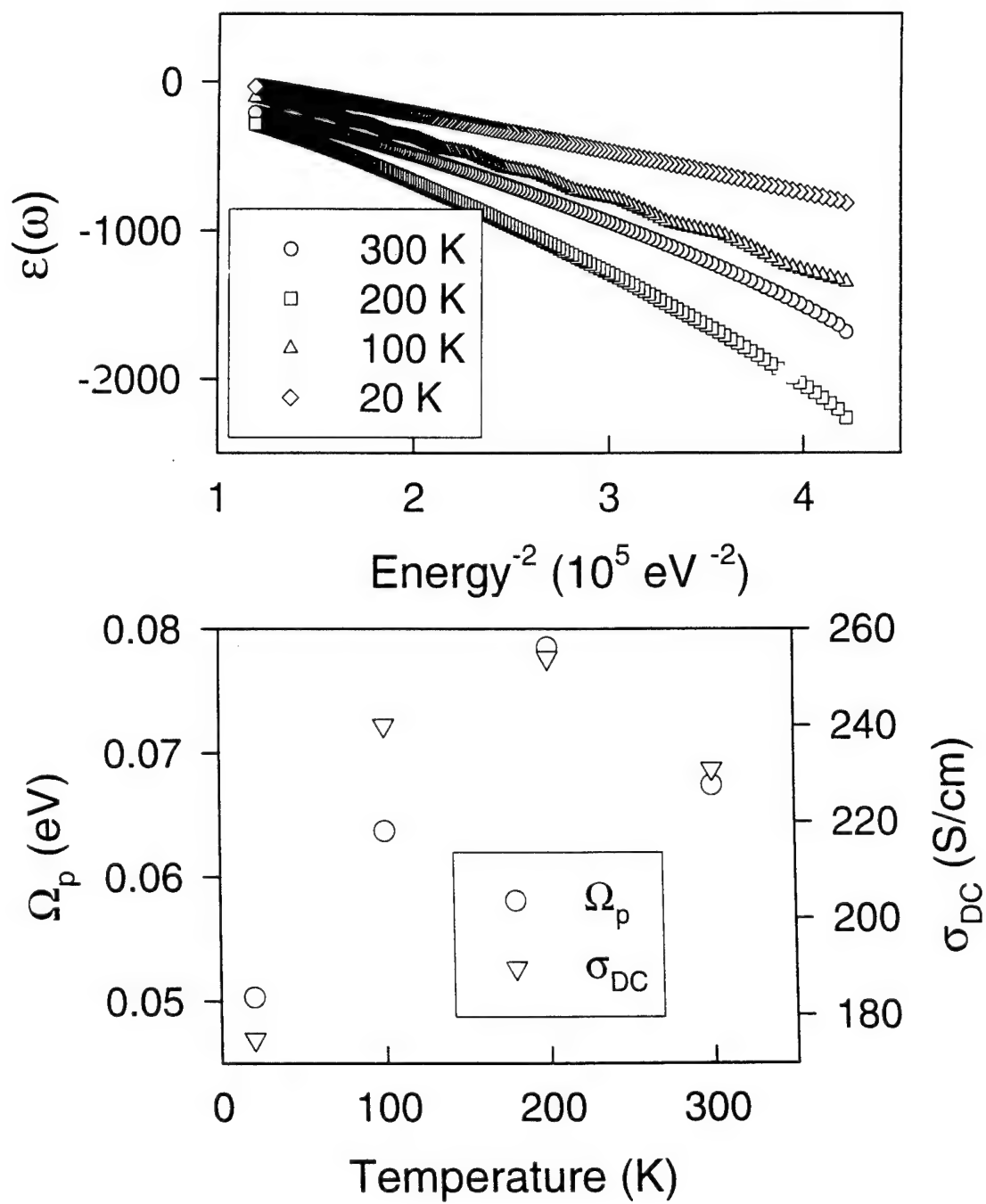
Energy (cm^{-1})
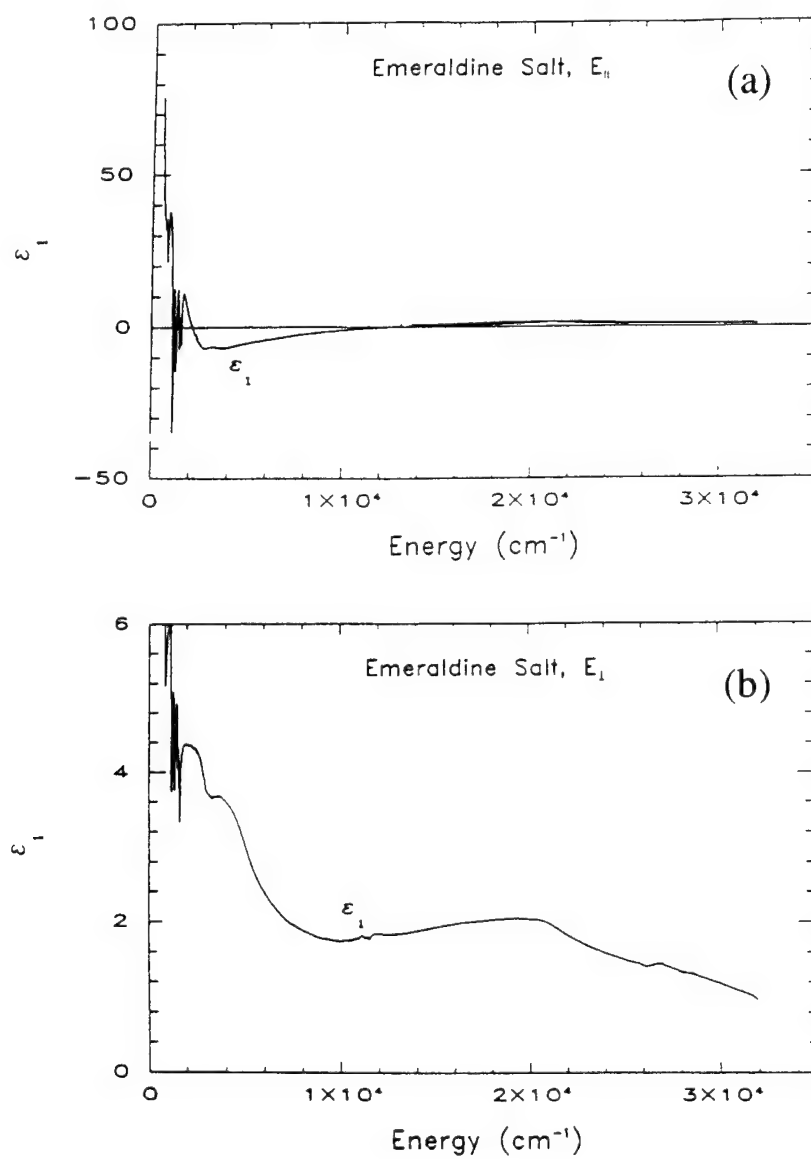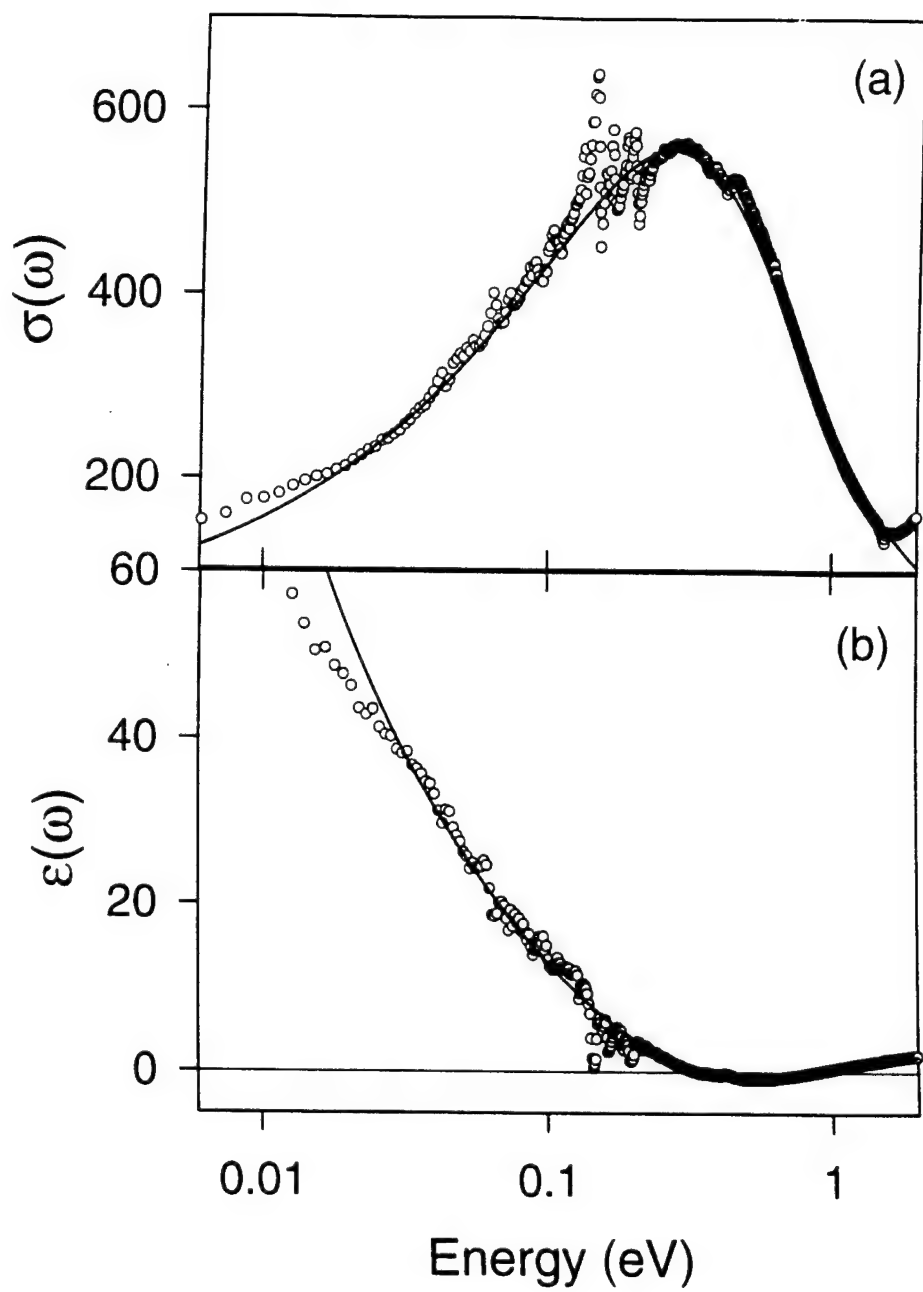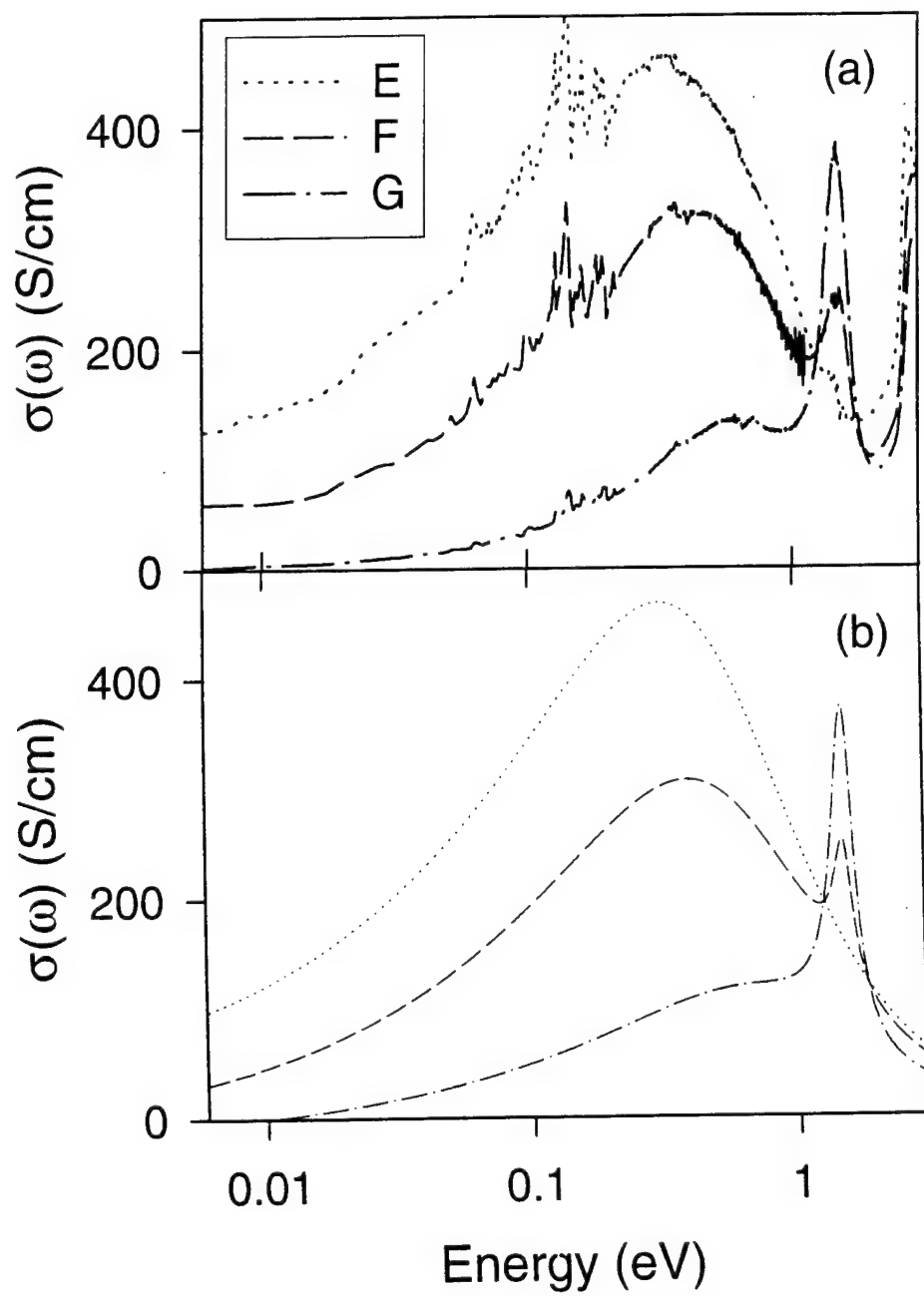
Figure 22

Figure 22

Figure 24
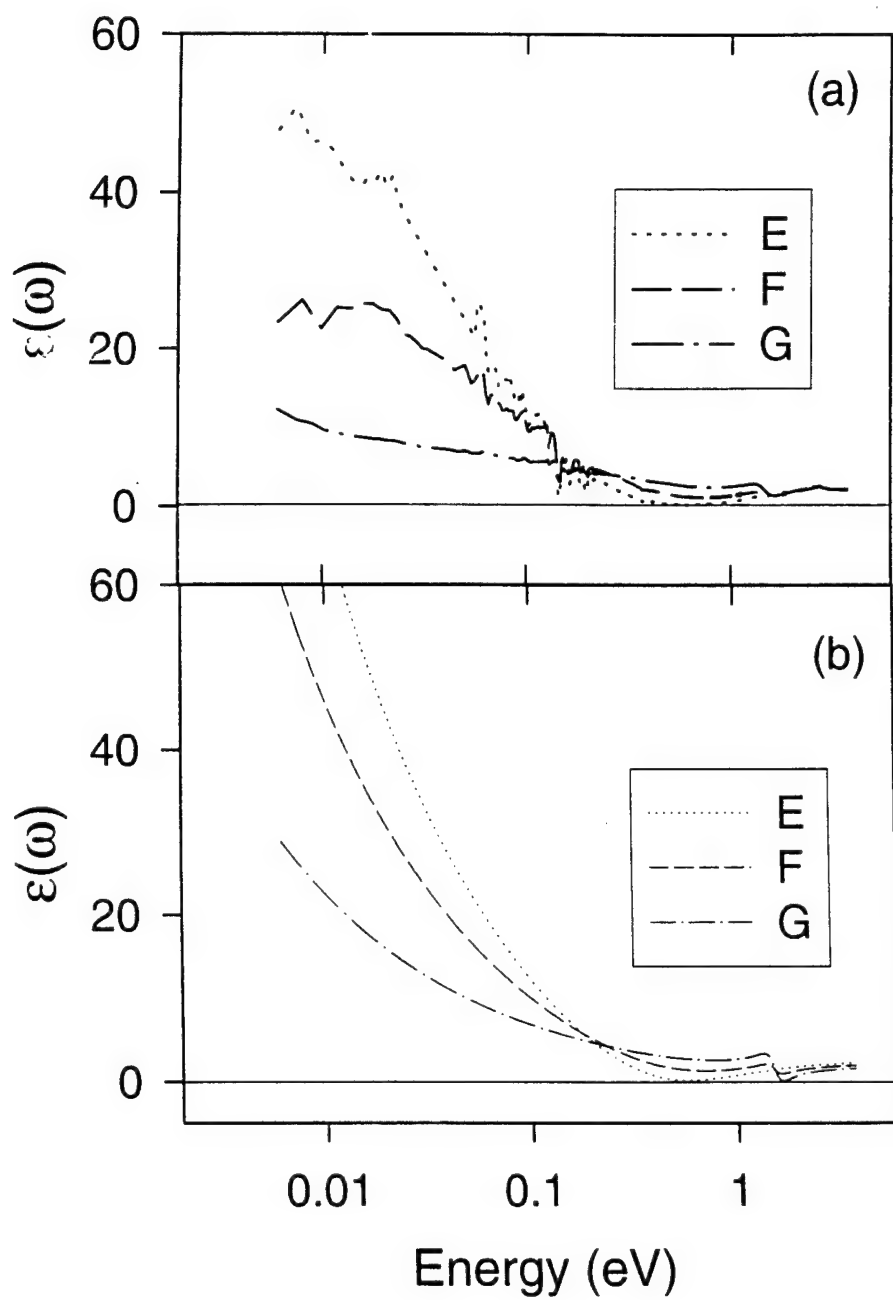
Figure 25
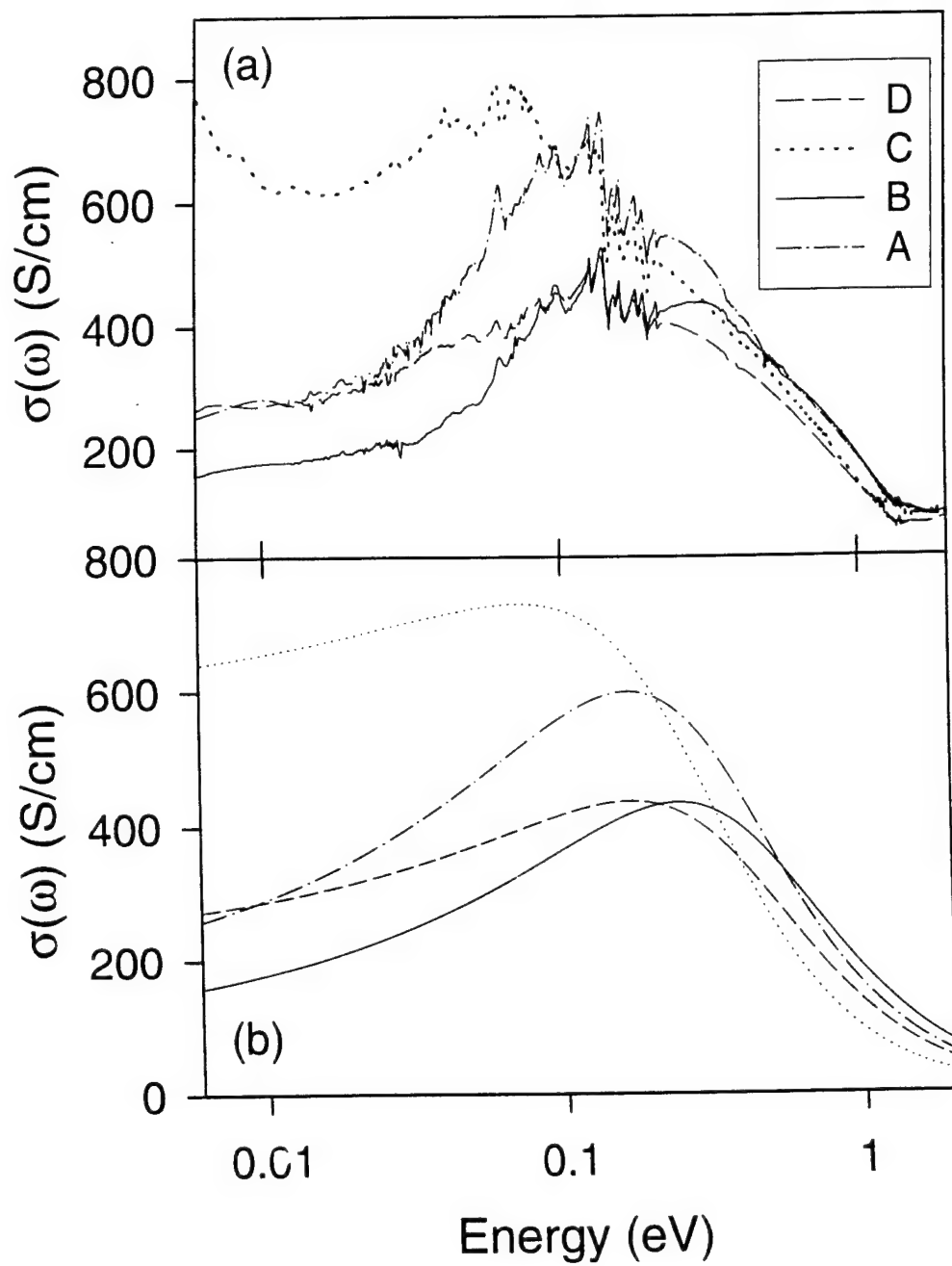
Figure 26
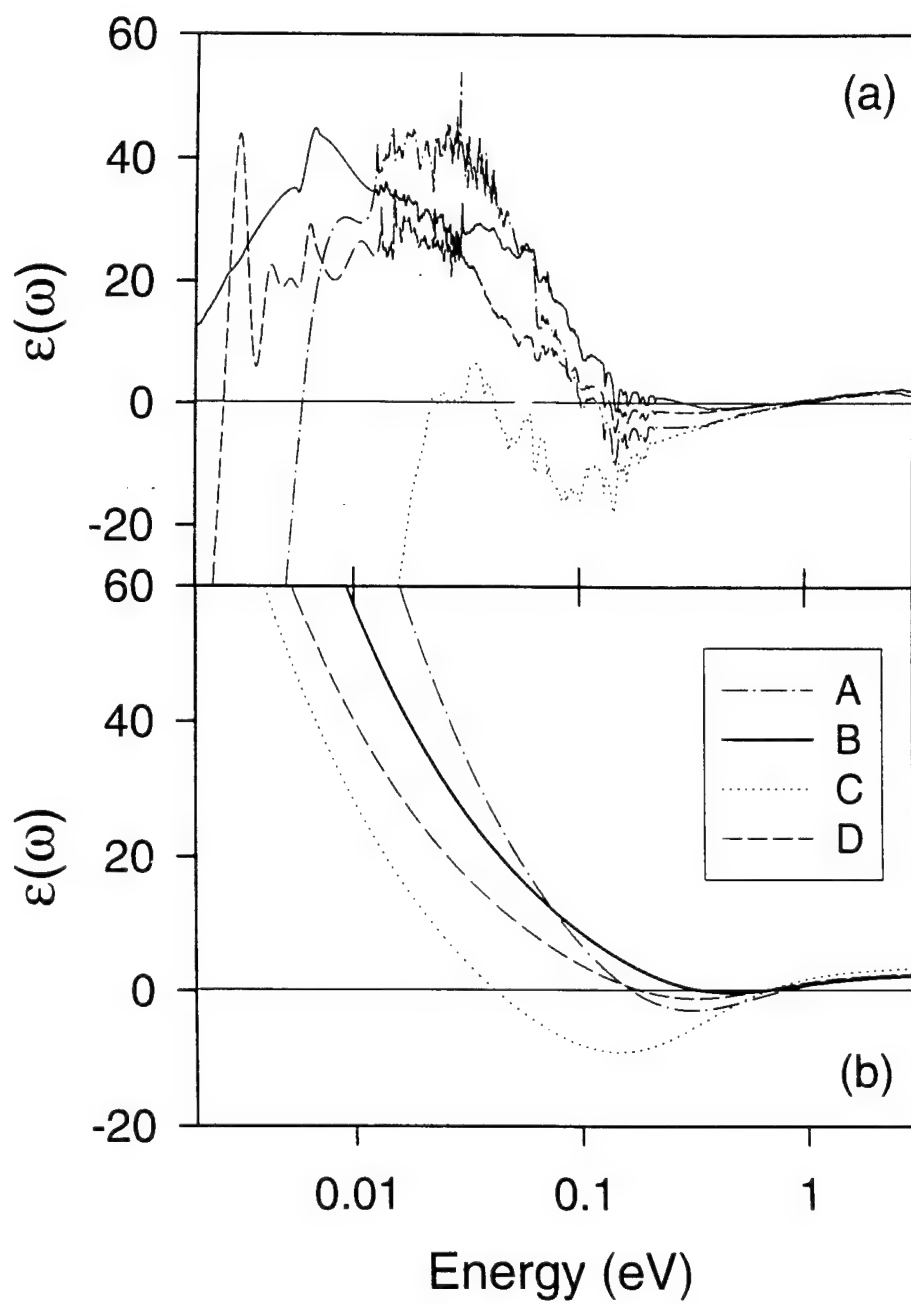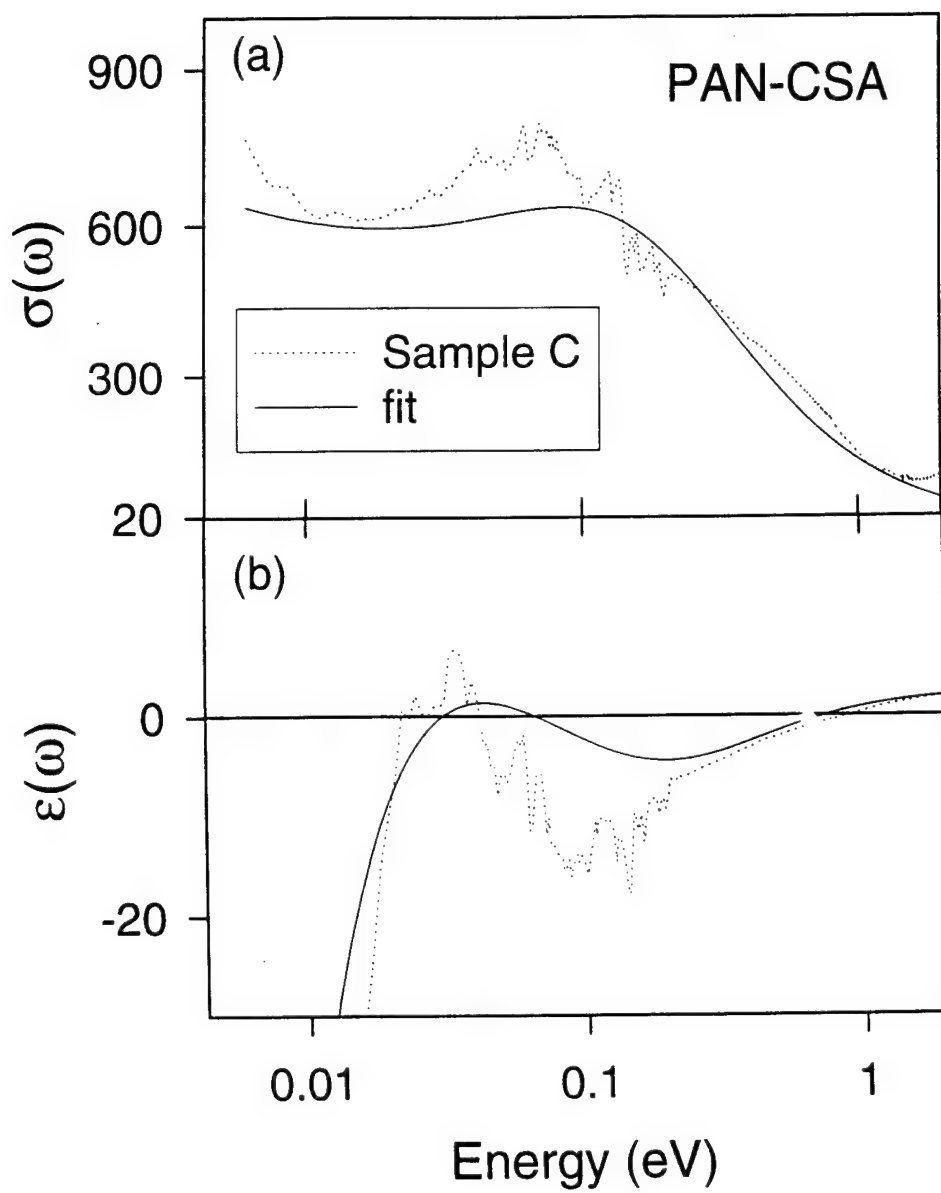
Figure 27.
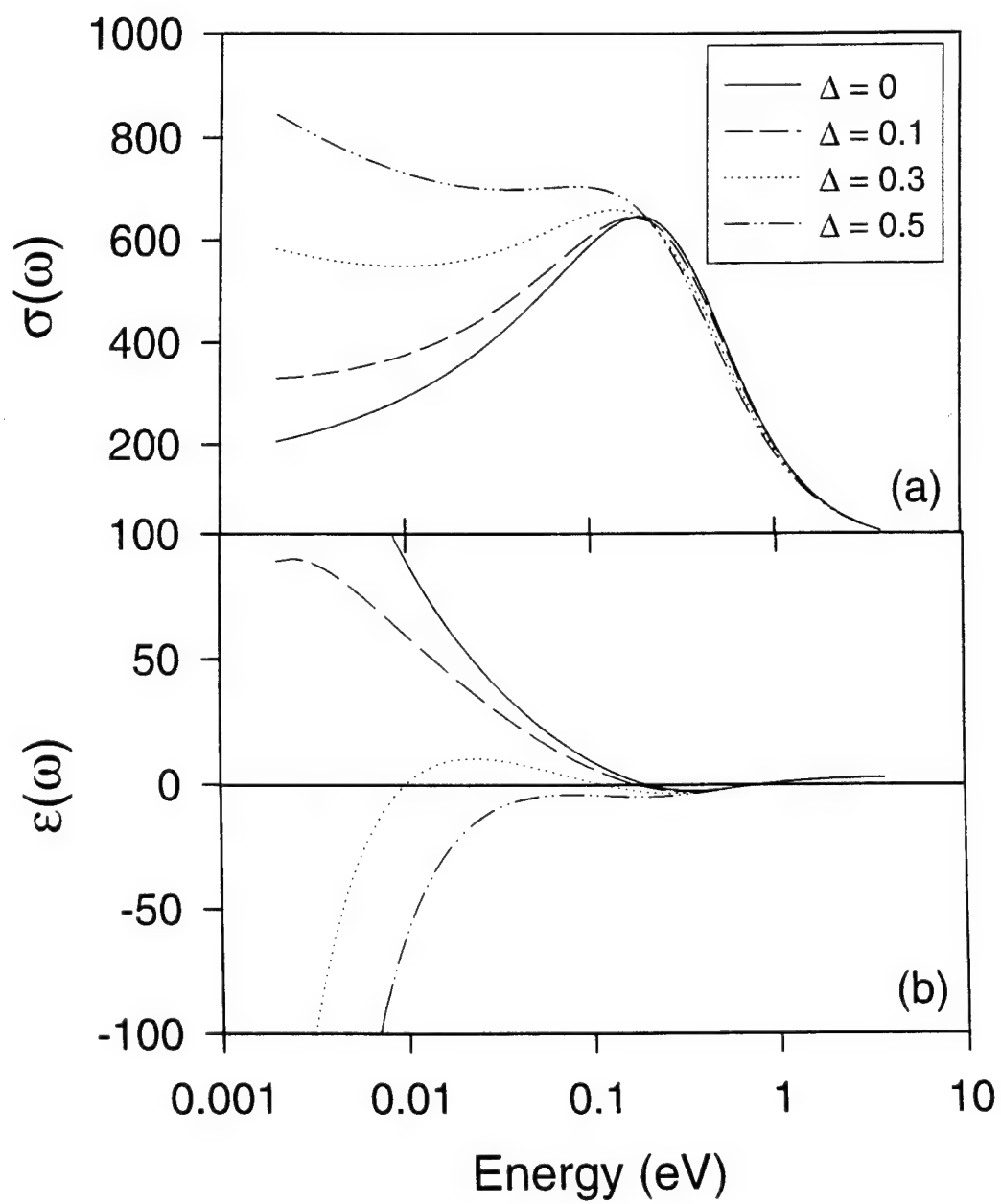
Figure 28

Figure 29
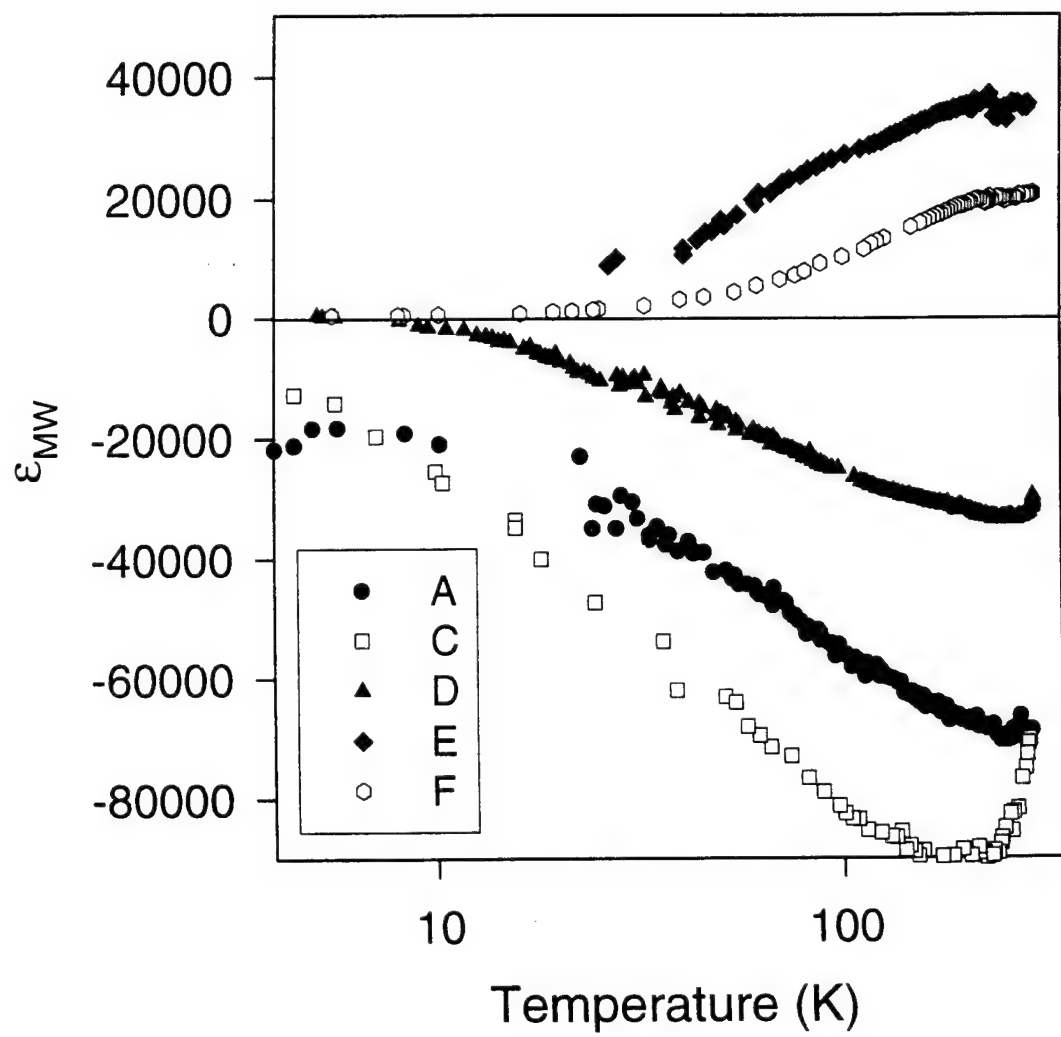
Figure 30
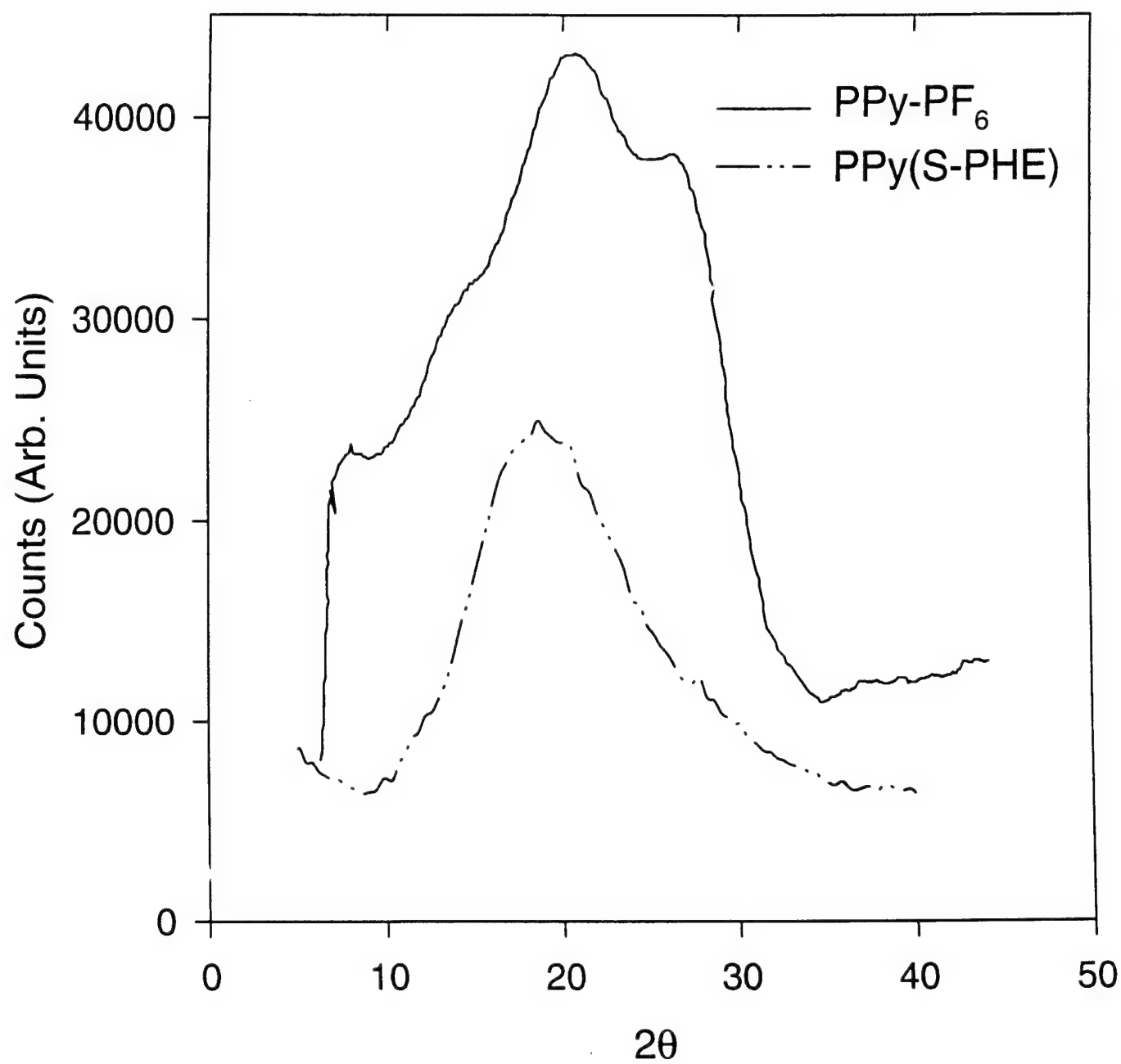
Figure 31
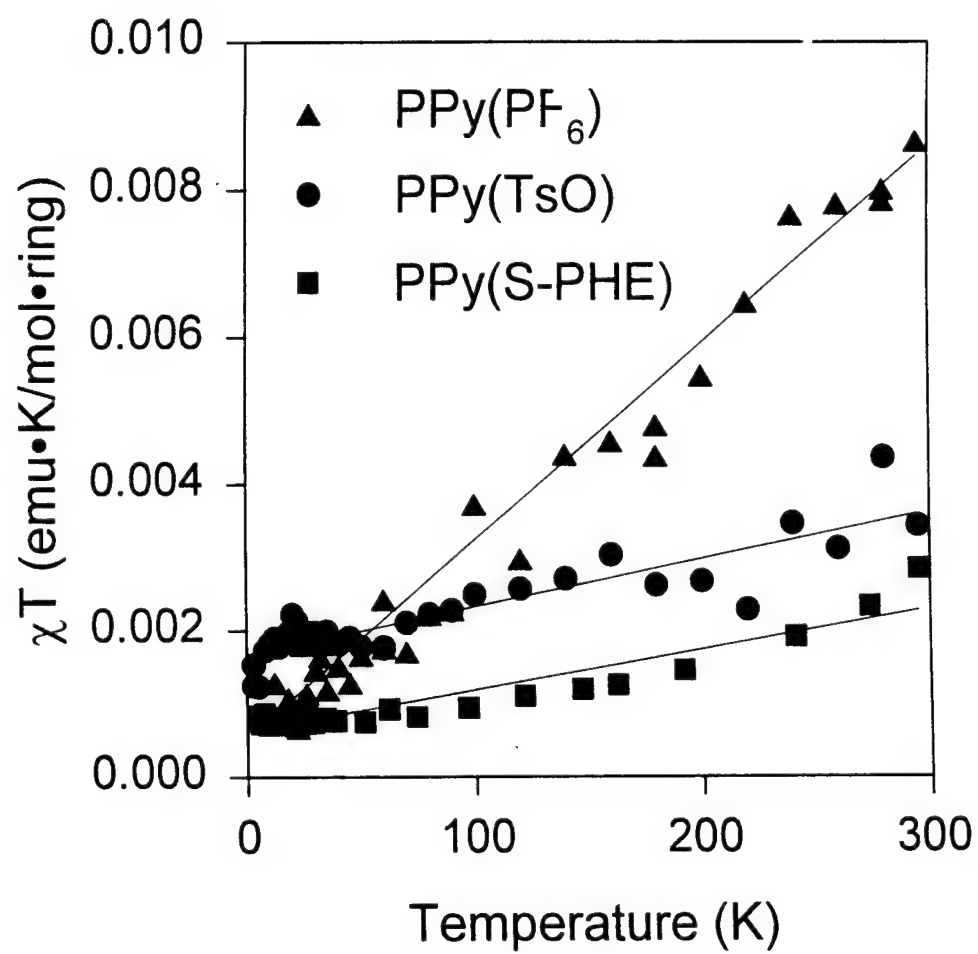
Figure 32
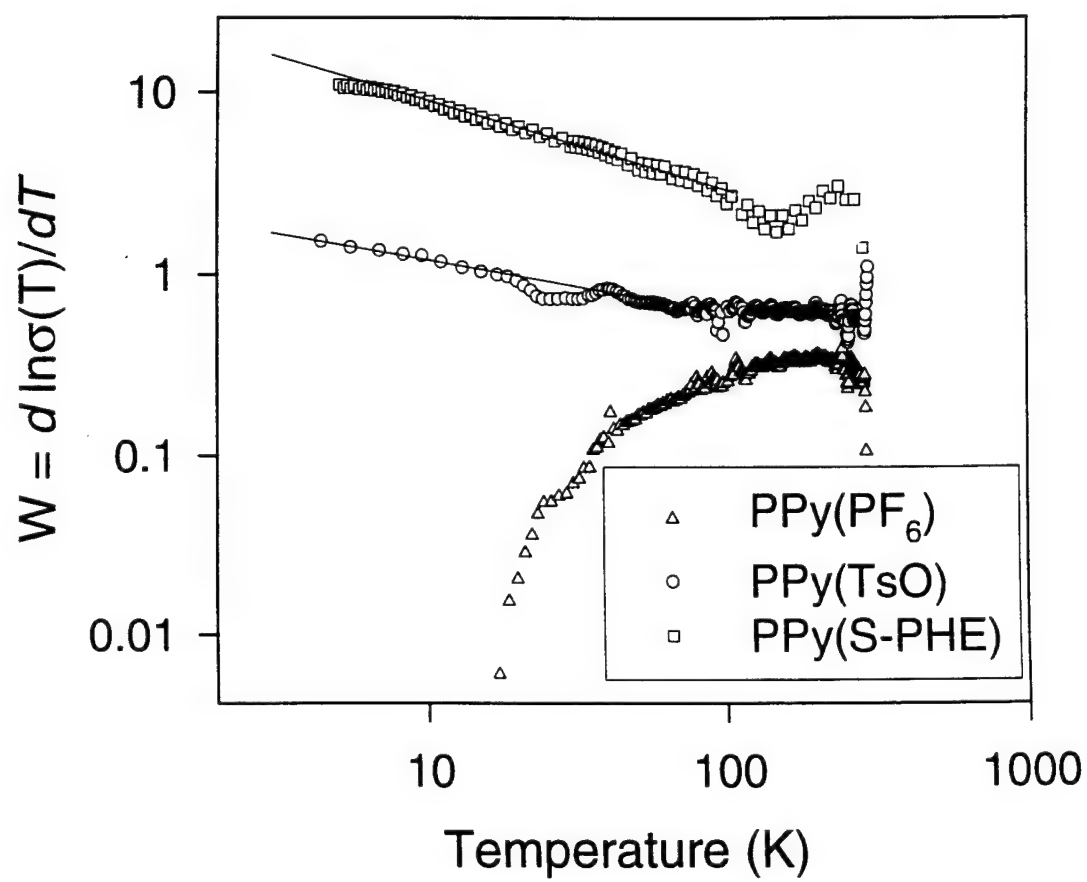
Figure 33
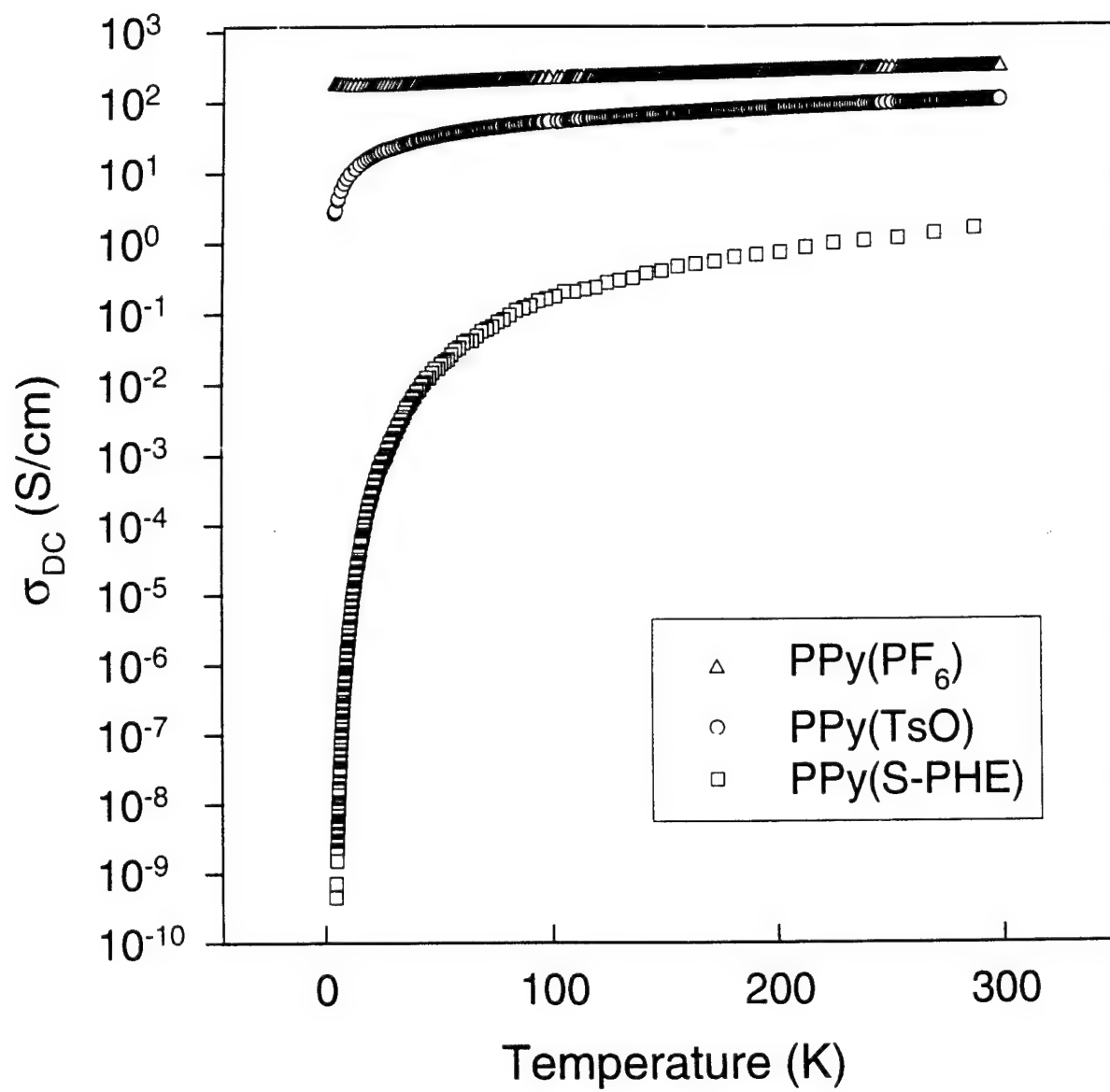
Figure 34
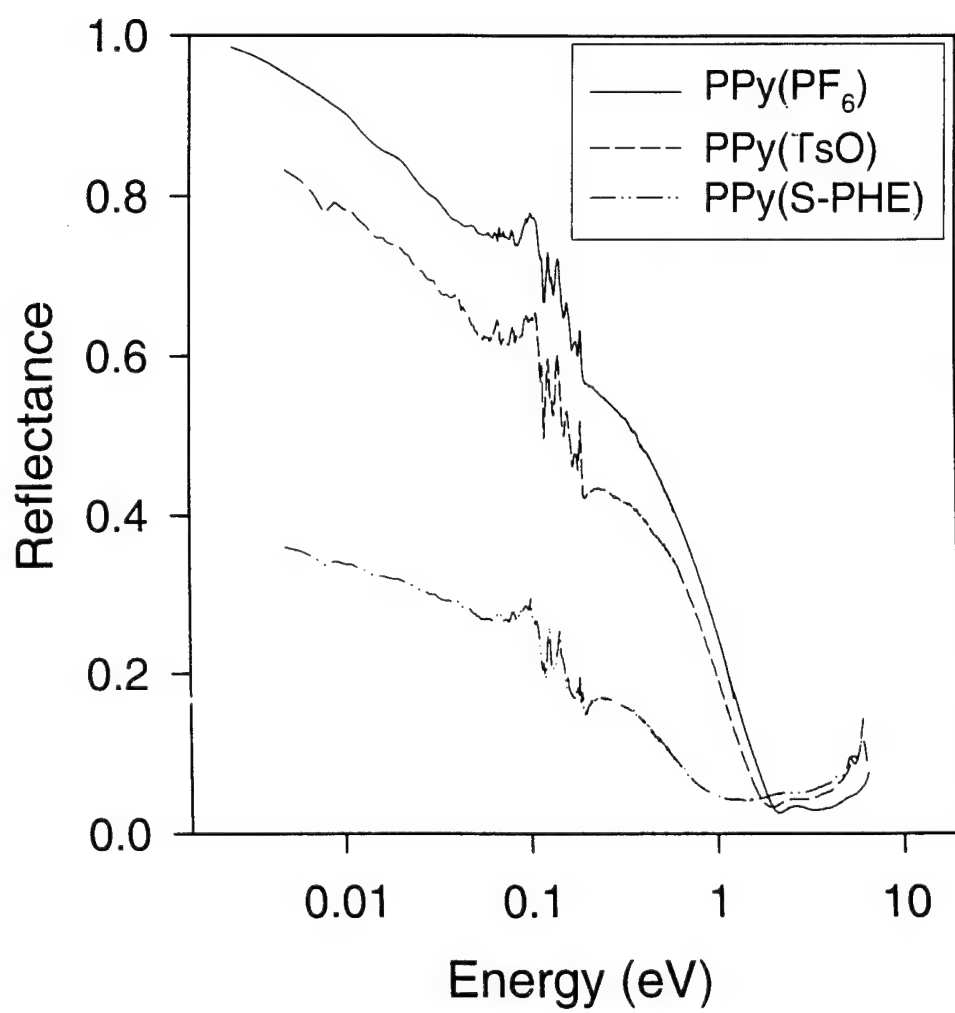
Figure 35

Figure 36

Figure 37

(a)

α (10⁵ cm⁻¹) vs Energy (eV)

- - - 10 K
—— 300 K

PPy-PF₆

(b)

- - - 10 K
—— 300 K

PPy-PF₆
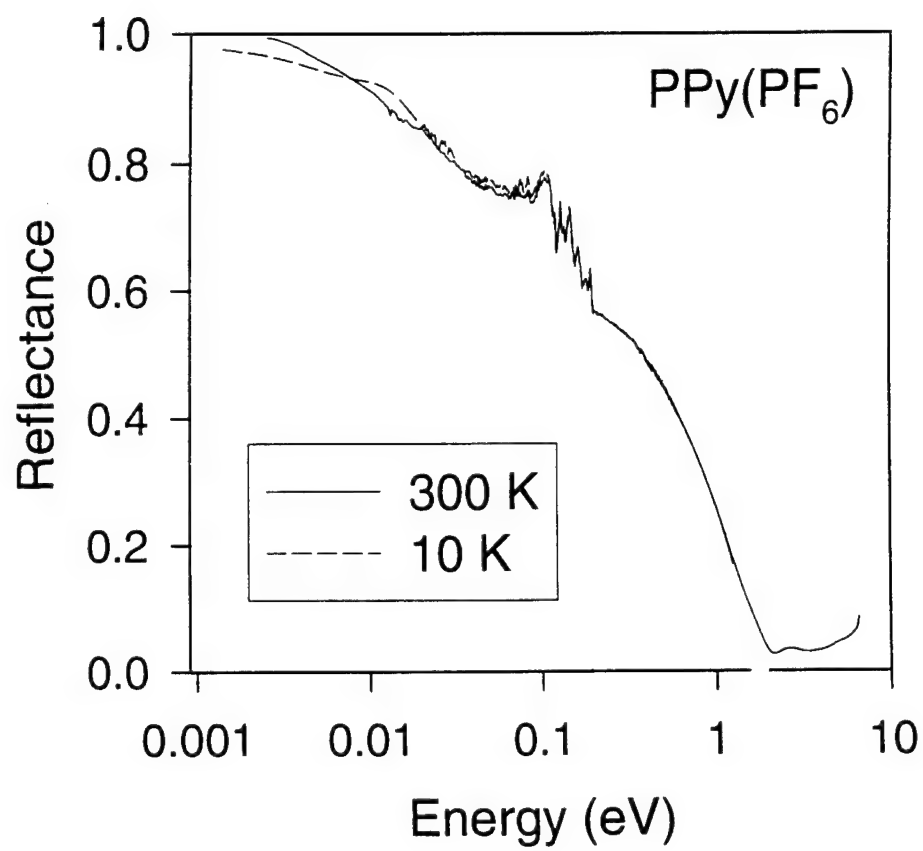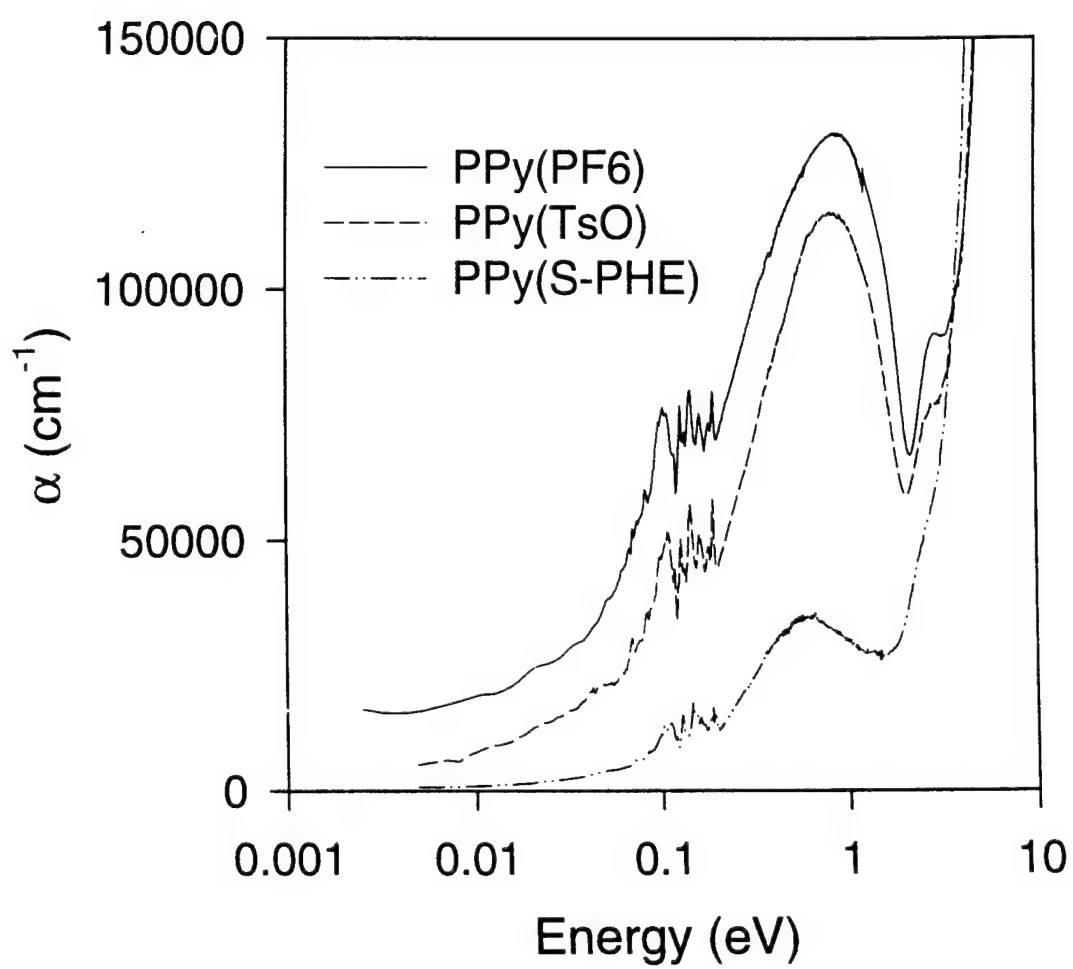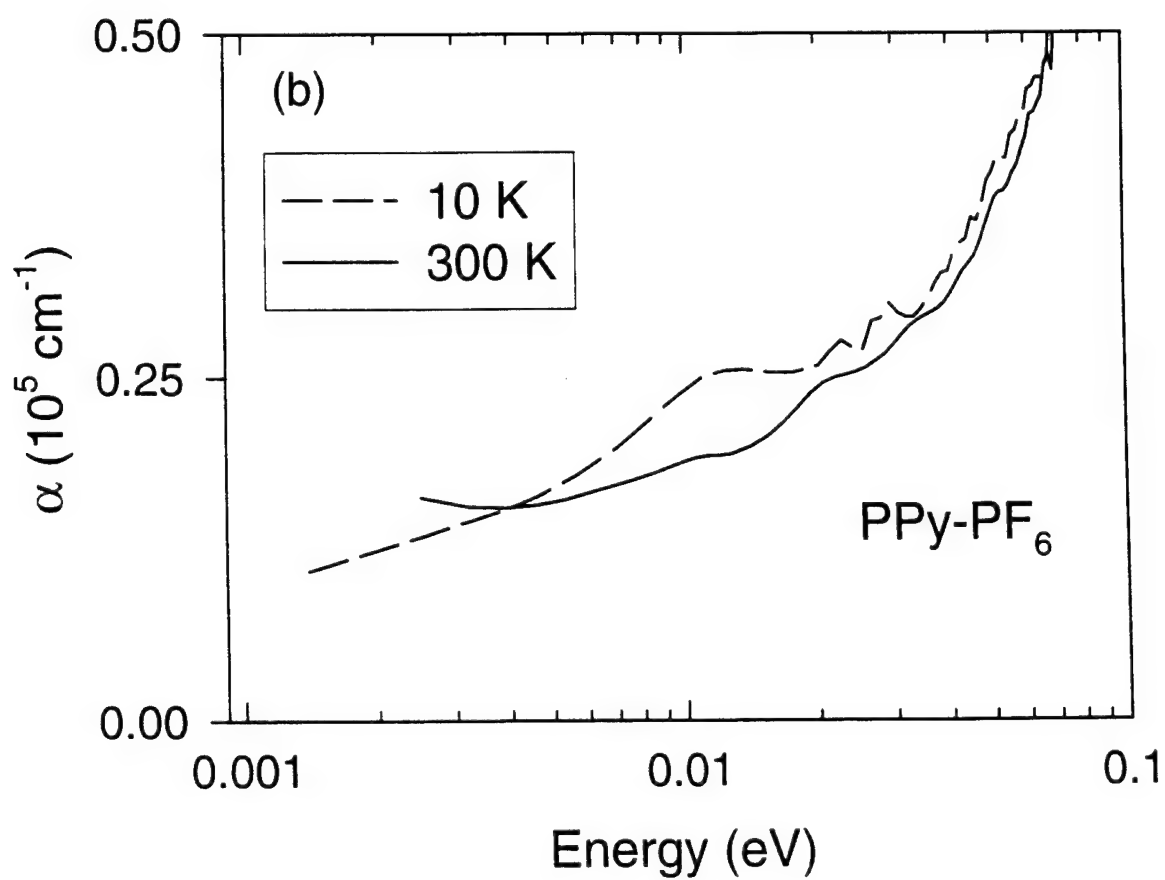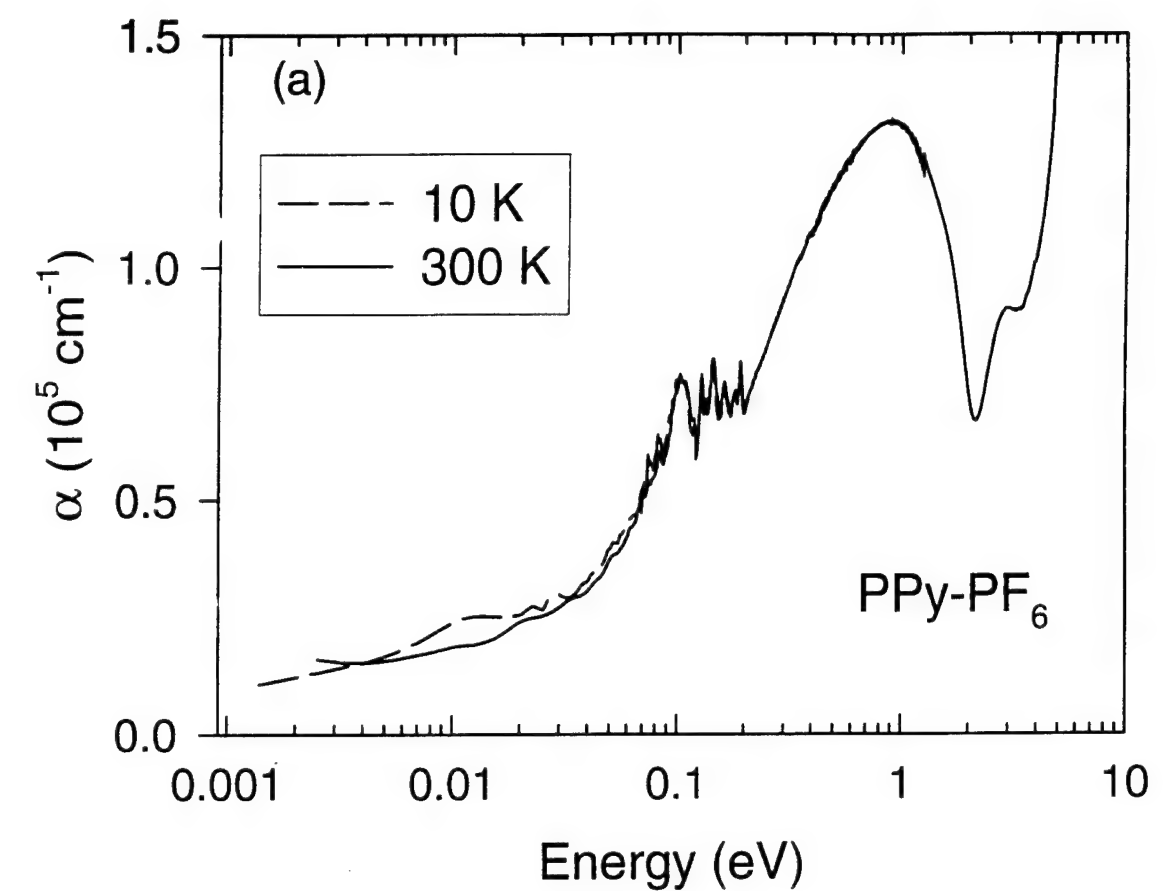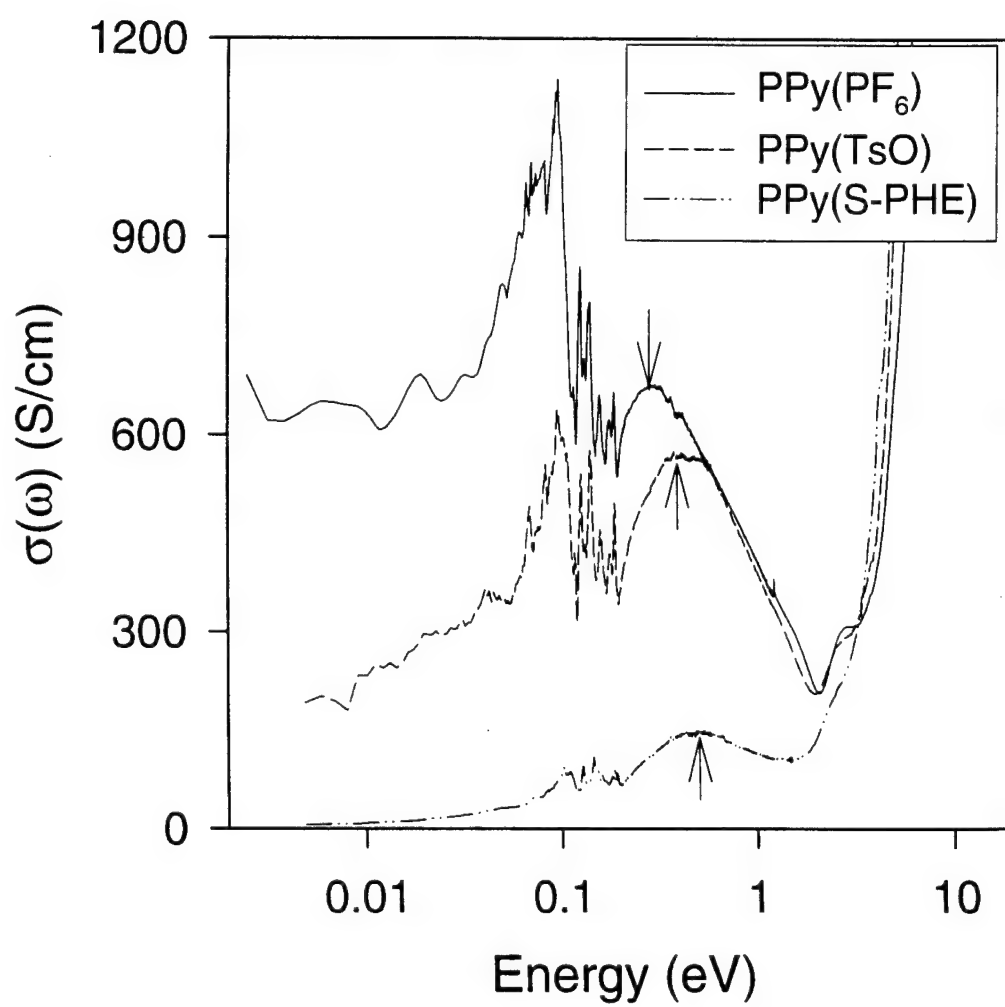
Figure 38

Figure 39

Figure 40

Figure 41

Figure 42

Figure 43